Carnegie Mellon University
MELLON COLLEGE OF SCIENCE

THESIS

SUBMITTED IN PARTIAL FULFILLMENT OF THE REQUIREMENTS
FOR THE DEGREE OF

DOCTOR OF PHILOSOPHY IN THE FIELD OF PHYSICS

TITLE: "Properties of the ρ Resonance from ππ Elastic Scattering and the Spectrum of Excited ρ Mesons Using the Stochastic LapH Method in Lattice QCD"

PRESENTED BY: Brendan Fahy

ACCEPTED BY THE DEPARTMENT OF PHYSICS

Colin Morningstar	09/25/14
COLIN MORNINGSTAR, CHAIR PROFESSOR	DATE

Stephen Garoff	09/25/14
STEPHEN GAROFF, DEPT HEAD	DATE

APPROVED BY THE COLLEGE COUNCIL

Fred Gilman	09/24/14
FRED GILMAN, DEAN	DATE

Properties of the ρ Resonance from $\pi\pi$ Elastic Scattering and the Spectrum of Excited ρ Mesons Using the Stochastic LapH Method in Lattice QCD

by
Brendan Fahy

Submitted in partial fulfillment of the
requirements for the degree of
Doctor of Philosophy
at
Carnegie Mellon University
Department of Physics
Pittsburgh, Pennsylvania

Advisor: Professor Colin Morningstar

September 18, 2014

Abstract

Inclusion of multi-meson operators allows lattice QCD calculations to extract energies of resonances above two-meson thresholds, as well as to study two-meson scattering. Previously, temporal correlations involving multi-hadron operators were difficult to evaluate due to contributions from quark propagators which begin and end on the same time slice. The stochastic LapH method allows for efficient computations of such contributions and is applied in this work to compute the low-energy spectrum of the $I = 1$, $S = 0$, T_{1u}^{+} channel, as well as the P-wave $\pi\pi$ scattering phase shift. The calculations use 412 gauge-field configurations generated by a Monte Carlo method utilizing clover-improved Wilson fermions on an anisotropic $32^3 \times 256$ lattice with a pion mass near 240 MeV. The masses of the ρ meson and several excited mesons are computed using a 63×63 correlator matrix for total zero momentum and are shown to agree with experiment. Additionally, the low-energy spectrum of stationary states in several channels of nonzero total momenta are calculated. The $\pi\pi$ stationary-state energies in a finite box are used to calculate the infinite-volume $I = 1$ P-wave scattering phase shifts, from which the width of the ρ resonance is determined.

Acknowledgments

Foremost, I would like to express my gratitude to my advisor Prof. Colin Morningstar for help, insight, and guidance in this research. Additionally, I would like to thank the efforts of the following researchers: Prof. Keisuke Jimmy Juge, Prof. John Bulava, Dr. Chik Him, Wong, Dr. David Lenkner, Dr. You-Cyuan Jhang, and Ben Hoerz for their contributions and help at all stages. I must thank my fellow graduate students and friends at Carnegie Mellon for helping me survive both personally and academically. Finally, I would like to thank my parents for their endless support.

Contents

List of Tables

List of Figures

Chapter 1

Introduction

The standard model of particle physics works admirably well for describing the dynamics of all known subatomic particles. It has been accurate at describing a wide variety of scattering phenomena and successfully predicting new particles and interactions for the past few decades. Many observed particles, known as hadrons, are not elementary but are composites consisting of quarks and gluons. The sector of the theory describing the interactions of these quarks and gluons is known as Quantum Chromodynamics (QCD). QCD is also responsible for the binding of protons and neutrons inside the nuclei of atoms.

Quarks are spin-$\frac{1}{2}$ fermions with fractional electric charges and come in six types known as flavors. The six flavors are named up u, down d, strange s, charm c, bottom b, and top t, in order of increasing mass. Quarks also possess another kind of charge that can take one of three different values. This charge is capriciously named *color* and has values called red, green, and blue, in analogy with the primary colors in the visible spectrum of light. Quarks interact by exchanging gluons, which are spin-1 massless bosons that also possess color, but in a different way from that of the quarks.

QCD is a quantum field theory involving the quark and gluon fields whose interactions are governed by a Lagrangian which is invariant under local nonabelian $SU(3)$ color gauge transformations. The QCD action looks deceptively similar to that of quantum electrodynamics (QED). The carrier of the QED force, the photon, is electrically neutral, and photons do not directly interact with one another. In contrast, the gluon possesses color charge, and gluons strongly interact with one another. These features cause the properties of QCD to radically differ from those of QED.

QCD has the interesting propriety that the so-called renormalization group β

function of the theory is negative at small coupling. The β function describes the running of the coupling, or the strength of interactions, at different energies. At very small distances, the running QCD coupling becomes small, a property known as asymptotic freedom. Due to this feature of the theory, high energy processes, such as deep inelastic scattering, can be reliably calculated using standard Feynman diagram techniques, such as those which work well in quantum electrodynamics. However, at large distance scales, the running coupling is not small, and computing low-energy quantities, such as hadron masses and decay constants, cannot be reliably done with small-coupling perturbative expansions.

To study hadron formation in QCD, a nonperturbative approach is needed. Formulating the theory on a space-time lattice and using Monte Carlo methods to estimate the resulting lattice QCD path integrals is one such powerful approach. Lattice QCD began with Ken Wilson's seminal paper in 1974 [1]. Space and time are discretized using a lattice, which both regulates the theory, providing an ultraviolet cutoff by excluding very short wavelengths, as well as makes calculations feasible using computers and Monte Carlo methods. However, such calculations require large amounts of computer resources, and calculations of many quantities in lattice calculations are only now becoming feasible. Computational limitations caused early calculations to use small and coarse lattices, which introduced large discretization errors, to use quark masses producing unphysically large pion masses, and to ignoring the fermion determinant in the action all together (which was known as the quenched approximation).

Lattice Monte Carlo calculations are only feasible in a finite space-time volume with a nonzero lattice spacing. Using a coarser spacing allows for simulating larger volumes for the same computing power at the cost of increased discretization errors. Modern theoretical improvements in how the action is discretized can mitigate some of the effects of finite lattice spacing. To reduce computational costs, most simulations choose parameters such that the pion mass is nonphysically heavy. Algorithm improvements and increases in raw computing power are making simulations at or close to the physical pion mass possible only in recent years.

The correlation functions, or n-point Green's functions, of QCD provide the information needed to extract hadron properties. Correlators involving the quark fields require evaluating quark propagators from one space-time location to another. Evaluating these quark propagators is the most computationally expensive part of any

lattice QCD calculation. Studying excited hadrons and hadron-hadron scattering processes in lattice QCD has not been possible until very recently due to the large number of quark propagators needed in such calculations. However, new methods are making such studies possible now. In this work, we use a method, known as the stochastic LapH method, to compute the low-energy spectrum of the $I = 1$, $S = 0$, T_{1u}^{+} channel, as well as the P-wave $\pi\pi$ scattering phase shifts, from which the width of the ρ resonance is determined.

The organization of this work is as follows. Chapter 2 provides a basic overview of QCD and how observables can be computed using a lattice regularization. This is followed by Chapter 3 which discusses constructing interpolating operators with particular symmetries to probe the stationary states of interest. Chapter 4 outlines the stochastic LapH method and how to estimate two-point correlation functions between the operators selected. In Chapter 5, we describe how scattering phase shifts can be obtained from the energies of two-particle stationary states in finite volume. Chapter 6 covers the analysis of the correlation functions and how to fit the data to extract the energies of the stationary states. Finally, results of the excitation spectrum in the $I = 1$, $S = 0$, T_{1u}^{+} channel, as well as the P-wave $\pi\pi$ scattering phase shifts, using a $32^3 \times 256$ anisotropic lattice are presented in Chapter 7, followed by conclusions in Chapter 8.

Chapter 2

Lattice QCD

Since standard perturbative methods fail to be useful for QCD at low energies, a non-perturbative approach known as Lattice gauge theory was developed. This involves treating space-time as a grid of discrete points. If the discretization is done properly, calculations can be performed which recover the original theory as the spacing between each of the lattice points, a, approaches zero.

Discretizing space-time into grid points regulates the ultraviolet divergences of the theory as modes with wavelengths much smaller than the lattice spacing are excluded and the quantum field theory becomes finite and mathematically well defined. An added benefit of treating space-time as discrete points is that it allows the theory to be modeled by computers. The path integrals which yield the correlation functions of the theory from which one extracts the physics can be approximated with Monte Carlo methods. To evaluate physical results reliably, a small lattice spacing is needed, or an extrapolation to zero spacing must be carried out.

This chapter will discuss the foundations of lattice QCD and how QCD is formulated on a lattice in Sec. 2.1. Next, Sec. 2.2 introduces the lattice QCD correlation functions from which observables are obtained. Sec. 2.3 contains an explanation of how the correlation functions are evaluated using computers. Finally, the specific details of the lattices and methods used in this work are given in Sec. 2.4.

2.1 Lattice Formulation

2.1.1 QCD in the continuum

This section discusses the details of QCD and how to formulate the theory on a space-time lattice. To begin, we define the continuum version and then discuss the process of discretization. First, the fields and the continuum action are introduced in Euclidean space-time (the imaginary time formalism), as opposed to the more usual Minkowski space-time. The reason for this will be given later. To define the theory in Euclidean space-time, one performs a Wick rotation to imaginary time $t \to -i\tau$. Under this transformation, there is no distinction between covariant and contravariant indices. We define a space-time vector x_μ to take indices $\mu = 1, 2, 3, 4$ where index $\mu = 4$ is the imaginary time coordinate. This gives a relation between a vector in Euclidean and Minkowski space-time as:

$$x^j = x_j = x^j_{\text{Minkowski}} = -x_{j\,\text{Minkowski}} \tag{2.1}$$

$$x^4 = x_4 = x^0_{\text{Minkowski}} = -x_{0\,\text{Minkowski}} \tag{2.2}$$

The quark fields are represented by Dirac 4-spinors:

$$\psi^{f,c}_\alpha(x), \quad \overline{\psi}^{f,c}_\alpha(x) \tag{2.3}$$

where α is the Dirac index $\alpha = 1, 2, 3, 4$ for the four spinor components, and c is a quantum number known as *color*. Note that in Euclidean space-time ψ and $\overline{\psi}$ are independent integration variables, so the relation for Minkowskian operators does not hold $\overline{\psi} \neq \psi^\dagger \gamma_0$. The quark fields come in six flavors (designated by the index f) named up, down, strange, charm, top, and bottom. The masses of all of these flavors are input parameters to the theory. The masses of flavors can differ by $\approx 10^5$ and for studying phenomena at lower energy (such as this work), the heavier flavors can be ignored. In addition to the quark fields, QCD contains gauge fields named gluons,

$$A_\mu(x) = \sum_{a=1}^{8} A^a_\mu(x) T^a \tag{2.4}$$

where T^a are the generators of the Lie algebra $SU(3)$, known as the Gell-Mann matrices. The index μ is a Lorentz index which denotes the direction in space-time.

For free quarks, the Lagrangian is:

$$\mathcal{L}_{\text{free}} = \sum_{f=u,d,s,\ldots} \overline{\psi}^f (\not{\partial} + m_f)\psi^f. \tag{2.5}$$

QCD is said to be an $SU(3)$ gauge theory, which means the Lagrangian of the theory is invariant under local gauge transformations which are elements of $SU(3)$. To ensure the Lagrangian is gauge-invariant, we replace the derivative with a gauge-covariant derivative

$$\mathcal{L}_{\text{quark}} = \sum_{f=u,d,s,\ldots} \overline{\psi}^f (\not{D} + m_f)\psi^f \quad \text{where} \quad D_\mu = \partial_\mu + igA_\mu(x) \tag{2.6}$$

which couples the quarks and gluons, where g is the QCD coupling, and we include an interaction for the gauge bosons of the form

$$\mathcal{L}_{\text{gauge}} = \frac{1}{4}\sum_{a=1}^{8} F^a_{\mu\nu}(x)F^a_{\mu\nu}(x). \tag{2.7}$$

Summing the two gives us the Lagrangian for QCD in the continuum. The next step is to define the lattice discretization of this theory.

2.1.2 Lattice Discretization

Discretization is redefining the continuum action onto a Euclidean space-time lattice. Instead of each field existing on all points in the manifold, we only consider discrete points separated by some spacing in each direction a_μ. The discretization of space-time regulates the theory by providing a momentum cut-off $\propto 1/a_\mu$ removing any ultraviolet divergences. This also makes approximating path integrals feasible as there are now a finite number of sites in a given region of space-time. If we are only interested in the physics at low energies, then quantities should be insensitive to the removal of information at distances less than a_μ. If this is done carefully, then the continuum theory should be recovered by taking the limit $a_\mu \to 0$. In this work, an anisotropic lattice is used so the spacing in the spacial directions, a_s is different than the lattice spacing in the temporal direction a_t. However, for simplicity, this section will treat the discretization for an isotropic case and the anisoptroic action will be discussed in Sec. 2.1.3.

In Eqs. 2.3 and 2.4, the fields are functions of the variable x representing location in space-time. This must be replaced by discrete points so the fields are now functions of $x_\mu \to n_\mu a_\mu$ where n_μ is a label for each of the points in the grid. The first issue to consider is the derivative term in the quark action. This derivative can be discretized as a finite difference as

$$\partial_\mu \phi(x) \to \frac{1}{2a} \left(\phi(n + \hat{\mu}) - \phi(n - \hat{\mu}) \right). \tag{2.8}$$

When applied to the covariant derivative of the quark and gluon fields, this produces an action which is not gauge invariant. We need to produce the analog of a covariant derivative, and introduce the gauge field in a way which preserves the gauge symmetry. Wilson proposed[1] a way to do this by introducing the gauge field as a set of *link variables* $U_\mu(n)$. Each $U_\mu(n)$ is an element of $SU(3)$ associated with the link starting at n and terminating at $n + \hat{\mu}$.

This idea comes from considering a *gauge transporter*, $G(x, y)$, which is a path-ordered exponential integral of the gauge field along some curve C.

$$G(x, y) = P \exp \left(ig \int_C A \cdot ds \right) \tag{2.9}$$

Wilson's link variables are simply the gauge transporters along the links of the lattice

$$U_\mu(n) = P \exp \left(ig \int_n^{n+\hat{\mu}} A \cdot ds \right). \tag{2.10}$$

Using these link variables, we must now define a discretized version of the gluonic action and the quark action which has the desired transformation properties. First, we start with the gluonic action. Representing the gluonic fields on the links rather than the lattice sites makes the action look different that the continuum version, but it is recovered in the limit of small spacing. It is important to build an object out of the link variables which is gauge invariant. The Wilson gauge action is built out of objects called "plaquettes" which are products of four link variables which form a closed loop:

$$P_{\mu\nu} = U_\mu(n) U_\nu(n + \hat{\mu}) U_\mu^\dagger(n + \hat{\nu}) U_\nu^\dagger(n). \tag{2.11}$$

The trace of any product of links which forms a closed loop is a gauge-invariant object.

The simplest closed loop of the plaquette is sufficient to build the gauge action. The Wilson gauge action is defined as the sum over the trace of all plaquettes

$$S_G[U] = \frac{2}{g^2} \sum_x \sum_{\mu<\nu} \mathrm{Re}\,\mathrm{Tr}\,(1 - P_{\mu\nu}) \tag{2.12}$$

This reduces to the continuum action by using Eq. 2.10 and expanding for small a. Inserting 2.10 into Eq. 2.11 and using the Baker-Campbell-Hausdorff formula we get $P_{\mu\nu} = \exp\left(ia^2 F_{\mu\nu} + \mathcal{O}(a^3)\right)$. This results in the Wilson gauge action approximating the continuum action up to order $\mathcal{O}(a^2)$.

We also need to define a discretized version of the quark action using the link variables. A quark action which is gauge invariant can be obtained using a *covariant finite difference*:

$$D_\mu(x,y) \to \Delta_\mu(n,m) = \frac{1}{2a_\mu}\left[U_\mu(n)\delta(n+\hat{\mu},m) - U_\mu^\dagger(n-\hat{\mu})\delta(n-\hat{\mu},m)\right] \tag{2.13}$$

The simplest gauge-invariant quark Lagrangian density can be written

$$\mathcal{L}_\mu = \left[\overline{\psi}(n)\gamma_\mu \frac{U_\mu\psi(n+\hat{\mu}) - U_\mu^\dagger(x-\hat{\mu})\psi(n-\mu)}{2a_\mu} + \overline{\psi}(n)m\psi(n)\right] \tag{2.14}$$

in which the flavor and color indices have been suppressed. One can see this approximates the continuum action by inserting $U_\mu(n) = 1 + iaA_\mu(n) + \mathcal{O}(a^2)$.

Unfortunately, this discretization suffers from a problem known as the *fermion doubling problem*. The quark action is often written as

$$S_f = a^4 \sum_{n,m} \overline{\psi}(n)\mathcal{M}(n,m)\psi(m) \tag{2.15}$$

where $\mathcal{M}$ is the Dirac matrix

$$\mathcal{M}(n,m) = \sum_\mu \gamma_\mu \Delta(n,m) + m_f\delta(n,m). \tag{2.16}$$

The problem can be seen by looking at the inverse of the Dirac matrix 2.16. This is known as the quark propagator and should have a single pole at $p^2 = -m^2$ in the free theory. However, the discretization scheme causes there to be extra nonphysical

poles in the free quark propagator

$$\left\langle \psi(p)\overline{\psi}(q)\right\rangle = \mathcal{M}^{-1}(p,q) = \delta(p,q)\frac{-i\sum_\mu \frac{1}{a_\mu}\gamma_\mu \sin(p_\mu a_\mu) + m}{\sum_\mu \frac{1}{a_\mu^2}\sin^2(p_\mu a_\mu) + m^2}. \tag{2.17}$$

The free quark propagator has the correct continuum limit, but for non-zero lattice spacing, there are extra poles when $\sin(a_\mu p_\mu)^2 = -m^2$. These extra poles are referred to as fermion doublers.

The fermion doubling problem is an artifact of our discretization scheme. Wilson proposed a different discretization which still recovers the continuum action in the limit of the lattice spacing going to zero, but removes the nonphysical poles. This is done by adding an extra term to the Dirac operator which vanishes for $a \to 0$, to order $\mathcal{O}(a)$, but at finite a, gives an extra mass to the doublers which is proportional to $\frac{1}{a}$. This means that in approaching the continuum limit, the doublers become extremely heavy and can be ignored. The additional term suggested by Wilson has the form

$$\mathcal{M}_W(n,m) = \mathcal{M}(n,m) - a\left[\frac{U_\mu(n)\delta(n+\hat{\mu},m) - 2\delta(n,m) + U_\mu^\dagger(n-\hat{\mu})\delta(n-\hat{\mu},m)}{2a_\mu^2}\right]. \tag{2.18}$$

The addition of this term solves the fermion doubling problem. However, the action no longer preserves chiral symmetry. There is a famous no-go theorem[2] which proves that there is no lattice regularization which respects Hermiticity, locality, and translational invariance without breaking chiral symmetry. The approach above solves the problem by explicitly breaking chiral symmetry, but there have been other approaches to fermions in lattice field theory. Other choices may decide to break the requirement of locality in order to preserve features of chiral symmetry. The choice of discretization scheme depends on the physics of interest and the cost to implement.

In this work, Wilson fermions are used which explicitly breaks chiral symmetry. However, the effect of this breaking is reduced by including an additional term named the "clover" term[3]. The inclusion of the additional clover term, and the use of smeared gauge link variables in place of the raw link variables, has been shown to mitigate some of the effects [4], [5] of the broken chiral symmetry. Further discussion of this improvement is in Sec. 2.1.3, with the details of link smearing covered in Sec. 3.1.1.

2.1.3 Action Improvements

Sec. 2.1.2 presented the basics of how to build an action on the lattice which reproduces the QCD action in the continuum limit. That action is not unique and other ways to discretize the action can be used provided they have the same continuum behavior. In this work, we use an "improved" action which recovers the continuum behavior to a higher order in the lattice spacing a. Additionally, the action is split into temporal and spatial parts with different lattice spacing a_s and a_t to give a finer resolution in the temporal direction $a_t \ll a_s$. This section presents the improvements to both the fermionic and gluonic parts of the action used in this work.

As will be seen in Chapter 6, information about the energy states is extracted from the temporal evolution of a correlation function. The temporal resolution can be increased without requiring a larger number of spatial lattice points by setting the temporal lattice spacing to be smaller than the spatial one $a_s = \xi a_t$ with $\xi > 1$. Before proceeding to write down the improved action, we express the Wilson gauge action 2.12 and Wilson fermionic action 2.15 on an anisotropic lattice. The unimproved anisotropic Wilson gluonic action is given by:

$$S_G^W = \frac{5\beta}{3\xi_g}\Omega_s^P + \frac{4\beta\xi_g}{3}\Omega_t^P \tag{2.19}$$

$$\Omega_s^P = \sum_{i<j} \mathrm{Re}\,\mathrm{Tr}\,(1 - P_{ij}) \tag{2.20}$$

$$\Omega_t^P = \sum_{i} \mathrm{Re}\,\mathrm{Tr}\,(1 - P_{it}) \tag{2.21}$$

where P are the plaquettes defined in Eq. 2.11, ξ_g is the bare gauge anisotropy and $\beta = 2N_c/g = 6/g$ is in place of the bare coupling. The Wilson fermionic action is split up similarly, with separate temporal and spatial parts for both the lattice derivatives and Laplacian. The anisotropic fermionic action is

$$S_f^W = a^4 \sum_{n,m} \overline{\psi}(n) \left[m^f + \gamma_t \nabla_t - \frac{a_t}{2}\nabla_t^2 + \frac{1}{\xi_f}\sum_i \gamma_i \nabla_i - \frac{a_s}{2}\nabla_i^2 \right] \psi(m) \tag{2.22}$$

where ξ_f is the bare fermionic aspect ratio.

One check which can be done on lattice calculations is to look at short range quantities where perturbation theory should be valid. It was found that there was significant disagreement between lattice results and perturbation theory for a variety

of short-distance quantities. However, the largest source of the disagreement was found to be contributions from so-called *tadpole* diagrams. Lepage and Mackenzie [6] developed a *tadpole improvement* scheme to absorb the nonphysical ultraviolet effects introduced by the expansion of the gauge transporter. This was done by normalizing the link variables through a mean-field approximation, replacing U with U/u where

$$u = \left\langle \frac{1}{3} \mathrm{ReTr}\left(U_{\mu\nu}\right) \right\rangle^{1/4}. \tag{2.23}$$

This mean field should be closer to unity and its use reduced the discrepancies mentioned above. On our anisotropic lattices, we require two different tadpole factors one for the spatial directions u_s an one for the temporal direction u_t.

Using the standard Wilson gauge action gives the correct continuum limit ($a \to 0$), but Wilson's gauge action has discretization errors of $\mathcal{O}(a^2)$ and the fermionic action has errors of $\mathcal{O}(a)$. There is nothing unique about these choices of discretization and we are free to discretize differently to remove leading order discretization errors, provided the terms preserve all symmetries of interest. Changing the discretization scheme to achieve faster approach to continuum behavior is known as a Symanzik improvement program [7–9].

The idea behind Symanzik improvement is that, given a finite difference approximation to a derivative, the Taylor expansion of the leading term is the desired derivative, but the error will be determined by higher terms which can be expressed as higher derivatives. As an example, a first derivative $D_1 = (f(x+h) - f(x-h))/2h$ has an expansion $D_1 = f'(x) + \frac{h^2}{6} f'''(x) + \mathcal{O}(h^4)$. Alternatively, one can expand the same derivative as $D_2 = (f(x+2h) - f(x-2h))/4h$, which again produces a first derivative in the limit of $h \to 0$, but the leading error is $\frac{2h^2}{3} f'''(x)$. One can then combine the two into a more complicated finite difference $(4/3)D_1 - (1/3)D_2$ to approximate the first derivative, whose errors are now $\mathcal{O}(h^4)$.

First, we apply the Symanzik improvement program to the Wilson gluonic action, which is order a^2. Rather than just looking at 1×1 plaquettes, we can remove the order a contribution by introducing 2×1 rectangular loops. The temporal rectangles are arranged such that the length-2 side is never in the time direction, because terms in the action which contain more than one site in the temporal direction cause the transfer matrix to not be positive definite, and unphysical negative norm states can occur. One then defines Ω^R's which are the same as the Ω^P's defined in Eq. 2.19,

but replacing the plaquettes with the 2×1 loops R. The Symanzik improved gauge action is then written

$$S_g = \frac{5\beta}{3\xi_g u_s^4}\Omega_s^P + \frac{4\beta\xi_g}{3u_s^2 u_t^2}\Omega_t^P + \frac{\beta}{12\xi_g u_s^6}\Omega_s^R + \frac{4\beta\xi_g}{12u_s^4 u_t^2}\Omega_t^P. \tag{2.24}$$

The tadpole factors in the gauge action were set to $u_s = 0.7336$ and $u_t = 1$ from the work in Ref. [4]. This improved action has leading order discretization effects of $\mathcal{O}\left(a_t^2, g^2 a_s^2, a_s^4\right)$.

The Wilson fermionic action has discretization errors of $\mathcal{O}\left(a\right)$ and the Symanzik procedure can be used here as well. One introduces a clover term which is named by the shape made by the gauge links. This term is

$$c\overline{\psi}\frac{1}{2}\sigma_{\mu\nu}F_{\mu\nu}\psi \tag{2.25}$$

and the discretized version of $F_{\mu\nu}$ is $F_{\mu\nu} = \frac{1}{8ia^2} = \left(Q_{\mu\nu} - Q_{\mu\nu}^\dagger\right)$, where Q is the average of four plaquettes around the lattice point depicted pictorially in Fig. 2.1. The clover parameter c is tuned using perturbation theory. Again, there will be separate parameters for directions c_s and c_t. The clover-Wilson tadpole improved action has the form

$$S_f = a^4 \sum_{n,m} \overline{\psi}(n)\mathcal{M}(n,m)\psi(m), \tag{2.26}$$

where

$$\mathcal{M} = m^f + \frac{1}{\widetilde{u}_t}\left(\gamma_t\nabla_t - \frac{a_t}{2}\nabla_t^2\right) + \frac{1}{\widetilde{u}_s\xi_f}\left(\sum_i \gamma_i\nabla_i - \frac{a_s}{2}\nabla_i^2\right) - \frac{c_s a_s}{2\widetilde{u}_s^3}\sum_{i<j}\sigma_{ij}F_{ij} - \frac{c_t a_t}{2\widetilde{u}_t\widetilde{u}_s^2}\sum_i \sigma_{tj}F_{tj}, \tag{2.27}$$

and the $\widetilde{u}_t$ and $\widetilde{u}_t$ are the tadpole factors for the fermionic action which were set to 0.9267 and 1, respectively. The c_s and c_t are the clover parameters and were tuned to $c_s = 1$ and $c_t = \frac{1}{2}\left(1 + \xi\right)$, where here ξ is the desired renormalized anisotropy. The improved action used in this work has discretization error of $\mathcal{O}(g^2 a_s, g^2 a_t, a_s^2, a_t^2)$.

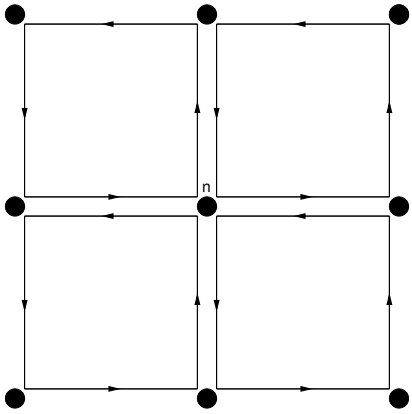

Figure 2.1: Diagram of $Q_{\mu\nu}$ in terms of the link variables in the clover term.

2.2 Correlation Functions

The above sections described the discretized action to be used in our lattice QCD studies. This section will discuss how we calculate observables of interest within the discretized quantum field theory we have developed. This is done using the path integral formulation of quantum field theory. The energies of the stationary states of the Hamiltonian can be determined from the temporal fall-off of a two-point correlation function. This section will identify how two-point correlation functions are defined in our formalism and how energies can be extracted from them.

The path integral formulation of quantum mechanics expresses transition amplitudes from one state to another as an integral over all paths. All paths are considered, but each path has an associated phase of $\exp\left(iS[x(t)]/\hbar\right)$, where $x(t)$ is a given path. This shows a connection to the classical principle of least action as paths whose small alterations change the action significantly compared to $\hbar$ cancel one another.

In a quantum field theory, the time-ordered vacuum expectation value of quantum field operators can be expressed as a functional integral over all field configurations. After changing units such that $\hbar = 1$, this is written as

$$\begin{aligned} C_{ij}(t,t_0) &= \langle 0|T\mathcal{O}_i[\phi,\overline{\phi},U](t)\overline{\mathcal{O}}_j[\phi,\overline{\phi},U](t_0)|0\rangle \\ &= \frac{\int \mathcal{D}\phi\mathcal{D}\overline{\phi}\mathcal{D}U\ \mathcal{O}_i[\phi,\overline{\phi},U](t)\overline{\mathcal{O}}_j[\phi,\overline{\phi},U](t_0)\ \exp\left(-S[\phi,\overline{\phi},U]\right)}{\int \mathcal{D}\phi\mathcal{D}\overline{\phi}\mathcal{D}U\ \exp\left(-S_G[\phi,\overline{\phi},U]\right)} \end{aligned} \tag{2.28}$$

where T is time ordering, $\mathcal{O}_i$ and $\mathcal{O}_j$ are operators which create or annihilate states, and S is the action and $\mathcal{D}\phi, \mathcal{D}\overline{\phi}, \mathcal{D}U$ represents an integration over all possible field

configurations. The exponential factors are not oscillatory due to the Wick rotation. The replacement of $t \to -i\tau$ makes the oscillatory exponential factors enter as Boltzmann-like factors $\exp(-S)$. Since $\exp(-S)$ is real and positive, it can be interpreted as a probability distribution, which is the key to being able to evaluate the integrals on a computer with the Monte Carlo method. The details of this will be discussed in Sec. 2.3.1.

We want to use two-point correlation functions to determine the energies of the stationary states of the lattice Hamiltonian. Let $|n\rangle$ be the nth eigenstate of the lattice Hamiltonian which has energy E_n. Since we do not know the eigenstates of QCD (which is what we are ultimately trying to determine), our operators will not be creation operators for any one eigenstate $|n\rangle$. Instead we expect our operators operating on the vacuum to create a large number of eigenstates. Since the calculation is being done in a finite volume, the energies of the eigenstates $|n\rangle$ are discrete due to momentum quantization. With that in mind, inserting a complete set of states gives a spectral representation of the two point function. By viewing our operators in the Heisenberg-picture operators $\mathcal{O}_i(t) = e^{Ht}\mathcal{O}_i(0)e^{-Ht}$, the two point function becomes

$$C_{ij}(t_2, t_1) = \langle 0|T\mathcal{O}_i(t_2)\overline{\mathcal{O}}_j(t_1)|0\rangle = \sum_n Z_i^n \left(Z_j^n\right)^* \exp\left(-E_n(t_1 - t_2)\right) \tag{2.29}$$

where Z_i and Z_j are

$$Z_i^n = \langle 0|\mathcal{O}_i|n\rangle, \qquad (Z_i^n)^* = \langle n|\overline{\mathcal{O}}_i|0\rangle. \tag{2.30}$$

The quantities $\langle 0|\mathcal{O}_i|n\rangle$ are called *overlaps* as they represent how much our operator produces the eigenstate $|n\rangle$. The spectral representation Eq. 2.29 is the central equation for computing the energies of QCD on the lattice. The key feature is that computing the fall off of the correlation function at different time separations $t_2 - t_1$ gives information about the energy.

Using Eq. 2.29 allows computation of the lowest energy of all states produced by $\overline{\mathcal{O}}_j$ acting the vacuum at large temporal separation, as contributions from higher energies decay away more quickly. Energies above the lowest-lying state are difficult to determine from a single correlation function as a particular operator will have many states $|n\rangle$ created and the magnitudes will be unknown. Fitting a single correlator to a large sum of exponentials is technically possible, but has far too many parameters

to be practical for a small number of data points. Instead, a set of N_{op} operators $\{\mathcal{O}_i\}$ are used to produce an $N_{\text{op}} \times N_{\text{op}}$ matrix of two point correlation functions. This matrix can then be rotated by finding a basis which makes the matrix diagonal. If this is done properly, the diagonal elements will be dominated by a single exponential and a spectrum of energies can be determined. Details of this process will be shown in Sec. 6.3.

2.2.1 Fermions

The quark fields are fermionic and must anti-commute. This is done by representing the fields with Grassman values. Manipulating Grassmann fields in computer software is difficult to do. Fortunately, it is possible to integrate out the fermion fields exactly, as described in this section.

Recall that the action is split into two parts: a gluonic part and fermionic part

$$S[\psi, \overline{\psi}, U] = S_g[U] + S_f[\psi, \overline{\psi}, U]. \tag{2.31}$$

The fermionic part of the action can be written as a bi-linear of the quark fields

$$S_f[\psi, \overline{\psi}, U] = \sum_{x_1, x_2} \overline{\psi}(x_1) \mathcal{M}(x_1, x_2|U) \psi(x_2) \tag{2.32}$$

where $\mathcal{M}$ is the Dirac matrix from Eq. 2.18. The integral over the fermionic part of the action is a Gaussian integral. A Gaussian integral over Grassman variables can be evaluated with the Matthews-Salam formula [10, 11]. The integration over the fermion fields with an integrand containing only the exponential of the action evaluates to a determinant of the Dirac matrix

$$\int \mathcal{D}U \, \exp\left(-S_g\right) \int \mathcal{D}\psi \mathcal{D}\overline{\psi} \, \exp\left(-S_f\right) = \int \mathcal{D}U \, \exp\left(-S_g\right) \det \mathcal{M}. \tag{2.33}$$

The hadron operators we use in our correlator calculations depend upon the quark fields, and thus, these need to be included at this stage. The results depend on what operators are included. The integral can be evaluated using *Wick's theorem* and will be in terms of products of $\mathcal{M}^{-1}$ corresponding to contractions of the chosen operators. By defining $F[\mathcal{M}^{-1}, U]$ to be the results of the Wick contractions of creation and

annihilation operators within $\mathcal{O}_i(t)$ and $\mathcal{O}_j(t_0)$, the correlator integral can be written

$$C_{ij} = \frac{\int \mathcal{D}U \; F[\mathcal{M}^{-1}, U] \det \mathcal{M} \exp\left(-S_g[U]\right)}{\int \mathcal{D}U \; \det \mathcal{M} \exp\left(-S_g[U]\right)}. \tag{2.34}$$

The determinant of the Dirac matrix, $\det \mathcal{M}$, is called the fermion determinant. Unfortunately, it is non-local and is very expensive to compute. Because of the difficulty in computing this, early lattice calculations made a simplification of simply setting the value equal to one. This is known as the *quenched approximation*. With the computing power available today, this approximation is no longer needed, and simulations which include the fermion determinant are referred to as simulations with *dynamical quarks*.

2.3 Computational Methods

2.3.1 Monte Carlo

To estimate correlation functions requires computing the ratio of integrals in Eq. 2.34. Since we are restricting ourselves to a lattice, the fields can be represented by using a finite number of link variables. If we consider just the gauge links on a 4D lattice of N points in each direction, there are $4 \times N^4$ gauge link variables. Since each link variable is represented by an element of $SU(3)$ which can be represented using at fewest 8 parameters, just representing the entire lattice requires a large amount of computer storage/memory. Additionally, there are an infinite number of possible values for each link variable so generating all possible field configurations is impossible.

Because of the exponential weighting of the Boltzmann factor, not all configurations contribute in a significant way. This allows us to do "importance sampling" Monte Carlo to statistically approximate the integral. Rather than enumerate all possible field configurations, we examine a small sample of configurations. The trick is to create a set of configurations in which each configuration is added to the set with a probability corresponding to the Boltzmann factor. By producing a set of configurations which are selected from a distribution according to the correct probabilities,

the value of an integral of interest becomes a simple sum

$$\langle X \rangle \approx \frac{1}{N} \sum_{i=i}^{N} X(\mathcal{C}_i) \tag{2.35}$$

where the set of configurations $\{\mathcal{C}\}$ are distributed according to the distribution

$$W[\mathcal{C}_i] = \frac{\exp(-S[\mathcal{C}_i]) \det[K]}{\mathcal{Z}}. \tag{2.36}$$

The challenge then becomes how to create a set of field configurations which follows the correct distribution. The basic idea of importance sampling Monte Carlo is to use a stochastic process to generate configurations constrained in such a way that the configurations are added with the correct probabilities. This process is done using a Markov chain whose fixed point is W. The Markov chain is generated by a process which randomly selects a new configuration which only depends on the previous entry in the chain. Let $p_{i\to j}$ denote the probability of selecting $\mathcal{C}_j$ if the previous entry is $\mathcal{C}_i$. A long chain of configurations are then generated starting with some random configuration and iterating one configuration at a time. Each configuration added is one "step". It is possible to construct a Markov chain such that after reaching equilibrium, the configurations will be distributed according to the desired probability distribution. The process of reaching the equilibrium state from any random configuration is called *thermalization*.

The Markov chain of configurations has the correct distribution if a few properties are satisfied. First is the requirement that any field configuration can eventually be generated from any starting point. The second requirement is the process be aperiodic, meaning it does not return to the same configuration at fixed intervals. These two requirements together are called *ergodicity*, and without it, there may be classes of configurations between which the chain could never transition. An additional requirement is that the chain be *reversible*, that the probability of transitioning from a configuration $\mathcal{C}_i$ to $\mathcal{C}_j$, $p_{i\to j}$, be the same as the probability of transitioning from $\mathcal{C}_j$ to $\mathcal{C}_j$ or

$$p_{i\to j} = p_{j\to i}. \tag{2.37}$$

For an ergodic reversible Markov chain, there exists a fixed point towards which

the chain will converge and configurations in the chain once in equilibrium will be distributed with that fixed-point distribution. We can then evaluate our integrals by setting up a Markov process to generate configurations which, after a period of thermalization, have the desired target distribution.

Since each configuration in the chain is generated using the previous configuration, there will be some dependency upon earlier elements. Even though elements of the chain follow the target distribution W in the long term, nearby elements are related and are not statistically independent. This is known as auto-correlation and is undesirable in Monte Carlo integration and increases the error in the estimate. Using a set of configurations generated as above, we can get an estimate of an integral

$$\int WXDc \approx \langle X \rangle \pm \frac{1}{\sqrt{N}} \sqrt{A_0(X) + 2 \sum_{h \geq 1} A_h(X)} \tag{2.38}$$

where N is the number of configurations used and A_h is the auto-correlation function between values h steps away given by

$$A_h(X) = \frac{1}{N-h} \sum_{i=1}^{N-h} \left(X(\mathcal{C}_i) - \langle X \rangle\right) \left(X(\mathcal{C}_{i+h}) - \langle X \rangle\right). \tag{2.39}$$

The auto correlations depend upon the integrand and the method of generating a new Monte Carlo step. In practice, a simple way to reduce auto correlations is to not use every element of the chain, but only use every nth element. The error is scaled overall by the square root of the number of configurations used, so we require an efficient method of generating elements for the Markov chain.

2.3.2 Configuration Generation

This section describes the process of generating the Markov chain which has the desired target distribution. It is desired to have a large number of configurations which have small auto-correlations. Due to the requirement of a large number of configurations, it is important to have a computationally efficient method of producing each step in the chain. This section presents the method used to produce the field configurations generated for the needed correlation functions.

A method of producing a Markov chain with a desired target distribution W is the *Metropolis-Hastings method*. In this method, one proposes a new candidate element

of the chain using the current configuration with probability $R(\mathcal{C}_j \leftarrow \mathcal{C}_i)$. One then accepts the element as a new step with probability

$$P_{\text{accept}} = \min\left(1, \frac{R(\mathcal{C}_j \leftarrow \mathcal{C}_i)W(\mathcal{C}_j)}{R(\mathcal{C}_i \leftarrow \mathcal{C}_j)W(\mathcal{C}_i)}\right). \tag{2.40}$$

If it is accepted, use $\mathcal{C}_j$ as the next element, otherwise keep the previous configuration. Repeat the process again proposing a new candidate from the last element of the chain. This simplifies in the case of a reversible proposal probability as the acceptance probability becomes $\min(1, W(\mathcal{C}_j)/W(\mathcal{C}_i))$. This boils down to always adding new elements if they are weighted higher in W than the current configuration, but only sometimes adding new elements which are weighted lower. When the acceptance probability is not unity, the use of uniform random numbers are required to test acceptance. One benefit of this method is that the normalization of W does not need to be known which is often difficult to compute. In the context of the quantum field theory integrals of interest, this process be seen as accepting configurations which lower the action, but only accepting configurations which increase the action some of the time.

This method relies on some choice of the proposal probability density R. A poor choice for R could result in almost all candidates becoming rejected which would waste time computing new states without making progress. It is also important that R make changes which have enough difference from the current configuration or the auto-correlations could be large and one could only use configurations separated by many steps. The auto-correlations depend on the observable being calculated. Local updates, such as a change to a single link variable at a time, have large autocorrelations with the previous configuration. So to reduce auto-correlations, we would like to use an R which proposes states which are significantly different from the current state. The presence of the fermion determinant in Eq. 2.36 complicates matters significantly. There is no advantage in proposing a local change since the determinant must be recalculated on the entire lattice. Thus, we need a proposal probability that generates a global change but in such a way that only small changes to the action are made to achieve a reasonable probability of acceptance.

2.3.3 The Hybrid Monte Carlo method

To propose a global modification to the gauge field which results in the action changing very little requires a clever algorithm. One such method involves forming a fictitious "Hamiltonian" and evolving the system according to Hamilton's equations of motion. This method hinges on being able to rewrite the weight function in the form of a Hamiltonian. For an even number of equal mass quark flavors, this can be done by introducing a pseudo-fermion field. This method is called Hybrid Monte Carlo (HMC)[12]. This section presents the HMC method, while the following method (RHMC) extends the method to add in the third quark flavor required for this work.

The first step is to rewrite our action in a form which can be expressed as a Hamiltonian. To deal with the fermion determinant, we introduce an additional field ϕ which is a bosonic complex-valued field. This field is often referred to as a pseudo-fermion field as it will be used to compute the fermion determinant despite being a bosonic field. With this field, we can express the quark determinant as an integral

$$\det \mathcal{M} = \int \mathcal{D}\phi \exp\left(\phi^\dagger \mathcal{M}^{-1} \phi\right). \tag{2.41}$$

This means that instead of attempting to use Grassman valued fields, we can simulate using the bosonic ϕ which has a non-local "action". This is simply extended to the case of two degenerate light quark fields by

$$\det \mathcal{M}_u \det \mathcal{M}_d = \det \mathcal{M}_l^\dagger \mathcal{M}_l = \int \mathcal{D}\phi \exp\left(\phi^\dagger \left(\mathcal{M}_l^\dagger \mathcal{M}_l\right)^{-1} \phi\right). \tag{2.42}$$

This works because $\mathcal{M}^\dagger = \gamma_5 \mathcal{M}^\dagger \gamma_5$, the determinant of $\det(\gamma_5)^2 = 1$, and the product of the Dirac matrix with itself is guaranteed to be positive. We can use this to rewrite the action in terms of the gauge fields U and the pseudo fermion fields ϕ:

$$S[U, \phi] = \phi^\dagger (\mathcal{M}^\dagger \mathcal{M})^{-1} \phi + S_g[U]. \tag{2.43}$$

In order to build a "Hamiltonian", we introduce fictitious "momenta" Π_μ, which are viewed as canonically conjugate to the U_μ fields, by inserting unity expressed as

$$1 = \int \mathcal{D}\Pi_\mu(x) \exp\left[-\frac{1}{2}\Pi^\dagger \Pi\right]. \tag{2.44}$$

Using this representation of unity, we insert it into the integral of interest

$$\int \mathcal{D}\Pi \exp\left[-\frac{1}{2}\Pi^\dagger\Pi\right] \int \mathcal{D}U\mathcal{D}\phi^\dagger\mathcal{D}\phi \exp\left(-S\right) \tag{2.45}$$

$$\int \mathcal{D}\Pi\mathcal{D}U\mathcal{D}\phi^\dagger\mathcal{D}\phi \exp\left[-\frac{1}{2}\Pi^\dagger\Pi - S\right] \tag{2.46}$$

$$\int \mathcal{D}\Pi\mathcal{D}U\mathcal{D}\phi^\dagger\mathcal{D}\phi \exp\left[-H\right] \tag{2.47}$$

where we introduce our fictitious "Hamiltonian" as

$$H = \frac{1}{2}\Pi_\mu^\dagger\Pi_\mu + S[U,\phi]. \tag{2.48}$$

Using this definition, we can evolve the system forward in fictitious time according to Hamilton's equation of motion. We solve Hamilton's equations using a finite step size $\delta\tau$ with a symplectic integration scheme. The state of Π and U after the discrete time evolution are then used as the proposed new element for the Metropolis-Hastings method. The time evolution nearly conserves H. Errors due to the discrete time steps used in the integration method cause the conservation to be only approximate. The accuracy of the integrator determines the acceptance rate for the proposed new field configuration. In this work, a second order Omelyan integrator was used [4] which is area preserving (required for detailed balance) and is accurate to $\mathcal{O}(\delta\tau^3)$.

The above method is not quite sufficient as it does not include the strange quark field. Extending the HMC method to include the strange quark field is called the Rational Hybrid Monte-Carlo method[13]. Before, we expressed the two light quark determinants in terms of an integral over pseudo fermion fields. We follow a similar process for the determinant over the strange field

$$\det\mathcal{M}_s = \det\left(\mathcal{M}_s^\dagger\mathcal{M}_s\right)^{\frac{1}{2}} = \int \mathcal{D}\phi \exp\left(\phi^\dagger\left(\mathcal{M}_s^\dagger\mathcal{M}_s\right)^{-1/2}\phi\right). \tag{2.49}$$

However, this is only allowed if $\det\left(\mathcal{M}_s\right)$ is positive. Since the strange quark mass is rather heavy, this is generally true.

This gives a relation from the pseudo fermion fields to the fermion fields of $\phi = \left(\mathcal{M}_s^\dagger\mathcal{M}_s\right)^{\frac{1}{4}}\psi$. This can be computed using the same pseudo fermion fields but requires computation of the fourth root $\mathcal{M}_s^\dagger\mathcal{M}_s$. This is done by using a rational

approximation

$$\left(\mathcal{M}_s^\dagger \mathcal{M}_s\right)^{\frac{1}{4}} \approx \alpha_0 I + \sum_i \frac{\alpha_i}{\mathcal{M}_s^\dagger \mathcal{M}_s + \beta_k}. \tag{2.50}$$

Computing $[\mathcal{M}_s^\dagger \mathcal{M}_s + \beta_k]^{-1}\phi$ is done simultaneously for all k using a multi-shift conjugate gradient solver.

2.4 The Lattice and Bare Parameters

The previous sections outlined the theoretical basis for our lattice calculations. This section discusses practical considerations of calculating on the lattice which must be addressed. Since discretization errors scale with the lattice spacing, one would like as fine a lattice as possible. However, decreasing the lattice spacing requires an increase in the number of lattice points to avoid finite volume effects. The physical size of the lattice should be much larger than the largest correlation length of the system, which will be determined by the mass of the pion. This requires a large number of lattice points, which drastically increases the computational requirements. So a trade off of accuracy due to discretization versus the computational requirements must be considered to determine how fine or coarse a lattice should be used.

The input parameters of the lattice QCD action are dimensionless. The main QCD coupling input parameter is β, and the so-called "bare" or Lagrangian quark masses are input in terms of the dimensionless products $a_t m_q$. We do not input a value for m_q in terms of MeV, but instead, a value for $a_t m_q$. The tuning of the bare parameters is detailed in Ref. [4], and a brief overview will be provided below. Given this, all results obtained are dimensionless. For example, an energy E of a given level is not determined directly, but rather, the dimensionless product $a_t E$ is determined. To obtain dimensionful estimates, we need some way of setting the lattice spacings a_t, a_s. This is known as "setting the scale." Since QCD is a renormalizable field theory, the scale can be set using a renormalization procedure.

The bare parameters which must be input to our discretized lattice action are β, the dimensionless light quark mass, m_ℓ, (suppressing the a_t), the strange quark mass, m_s, the gauge anisotropy ξ_g and the fermionic anisotropy ξ_f. One would like to choose these parameters such that the theory reproduces the correct physics of QCD. This must be done non-perturbatively, meaning testing many possible values for the

parameters and running a simulation and computing the n independent observables until it produces their physical values. Each bare parameter is associated with a measurable quantity, which is computed using many values of the input bare parameter to find a suitable choice. However, for computational feasibility, it is common to tune the bare quark mass such that the pion mass is set nonphysically large, as explained in the next section.

2.4.1 Nonphysical pion mass

Lattice calculations at the physical pion mass are only now becoming feasible. There are huge computational costs associated with computing using a physical pion, and so most calculations are still done with bare parameters set to yield a pion mass that is heavier than in nature. Lattice calculations are then simulating a *QCD-like* theory which has a heavier pion, and results must be extrapolated to the physical point. This section will outline some of the computational challenges of computing using light pion masses.

The largest computational cost in lattice QCD is by far inverting the Dirac matrix. While the Dirac matrix is guaranteed to have positive eigenvalues if $m > 0$, the broken chiral symmetry of the Wilson term means the fermion masses are not protected from additive renormalization. It turns out that to achieve physically relevant observables, the bare quark masses must be negative. This makes computing the inverse challenging as eigenvalues may be very small, making the matrix ill-conditioned. With very small eigenvalues, standard numerical techniques to compute the inverse take a large amount of computer power to converge.

Additionally, it is required that the lattice be large enough so that the finite volume does not have a significant effect on the observables. The long distance correlations are dominated by the lightest particle. So working with a heavier pion means that long distance effects are reduced and the simulation can use a smaller number of spatial points for a given lattice spacing. It has been established as a rule of thumb that finite volume effects in most quantities of interest are smaller than 1% if the mass of the pion mass times the spatial extent of the lattice sastisfies $m_\pi L > 4$.

A light pion also poses a challenge for the extraction of excited state energies. As we will see in Chapter 6, reliably extracting energy levels above the ground state requires inclusion of operators which have large overlaps with every state below the

state of interest. Approaching the physical pion mass means an increasing number of multi-hadron states will be below the resonances of interest. In this work, we include operators which should have strong overlaps with single and multi-hadron-like states. At low pion masses, consideration of three-pion or four-pion bound states could appear below most states of interest and may be significant.

As computer power increases and calculation methods improve, lattice studies are becoming more feasible at lighter pion masses. The community is now at a point that simple calculations at the physical pion mass are possible. However, these calculations are still limited to coarse lattices to reduce the computer resources required.

2.4.2 Lattice parameters

To determine the bare parameters, a Schrödinger functional approach was used which involves using a background field in the z direction. Details of the tuning process are in Ref. [4]. The bare quark masses were tuned using the following dimensionless quantities:

$$s_\Omega = \frac{9(m_K^2 - m_\pi^2)}{4m_\Omega^2} \tag{2.51}$$

$$l_\Omega = \frac{9m_\pi^2}{4m_\Omega^2} \tag{2.52}$$

where m_π, m_K and m_Ω are the masses of the pion, kaon and Ω baryon respectively. These quantities are proportional to the masses of the strange quark and the light quarks to leading order in chiral effective theory [14]. The s quark mass was tuned to the value $m_s = -0.0743$ such that s_Ω corresponded to the physical value. The running of s_Ω with respect to the light quark mass was found to be small. The light quark mass was tuned to $m_\ell = -0.0840$ and $m_\ell = -0.0860$ for the different lattices used in this work. These values correspond to $m_\pi \approx 390\,\text{MeV}$ and $m_\pi \approx 240\,\text{MeV}$ respectively. A summary of the parameter choices is shown in Table 2.1. When discussing a particular lattice, the naming convention of {spatial extent}_{light quark mass $\times -10,000$} is used, for example the second lattice in table 2.1 will be referred to as 24^3_840.

The value of the coupling used was $\beta = 1.5$. If the Ω baryon mass is used to set the scale, then one finds $a_s \approx 0.12$ fm and $a_t \approx 0.035$ fm. So our 16^3, 24^4 and 32^3 lattices would have a spatial extent L of ≈ 1.93 fm, ≈ 2.88 fm and ≈ 3.84 fm, respectively. These spatial lengths should be enough such that the finite volume of the box does

Spatial Extent	Time Extent	# of Configurations	m_ℓ	m_π	$m_\pi \times L$
16^3	128	100	-0.0840	≈ 390	≈ 3.8
24^3	128	551	-0.0840	≈ 390	≈ 5.7
24^3	128	584	-0.0860	≈ 240	≈ 3.5
32^3	256	412	-0.0860	≈ 240	≈ 4.7

Table 2.1: Lattices used in this work. The 16^3 lattice was mainly used for testing operators, while the 32^3 lattice was the target for the results. The number of configurations are how many field configurations were available to work with. m_ℓ is the bare light quark mass and the final column is the approximate pion mass which resulted from the bare mass input. The 24^3 lattice with the lighter pion was only used for testing purposes in this work as $m_\pi L$ is small, meaning it has large contributions due to finite volume.

not have a major effect. Since the pion is the lightest state, we should require that $m_\pi L$ be large. For the 24^3_840 and 32^3_860 ensembles, $m_\pi L > 4$ indicating finite volume effects are negligible which are the two lattices for which we report results.

The parameter ξ_g, or the spatial aspect ratio, was tuned using a ratio of Wilson loops in the spatial and temporal directions. A closed loop of gauge links oriented in two spatial directions or a spatial direction and the temporal direction are computed. The parameter in the anisotropic gauge action is then adjusted to give the desired aspect ratio of the two dimensions. In our calculations the desired anisotropy was 3.5 and it was found that a bare anisotropy of $\xi_g = 4.3$ gave close to the desired results. The anisotropy in the fermionic action was determined using the pion dispersion relation

$$a_t^2 E^2(\boldsymbol{p}) = a_t^2 m^2 + \frac{1}{\xi_f^2} a_x^2 |\boldsymbol{p}|^2. \tag{2.53}$$

Using a few low values for the three-momenta on the lattice, the bare anisotropy was set to 3.4, which again yielded a value of ≈ 3.5.

Chapter 3

Operator Construction

Producing QCD correlators that allow the extraction of excited-state hadron physics requires a careful choice of operators. This chapter discusses the methods used to construct operators which are effective at creating the states we wish to study.

The operators used come in two major types, "single hadron" operators involving fields to create a quark-antiquark pair, and multi-hadron operators which are constructed from the single hadron operators. The goal is to select a set of operators which together can create all expected eigenstates below some energy. In this set, at least one operator should have some coupling to each of the first N states. These operators should be constructed so their couplings to the first N states are large and couplings to higher levels are suppressed.

The first ingredient in making useful operators is to smear the field variables. Smeared fields have dramatically reduced couplings to high energy states. Also, using operators which transfer according to the irreducible representations of the symmetry group of the system helps to block-diagonalize the Hamiltonian, so that we can focus our efforts separately on individual channels.

3.1 Smearing

One method to minimize the coupling to higher energy states is to use smeared quark and gluon fields. Smearing replacing the fields at a given point by a local average of the fields in such a way that all symmetries of the original fields are preserved by the smeared field. In this work, the gluon fields are smeared using the so-called stout smearing method, while Laplacian Heaviside smearing is used for the quark fields.

3.1.1 Stout Smearing

One iteration of stout smearing replaces each link U with a new link U'

$$U'_\mu(x) = \exp\left(iQ_\mu(x)\right) U_\mu(x). \tag{3.1}$$

The use of the exponential keeps the link variable within the Lie group. The matrix Q_μ is Hermitian and trace-less matrix defined as

$$Q_\mu = \frac{i}{2}\left(\Omega^\dagger_\mu(x) - \Omega_\mu(x)\right) - \frac{1}{6}\mathrm{Tr}\left(\Omega^\dagger_\mu(x) - \Omega_\mu(x)\right) \tag{3.2}$$

$$\Omega_\mu(x) = C_\mu(x)U^\dagger_\mu(x) \tag{3.3}$$

where C_μ is a weighted sum of nearby links given by

$$C_\mu(x) = \sum_{\nu\neq\mu} \rho_{\mu\nu}\left[U_\nu(x)U_\mu(x+\hat{\nu})U^\dagger_\nu(x+\hat{\mu})\right. \tag{3.4}$$

$$\left. + U^\dagger_\nu(x-\hat{\nu})U_\mu(x-\hat{\nu})U_\nu(x-\hat{\nu}+\hat{\mu})\right]. \tag{3.5}$$

C_μ is referred to as a *staple* because of the shape it makes with the link variables. The weights $\rho_{\mu\nu}$ are tunable and we selected $\rho_{4\mu} = \rho_{\mu 4} = 0$. This means the smearing is only done in the spatial directions and the temporal links are not smeared nor used in smearing the spatial links. This is done to preserve positively of the transfer matrix for all times. For the rest of the values of ρ, we select a common value so $\rho_{ij} = \rho$.

This procedure is iterative and the updated links can be smeared again using the same procedure to produce a final smeared field $\widetilde{U}$ via

$$U \to U' \to U'' \to \ldots \to U^{(N)} = \widetilde{U} \tag{3.6}$$

The parameters were set to $\rho = 0.14$ with $N = 2$ iterations for the links when used in the action, and set to $\rho = 0.1$ and $N = 10$ for generating operators. The static quark-antiquark potential was used to determine these parameters, as described in Ref. [15].

3.1.2 Quark field smearing

It is also necessary to smear the quark fields. This was done using a method called Laplacian Heaviside (LapH) smearing[16]. The discretized covariant three-dimensional Laplacian operator, ∇^2, is defined as

$$\nabla^2{}_{ab}(x,y,\widetilde{U}) = \sum_{k=1}\left(\widetilde{U}_k^{ab}(x)\delta(y,x+\hat{k}) - 2\delta(x,y)\delta^{ab} + \widetilde{U^\dagger}_k^{ab}(x)\delta(y,x-\hat{k})\right) \tag{3.7}$$

where $\widetilde{U}$ are the stout smeared link variables discussed in the previous section. ∇^2 is rotationally invariant, which makes it a good operator on which to base the quark field smearing. Since ∇^2 is a Hermitian matrix, the eigenvalues are real, and in this case, all negative. Smearing will be effective if the eigenvectors of $-\nabla^2$ with larger eigenvalues are weighted less than the lowest lying ones. One choice is Gaussian smearing,

$$\widetilde{\psi}^A_{a\alpha}(x) = \left(1 - \frac{\sigma}{n}\nabla^2{}_{ab}\right)^n \psi^A_{b\alpha}(x) \tag{3.8}$$

which suppresses the higher eigenmodes exponentially provided that n is large. In the limit of $n \to \infty$, this results in $e^{\sigma\nabla^2}$, where σ is a tunable parameter for the suppression.

The above procedure results in only a small number of modes contributing substantially. An even simpler method is to project down to a subset of the modes and remove the eigenvalues below a threshold, such as

$$\widetilde{\psi}^A_{a\alpha}(x) = \Theta\left(\sigma_s + \nabla^2{}_{ab}\right)\psi^A_{b\alpha}(x) \tag{3.9}$$

where Θ is the Heaviside function. This method is known as Laplacian Heaviside (LapH) smearing. To simplify the smearing in practice, we truncate to a fixed number N_v of eigenvectors on each time slice, which is approximately equivalent to the Heaviside operation. In short, our smearing operator is

$$\mathcal{S} = \sum_{k=1}^{N_v} v^k v^{k\dagger} = VV^\dagger \tag{3.10}$$

where the k^{th} column of V contains the k^{th} eigenvector of the smeared covariant

Laplacian, and the smeared quark fields used in our calculations are defined by

$$\widetilde{\psi}^A_{a\alpha}(x) = \mathcal{S}_{ab}(x,y)\psi^A_{b\alpha}(y). \tag{3.11}$$

We must also consider the $\overline{\psi}$ fields. In Minkowski space $\overline{\psi} = \psi^\dagger\gamma_0$, so creation operators would involve $\overline{\psi}\gamma^0$. In the imaginary time formalism, we consider $\gamma^0 \to \gamma_4$, and it is convenient to introduce

$$\chi \equiv \overline{\psi}\gamma_4. \tag{3.12}$$

Using this, we define the smeared field

$$\widetilde{\chi} = \overline{\psi}^A_{b\alpha}(y)\gamma_4\mathcal{S}_{ab}(x,y). \tag{3.13}$$

Computation of the eigenvectors can be done separately on each time slice and each configuration. The covariant Laplacian is a large matrix for reasonably sized lattices, but computation of the eigenvectors with smallest eigenvalues can be done using an iterative Lanczos method. In this work, the Krylov-Spectral Restarted Lanczos method was used [15], which is a modification of the thick restarted Lanczos method described in Ref. [17].

3.2 Symmetries

Rather than compute the energy of every possible stationary state on the lattice simultaneously, it is possible to restrict to a subset of states. Stationary states can be classified according to how they transform under a system operation, such as a rotation or reflection. Using operators which transform irreducibly according to a symmetry of the Hamiltonian allows us to restrict the analysis to a single *channel* at time. Particles in the continuum are often categorized by J^{PC}, which is spin (J), parity (P), and charge conjugation (C). Unfortunately, due to being in a finite box (and discretized space-time), spin is not a good quantum number, and so lattice states cannot be described this way. This section will discuss the symmetries which are present on the lattice, and construction of operators which transform irreducibly under the available symmetries.

3.2.1 Rotations and Parity

This work aims to compute the spectra of states of QCD in a finite box with periodic boundary conditions. Putting QCD in a box breaks continuous rotational symmetry of space, even in the continuum limit. The finite box and discretized lattice do have symmetry under discrete rotations. The allowed spatial rotations of the cubic lattice are those of the *octahedral group* O.

The group O has 24 elements which can be categorized into 5 conjugacy classes. The elements in each conjugacy class are listed with the number of elements in each class are:

- Identity (1)
- Rotations by $2\pi/3$ and $4\pi/3$ through the 4 corners (8)
- Rotations by π about the x, y or z axes (3)
- Rotations by $\pi/2$ or $3\pi/2$ about axes normal to the cube faces (6)
- Rotations by π through axes through the midpoint of the cubes edge (6)

Since O has 5 conjugacy classes, there are 5 irreducible representations. These representations are named A_1, A_2, E, T_1, and T_2. The A representations are one-dimensional, E is two dimensional, and the T's are three dimensional. The A_1 representation is the identity.

The cubic lattice has an additional symmetry of spatial inversion, or parity. The addition of parity to the group O produces the O_h group. This group has 10 irreducible representations, two for each of the irreducible representations of O one which is even under parity and one which is odd. These are denoted by a subscript g if they are even under parity and u if it is odd under parity (e.g. $A_{1g}, A_{1u}, E_g \ldots$). This comes from *gerade* and *ungerade*, meaning even and odd in German. Superscripts $^+$,$^-$ will be used for G-parity.

3.2.2 Momentum on the lattice

The periodic boundary conditions of the cubic lattice quantize momentum. Momentum is restricted to $\boldsymbol{k} = 2\pi\boldsymbol{n}/L$ where $\boldsymbol{n}$ is a three vector with integer components and L is the spatial length of the lattice. The operators we construct will create states

of definite momentum, and in the case of multi-hadron operators, the building blocks will be hadrons of definite momenta which sum to the desired total momenta. For example, a multi-hadron operator at rest may be composed of single hadrons with opposing momenta.

Considering operators with nonzero momenta reduces the symmetry allowed. Spatial inversion and certain rotations rotate the momentum vector $\boldsymbol{k}$ so the symmetry elements must be restricted those which leave $\boldsymbol{k}$ unchanged. The elements of a subgroup which leave a particular vector unchanged make up the so-called *little group* of $\boldsymbol{k}$. Since we are only after the low energy spectra, we do not have to consider all possible momenta. We restrict our attention to momenta *on axis* (OA) along the x, y, z axes of the lattice, such as $\boldsymbol{k} = (k, 0, 0)$, momenta which are planar diagonal (PD), such as $\boldsymbol{k} = (k, k, 0)$, and momenta directed along a cubic diagonal (CD), such as $\boldsymbol{k} = (k, k, k)$). Other momenta are possible, but the energies of particles with momenta larger than a single unit each of x, y, and z have more energy than the low spectra of interest.

The elements of O_h which preserve an on-axis momentum vector consist of the identity, rotations about the momentum axis by $\pi/2, \pi$ and $3\pi/2$, and then 4 operations which are rotations by π about axis orthogonal to the momentum direction, which flip the momentum vector, followed by a spatial inversion. This eight-element group is denoted C_{4v}. The elements can be grouped into 5 conjugacy classes, so there are 5 irreducible representations. These by convention are named A_1, A_2, B_2, B_2, and E. Each of the irreducible representations is one-dimensional, except for E which is two dimensional.

For planar diagonal and cubic diagonal momenta, the associated little groups are C_{2v} and C_{3v} respectively. The C_{2v} little group only contains 4 elements, each in their own conjugacy class. The group has 4 irreps, which are labeled A_1, A_2, B_1, and B_2. C_{3v} has 6 elements but only 3 irreps labeled A_1, A_2, and E. The details of the little groups, and choices for representation of the matrices, are given in Ref. [18].

3.2.3 Group subductions

The lattice stationary states can be categorized by the lattice symmetries, and so our operators should transform according to the irreps of the symmetry group. However, to compare to experiment, it is needed to say how the lattice states relate to the

continuum particles. It is possible through a method of subduction to determine which irreps of $SO(3)$, J, map onto the irreps of the little groups.

The octahedral group O is a subgroup of $SO(3)$. If we restrict to the subgroup O, we can count the number of times each irreducible representation of O occurs in the subduced representations of $SO(3)$ restricted to O, written $J \downarrow O$ [19]. The results of this subduction are presented in Table 3.1. This shows that for a given stationary state on the lattice, there is not an unambiguous identification of spin. For example, the states produced using T_1 operators will produce states which correspond to $J = 1, 3, 4, 5, \ldots$ in the continuum limit. This provides a major challenge for comparing results on the lattice with experimental results.

J	A_1	A_2	E	T_1	T_2
0	1	0	0	0	0
1	0	0	0	1	0
2	0	0	1	0	1
3	0	1	0	1	1
4	1	0	1	1	1
5	0	0	1	2	1

Table 3.1: The number of times each irreducible representation of the group O occurs in the subduced representations $J \downarrow O$ for values of $J < 6$. Higher J values generally correspond to higher energies.

For certain states of interest, mapping lattice states to continuum states can be done by identifying nearly degenerate energy levels which appear in two or more different lattice channels. For example, for a spin-2 state, 3 polarizations appear in the T_2 irrep, and the other 2 polarizations occur in E.

The other use of subductions is mapping irreps of O_h to the irreps of the little groups for nonzero momenta. This is needed for constructing and choosing operators which we expect to show up in a particular channel. The subductions for O_h onto the three little groups of interest are given in Table 3.2. These map each irrep of O_h to one or more irreps of the little groups. Note that the mappings are different for different parities. For example, the ρ meson has $J^P = 1^-$, so when at rest, it shows up in the T_{1u} lattice channel. The moving ρ with nonzero on-axis momentum will show up in both the A_1 and E lattice channels.

O_h	$\downarrow C_{4v}$	$\downarrow C_{3v}$	$\downarrow C_{2v}$
A_{1g}	A_1	A_1	A_1
A_{1u}	A_2	A_2	A_2
A_{2g}	B_1	A_2	B_2
A_{2u}	B_2	A_1	B_1
E_g	$A_1 \oplus B_1$	E	$A_1 \oplus B_2$
E_u	$A_2 \oplus B_2$	E	$A_2 \oplus B_1$
T_{1g}	$A_2 \oplus E$	$A_2 \oplus E$	$A_2 \oplus B_1 \oplus B_2$
T_{1u}	$A_1 \oplus E$	$A_1 \oplus E$	$A_1 \oplus B_1 \oplus B_2$
T_{2g}	$B_2 \oplus E$	$A_1 \oplus E$	$A_1 \oplus A_2 \oplus B_1$
T_{2u}	$B_1 \oplus E$	$A_2 \oplus E$	$A_1 \oplus A_2 \oplus B_2$

Table 3.2: Subductions of irreducible representations of O_h onto those of the little groups for on-axis, planar-diagonal, and cubic-diagonal momenta. These allow us to construct multi-hadron operators.

3.2.4 Isospin

We use the approximation $m_u = m_d$ in our action, which yields an additional internal symmetry which rotates u quarks into d quarks. This symmetry is an $SU(2)$ symmetry called *isospin*. This means that that u and d quarks can be viewed as two states of an object having isospin $I = \frac{1}{2}$. Choosing an axis in isospin space and quantizing, we designate the u quark to be the state $I_3 = +\frac{1}{2}$ and d to be the $I_3 = -\frac{1}{2}$ state. The s quark has isospin zero. Using this, we can categorize states consisting of u, d, s quarks by their total isospin I and isospin projection I_3, as well as strangeness, and build operators accordingly.

In reality, this isospin symmetry is broken by electomagnetic effects and the fact that the quark masses m_u and m_d are slightly different, so that the $\pi^{\pm}$ and π^0 have different masses, and the proton mass differs from that of the neutron. However, these differences are small, especially compared to the precision of our calculations here. Our computations do not assume any $SU(3)$ flavor symmetry.

3.2.5 G-parity

Another symmetry of QCD is charge conjugation, which transforms a particle into its corresponding antiparticle. However, only uncharged particles, such as the π^0 meson, are eigenstates of charge conjugation. Another symmetry, known as G-parity, consists

of charge conjugation $\mathcal{C}$, plus a rotation by π about the second axis in isospin space:

$$G = \mathcal{C} \exp(-i\pi I_2). \tag{3.14}$$

Particle multiplets which have an average electric charge of zero are eigenstates of G-parity. Our meson operators are constructed (where appropriate) to have definite G-parity. Meson operators which have nonzero strangeness do not have a symmetry under G-parity. The G-parity of a channel is labeled with $+$ or $-$ superscript. Each of the irreps discussed in Sec. 3.2.1 can be projected onto positive or negative G-parity, such as A_{1u}^{+} or A_{1u}^{-}. Recall that spatial parity is represented by the u or g subscripts.

3.3 Covariant Displacements

We expect that hadron resonances are objects with large physical extents. Hadron operators with substantial extents are needed to capture such radial and orbital structure. A simple way to build operators with large extents is to use covariantly-displaced smeared quark fields.

To preserve gauge invariance, displacements must be made using the parallel transporters, that is, the link variables. For a spatial direction j, we define a covariant displacement operator which displaces a field from $x \to x'$ by p lattice sites as

$$D_j^p(x, x') = \widetilde{U}_j(x)\widetilde{U}_j(x + \hat{j}) \ldots \widetilde{U}_j(x + (p-1)\hat{j})\, \delta_{x', x+p\hat{j}} \tag{3.15}$$

Note that these are defined using the smeared link variables as described in Sec. 3.1. To simplify calculations p was fixed to a single value and all displacements were done at the same fixed p. A preliminary study was done and we found $p = 3a_s$ to be a good choice for meson operators. Thus, the basic building blocks of our meson operators are the displaced fields q defined as

$$q = D_j \widetilde{\psi}, \qquad \overline{q} = \widetilde{\chi} D_j^{\dagger} \tag{3.16}$$

where D_j denotes a product of displacements as in Eq. (3.15), yielding a total displacement $\boldsymbol{d} = p(\hat{j}_1 + \hat{j}_2 + \hat{j}_3 + \ldots \hat{j}_n)$. The smeared fields $\widetilde{\psi}$ and $\widetilde{\chi}$ are defined as in Eq. (3.11) and (3.13).

3.4 Single Hadron Operators

Our meson-annihilation operators are superpositions of the following elemental quantities:

$$\Phi^{AB}_{\alpha\beta} = \sum_{x} \exp\left(-i\boldsymbol{p}\cdot\left(\boldsymbol{x}+\frac{1}{2}(\boldsymbol{d}_\alpha+\boldsymbol{d}_\beta)\right)\right)\delta_{ab}\overline{q}^{A}_{a\alpha}(\boldsymbol{x},t)q^{B}_{b\beta}(\boldsymbol{x},t). \tag{3.17}$$

Here the fields q and $\overline{q}$ are the covariantly-displaced LapH-smeared quark fields defined in the previous section. $\boldsymbol{d}_\alpha$ and $\boldsymbol{d}_\beta$ are the total displacements of the respective quark fields. The indices α, and β denote the spin components, and A and B indicate the flavor of the quark field. The δ-function ensures that only a color-singlet combination is formed. The above operator annihilates a definite momentum $\boldsymbol{p}$.

We construct objects of the form 3.17 for a set of fixed shapes. It is hoped that these simple shapes are enough to capture the spatial structure of the desired states. The simplest choice is to have no displacements at all, with both quark and antiquark operator at the same lattice site. This type of object we denote as a single-site (SS) operator. The next simplest shape is to have the quark displaced from the anti-quark in a single direction, denoted singly-displaced (SD). For operators which are not at rest the singly displaced operators come in two forms: transversely-singly-displaced (TSD) if the displacement is perpendicular to the axis of momentum, and longitudinally-singly-displaced (LSD) or planar-singly-displaced (PSD) if the momentum is along the axis of momentum, or in the same plane in the case of PD moving operators.

For operators at rest, we also consider more extended displacements. We can displace both the quark and the anti-quark in perpendicular directions, which we name doubly-displaced-L (DDL). Displacing both the quark and anti-quark along the same axis just results in a singly displaced operator with a larger displacement, which we do not consider. Finally, we consider triply displaced operators of which there are two types; triply-displaced-U (TDU) if two of the displacements are parallel and triply-displaced-O (TDO) if all three displacements are perpendicular. The explicit construction of all of these operators, and a visual representation is given in Table 3.3.

3.4.1 Group theory projections

Having constructed the building blocks as given in the previous section, we use them to construct our final operators. The objects in Eq. (3.17) do not transform according

Illustration	Name	Explicit form ($\|i\| \neq \|j\| \neq \|k\| \neq 0$)
	single-site	$\delta_{ab}\ \widetilde{\chi}^{A}_{a\alpha}\ \widetilde{\psi}^{B}_{b\beta}$
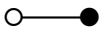	singly-displaced	$\delta_{ab}\ \widetilde{\chi}^{A}_{a\alpha}\ \left(D_j\widetilde{\psi}\right)^{B}_{b\beta}$
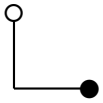	doubly-displaced-L	$\delta_{ab}\ \left(\widetilde{\chi}\ D^{\dagger}_{j}\right)^{A}_{a\alpha}\ \left(D_k\widetilde{\psi}\right)^{B}_{b\beta}$
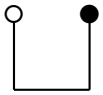	triply-displaced-U	$\delta_{ab}\ \left(\widetilde{\chi}\ D^{\dagger}_{j}\right)^{A}_{a\alpha}\ \left(D_kD_j\widetilde{\psi}\right)^{B}_{b\beta}$
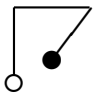	triply-displaced-O	$\delta_{ab}\ \left(\widetilde{\chi}\ D^{\dagger}_{i}\right)^{A}_{a\alpha}\ \left(D_jD_k\widetilde{\psi}\right)^{B}_{b\beta}$

Table 3.3: The five types of displacements we use for our meson elementals are illustrated here. The smeared quark fields are represented by solid circles, the smeared barred antiquark fields by empty circles, and solid lines connecting them indicate displacement operators.

to an irreducible representation of O_h. Linear combinations of them are constructed which do transform irreducibly. The details of this method applied to baryon operators are explained in Ref. [20]. We start with a set of N linearly independent building blocks which transform among each other under O_h. A MAPLE program was used to carry out the needed operator transformations. Using such a set of operators, we construct an $N \times N$ matrix W_{ij} that describes their transformations:

$$U_R \Phi_i(t) U_R^{\dagger} = \sum_{j=1}^{N} \Phi_j(t) W_{ij} \tag{3.18}$$

$$U_R \overline{\Phi}_i(t) U_R^{\dagger} = \sum_{j=1}^{N} \overline{\Phi}_j(t) W^{*}_{ij} \tag{3.19}$$

The elements of W are determined by explicitly transforming the building blocks and using a Moore-Penrose pseudoinverse [21]. Once W is computed, group theoretical projections are used to find the basis-change to produce operators that transform according to the irreducible representations of O_h

Given all elements R of O_h, we can construct linear combinations of the Φ elementals which transform according to a given irreducible representation Λ using the projection

$$O_i^{\Lambda\mu}(t) = \frac{d_\Lambda}{g_{O_h}} \sum_R \Gamma^\Lambda_{\mu\mu}(R) U_R \Phi_i(t) U_R^\dagger, \tag{3.20}$$

where d_Λ is the dimension of the irreducible representation, g_{O_h} is the number of elements in the group, U_R is the operator which effects the group element R and Γ is an explicit matrix representation of the transformation R. This projects onto a single row μ of the representation. Only one row is required as the particle energies are independent of the row of the irrep. Calculations using different rows can be averaged to increase statistics.

Starting with a set of r building blocks, the projections in Eq. (3.20) produce r operators, some of which may be zero or linearly dependent. A Gram-Schmidt procedure is then needed to construct a set of independent projected operators. Since the W matrices may not be unitary, this requires defining an appropriate inner product with a metric defined by

$$M_{ij} = \frac{1}{g_{O_h}} \sum_R \sum_k^N W_{ki}(R)^* W_{kj}(R). \tag{3.21}$$

The resulting operators are expressed as

$$\mathcal{O}_i(t) = \sum_j^N c_{ij} O_j(t) \tag{3.22}$$

where the coefficients c_{ij} satisfy

$$\sum_{k,l}^N c_{ik} M_{kl} c_{jl} = \delta_{ij}. \tag{3.23}$$

These operators are what we refer to as *single-hadron operators* to distinguish them from the operators described in the next section.

3.5 Multi-Hadron Operators

To extract the low-energy spectrum of every channel, we should also include multi-hadron like operators. While in many channels the lowest state may be a single hadron, in some channels one expects two-pions to be the lightest stationary state. Additionally, the excited states above the ground states in most channels will have a plethora of multi-hadron states that are lower in energy than some excited meson resonances. To address these issues, we use multi-hadron operators which use the single-hadron operators of the previous section as the building blocks. The process proceeds much the same way as Sec. 3.4.1, except instead of Eq. (3.17) as the starting point, the fully constructed single-hadron operators are used. We construct multi-hadron operator which create states of definite total momentum.

The first classification of our multi-hadron operators is by flavor. The different combinations of quark flavor fields will produce operators with different strangeness S and isospin I. This section discusses construction of multi-hadron operators of different flavor structure and our naming scheme for such operators to help identify them.

First, consider operators made of only light quark fields, u or d and excluding the strange quark. Here, we have $S = 0$ for any combination. To build a multi-meson operator, each individual meson can have total isospin $I = 1$ or $I = 0$. Combining two of them to form a two-hadron operator allows for isospins of $I = 0$, $I = 1$ or $I = 2$. Since we are working with perfect isospin symmetry, we only have to classify states by their total isospin, and states with different isospin projections I_3 will have degenerate energies. So only one of the projections needs to be considered. Since only one is required, we are free to choose which one and in this work, we always construct operators which have maximal I_3 or $I_3 = I$.

For every combination of flavor structure, we will label the single meson building block by a representative meson with that structure. So for operators with $S = 0$ and $I = 1$, we use the label π as they are *pion-like* operators. This refers only to the flavor structure of the operator and not how it behaves under rotation, parity or G-parity, despite a physical pion having definite properties under those operations.

I	S	Flavor Structure	Label
0	0	$\overline{u}u + \overline{d}d$	η
0	0	$\overline{s}s$	ϕ
1	0	$\overline{u}u$	π
$\frac{1}{2}$	1	$\overline{s}d$	K
$\frac{1}{2}$	-1	$\overline{u}s$	K^c

Table 3.4: The labels given to the creation operators with a given flavor structure. Operators with quark content $\overline{d}u$ are labeled π as a *pion-like* operator. This labeling is independent of other quantum numbers and refers only to flavor.

Likewise, operators with flavor content $\overline{u}u + \overline{d}d$ having $S = 0$ and $I = 0$ are here represented as an η or *eta-like* operator. Including the strange quark, we are able to produce three more flavor structures. Again, $S = 0$ and $I = 0$ is possible with $\overline{s}s$, so such operators are denoted as ϕ operators. The final quark anti-quark combinations are $\overline{s}u$ or $\overline{s}d$ with strangeness $S = 1$ denoted K and finally $\overline{u}s$ or $\overline{d}s$ with strangeness $S = -1$ denoted K^c to indicate charge conjugated versions. The difference between K and K^c on their own does not matter as the spectrum should be the same, but the distinction is required when considering multi-hadron states. These labels are summarized in Table 3.4.

We now want to consider all multi-particle flavor combinations. These can be expressed as combinations of the flavors in Table 3.4. If we take two π, or pion-like operators, together, we can form $I = 0$, $I = 1$ or $I = 2$ states each with $S = 0$. However for $S = 0$ we can make $I = 0$ and $I = 1$ states by the combination $\pi\eta$ or $\pi\phi$ as well. Table 3.5 contains a list of the possible single- and two-particle operators for a given isospin and flavor content.

Since many of the single meson operators have definite G-parity, constructing two-meson operators of a desired G-parity is straightforward. Even G-parity is produced by combining two operators of the same G-parity, and odd G-parity uses single-meson operators with opposite G-parities. Our "kaon" type operators do not have definite G-parity as $U_G K U_G^\dagger = K^c$ and $U_G K^c U_G^\dagger = -K$, but KK^c operators can form operators which create states of definite G-parity via $O^\pm = O \pm U_G O U_G^\dagger$.

$I = I_3$	S	Flavor Content
0	0	$\eta,\ \phi,\ G,\ \eta\eta,\ \eta\phi,\ \phi\phi,\ \pi\pi,\ KK^c$
1	0	$\pi,\ \pi\pi,\ \eta\pi,\ \phi\pi,\ KK^c$
2	0	$\pi\pi$
$\frac{1}{2}$	1	$K,\ K\pi,\ K\eta,\ K\phi$
$\frac{3}{2}$	1	$K\pi$
0	2	KK
1	2	KK

Table 3.5: The type of operators which can appear in each channel, considering only flavor structure. This uses the designations in Table 3.4 to show combinations which produce definite total isospin and strangeness. For some channels, both single hadrons and two-hadron operators appear.

3.6 Operator Selection and Pruning

Ideally, we would like to produce all possible operators which have the correct transformation properties for a given channel. However, limited computer resources requires restricting our attention to prudent choices of operators. Following the above guidelines, there are many different possible operators to construct. For an operator with a given flavor structure and other quantum numbers, there are many different choices for displacements for that operator. Certain displacements could couple poorly to the states of interest, or poorly to all states on the lattice. These operators which couple poorly to states of interest are not worth the computer resources to produce, so we prune them out of the list of produced operators. Additionally, for multi-hadron states, there may be many possible operators which can have the quantum numbers for a channel of interest, but many will be exceedingly high energy states. So a method of selecting which multi-particle operators to use in each channel is needed.

3.6.1 Pruning

Operator selection or "pruning" is somewhat subjective. We followed certain rules of thumb. First, we eliminated operators whose correlators had large statistical errors. Monte Carlo calculations on small 16^3 and 24^3 lattices were done to prune out these noisy operators. The correlators were computed in each channel and sorted by their

type	at rest (single only)	at rest	on axis	planar diagonal	cubic diagonal
π	228	37	47	47	26
K	139	30	30	30	18
η,ϕ	209	63	46	47	39

Table 3.6: The total number of operators produced of each flavor type and momentum direction. These are the totals over all different irreps for the corresponding little group. For isoscalar mesons, the same operators were chosen for our $\overline{\ell}\ell$ (η) and $\overline{s}s$ (ϕ) type.

statistical error, and those with the largest errors were removed from the list. Second, operators which produced correlators whose effective masses (see later) appeared to level off at energies higher than a cutoff energy E_c were discarded, as their couplings to the lower-lying states of interest were deemed too small. We chose

$$a_t E_c = \sqrt{(0.5)^2 - a_t E_\pi(p)^2} \tag{3.24}$$

for momentum p. Third, we removed operators that produced states not sufficiently independent from the states created by other operators. A final set of operators to retain was determined by examining the condition number of the correlation matrix, suitably normalized, of the operators left after step two. Restricting operators whose normalized correlation matrix at an early time separation yields a condition number of less than ≈ 100 gives a reasonable set of approximately twenty or fewer for each channel.

Even with judicious pruning of operators in each channel, the total number of operators remained large due to the number of possible channels and allowed momenta. The number of operators which we considered computing are in Table 3.6.

3.6.2 Two-hadron Operator Selection

The pruning process limits the number of single-hadron operators we consider to a reasonable number, but for a given channel, there are still a huge number of possible two-hadron operators. Table 3.5 gives the list of possible flavor combinations for each channel. Since it is not feasible to include all possible two-hadron operators, we must have some guiding principle to select which operators to include.

In the absence of hadron interactions, the energies and natures of all free two-

hadron states is easily known using symmetry, the known single-particle energies, and the available momenta on the lattice. MAPLE code was written to discover all of these states below a certain energy-cutoff. We then use these lists of expected free two-meson states as a guide in selecting two-hadron operators. In each channel, we make sure to include at least one operator, known as a *primary* operator, that should couple strongly to each stationary state corresponding to each expected free level. It is not essential to include an operator which approximates each of the stationary states in a channel as the operator will have overlaps with many states, but getting a set which is closer hopefully produces a better signal. Additional so-called *secondary* operators were also added to ensure our computations would capture all two-meson states in the interacting theory.

For example, consider the $I = 1/2$, $S = 1$, T_{1u} channel with total momentum zero. Given the available momenta, we expect the $K^*(892)$ meson at rest to be the lightest state in this channel. Assuming small hadron-hadron interactions, the second lowest state in the channel on our 32^3 lattice is expected to be a pion-kaon state with each having a single unit of momentum back to back. So we would include operators which is expected to pick up that level, choosing an operator built from a pion-like operator which transforms as A_{2m} and a kaon-like operator which transforms as A_2. The next lowest state is again expected to be a pion-kaon state with each having minimal nonzero planar-diagonal opposite momenta, and so on.

One could have simply chosen a random assortment of operators, including all possible flavor combinations which are allowed in the channel of interest. Since the operators we make will never exactly correspond with the actual stationary states any given operator will create a linear combination of many or all of the stationary states. By choosing operators to match the non-interacting spectrum, we except the operators will have strong overlaps with all of the low energy states resulting in a stronger signal. Now that the process of operator selection has been discussed we proceed to the next chapter on how to evaluate the operators to produce the correlation functions.

Chapter 4

Computing the Correlators

Sec. 2.2 introduced two-point correlation functions in terms of path integrals. This section outlines how the correlators are evaluated. The idea of a quark line is introduced to describe propagation of the quarks. These quark lines require multiplying the inverse of the Dirac matrix onto certain vectors. This is computationally expensive, especially for correlators involving multi-hadron operators. Such computations are made feasible using the stochastic LapH method.

4.1 Quark Lines

Recall from Sec. 2.2.1 that the fermion fields are integrated out, yielding functions $F[\mathcal{M}^{-1}, U]$ involving products of $\mathcal{M}^{-1}$ that depend on the quark fields present in the operators for a particular correlator. Evaluating the correlator using Eq. (2.34) comes down to simply evaluating $F[\mathcal{M}^{-1}, U]$ using the configurations in a Monte Carlo ensemble and averaging. This section describes the form of $F[\mathcal{M}^{-1}, U]$ needed for a correlator of interest. The combinations of Dirac matrix inversions needed are determined by Wick's theorem.

Our single hadron creation operators $\overline{\mathcal{O}}_i$ are given in Eq. (3.22) and are built from objects given in Eq. (3.17). A correlation function between an operator which creates a single meson $\overline{\mathcal{O}}$ and a similar annihilation operator $\mathcal{O}$ has the form

$$C(t_F - t_0) = c^{f_1}_{\alpha\beta} c^{f_2}_{\alpha'\beta'} \frac{1}{N_t} \sum_{t_0} \sum_{xx'} e^{-ip(x+\frac{1}{2}(d_\alpha + d_\beta))} e^{-ip(x'+\frac{1}{2}(d'_\alpha + d'_\beta))} \times \left\langle \overline{q}_{a\alpha}(x, t_f) q_{a\beta}(x, t_f) \overline{q}_{a'\beta'}(x', t_0) q_{a'\alpha'}(x', t_0) \right\rangle . \quad (4.1)$$

The first trick is to employ invariance under time translations to realize one does not have to evaluate on all values t_0. This means we can fix the time of the source operator to one (or a few) times to reduce the computational cost. A similar trick can sometimes be used to not have to evaluate the source at all spatial sites, as long as the summation at the sink time is maintained to project out the definite momentum. This is known as the point-to-all method and works very well when it can be applied. The problem is that this method cannot be applied if the operators require contractions of the fields on the same sink-to-sink time slice, such as for isoscalar mesons, or the source operator involves more than one summation over sites, such as in a multi-hadron operator.

To illustrate the problem with using the point-to-all method, we explicitly evaluate a path integral over the fermion fields. For isovector mesons involving u and d quarks given by

$$\overline{O}_v(x,t) = \sum_{x_0} e^{ip\cdot x}\overline{q}^u_{a\alpha}(x,t)q^d_{a\beta}(x,t) \tag{4.2}$$

$$O_v(x,t) = \sum_{x'} e^{ip'\cdot x}\overline{q}^u_{b\alpha'}(x,t)q^d_{b\beta'}(x,t) \tag{4.3}$$

the Grassman integrations lead to

$$F(\mathcal{M}^{-1}) = -\sum_{x,x'} e^{ip\cdot x}e^{ip'\cdot x'}\mathcal{M}^{-1}{}^d_{b\beta',a\alpha}(x,t|x_0,t_0)\mathcal{M}^{-1}{}^u_{a\beta,b\alpha'}(x_0,t_0|x,t). \tag{4.4}$$

For isoscalar meson operators involving terms such as

$$\overline{O}_s(x,t) = \sum_{x_0} e^{ip\cdot x}\overline{q}^u_{a\alpha}(x,t)q^u_{a\beta}(x,t) \tag{4.5}$$

$$O_s(x,t) = \sum_{x'} e^{ip'\cdot x}\overline{q}^u_{b\alpha'}(x,t)q^u_{b\beta'}(x,t) \tag{4.6}$$

there is an additional way to do the contractions, giving two terms

$$\begin{aligned} F(\mathcal{M}^{-1}) = &-\sum_{x,x'} e^{ip\cdot x}e^{ip'\cdot x'}\mathcal{M}^{-1}{}^u_{b\beta',a\alpha}(x,t|x_0,t_0)\mathcal{M}^{-1}{}^u_{a\beta,b\alpha'}(x,t|x_0,t_0) \\ &+\sum_{x,x'} e^{ip\cdot x}e^{ip'\cdot x'}\mathcal{M}^{-1}{}^u_{b\beta',b\alpha'}(x,t|x,t)\mathcal{M}^{-1}{}^u_{a\beta,a\alpha}(x_0,t_0|x_0,t_0). \end{aligned} \tag{4.7}$$

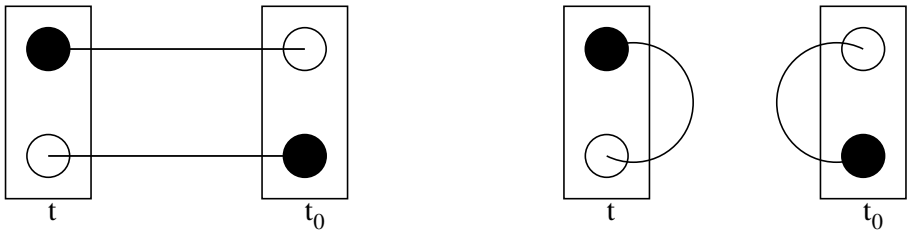

(a) Connected diagram (b) Disconnected diagram

Figure 4.1: Possible contractions for correlators of a single meson source and a single meson sink. The disconnected diagram contributes only in the case of isoscalar mesons.

The contractions for this are shown graphically in Fig. 4.1. Each of the diagrams corresponds to a term in F. The lines in each diagram are the result of a particular contraction between a ψ and χ, which we refer to as a *quark line*. Defining $\Omega = \gamma_4 \mathcal{M}$, then a quark line describing the propagation of $\overline{q} = \widetilde{\chi} D_j^\dagger$ at t_0 to a $q = D_j \widetilde{\psi}$ at t is

$$Q_{ij}(t, t_0) = D_i \mathcal{S} \Omega^{-1}(t, t_0) \mathcal{S} D_j^\dagger. \tag{4.8}$$

There are three types of quark lines. A *forward-time* quark line connects a χ at the source time to a ψ at the sink, a *backward-time* quark line connects a χ at a later time t to a ψ at an earlier time t_0, and a *same-time* line which connects ψ and χ on the same time slice. The details of computing these are discussed in Sec. 4.2.3.

The graphical representation in Fig. 4.1 is useful to visualize the Wick contractions of a particular correlator. The number of possible quark line connections increases when dealing with multi-hadron operators. The possible Wick contractions for a correlator of a meson-meson source to a meson sink are shown in Fig. 4.2. Not all diagrams may contribute, depending on the flavor of the quarks in the mesons involved. Diagrams which depict a contraction of quarks of different flavors are taken to be zero. For example, each of the diagrams involving quark lines that start and end inside the same meson are zero unless that meson is an isoscalar.

There are 24 possible contributing diagrams for the case of a two-meson source to a two-meson sink. These are shown in Fig. 4.3. Again, only the diagrams which connect quarks of the same flavor contribute. Here, we can see there are many diagrams which involve same-time quark lines.

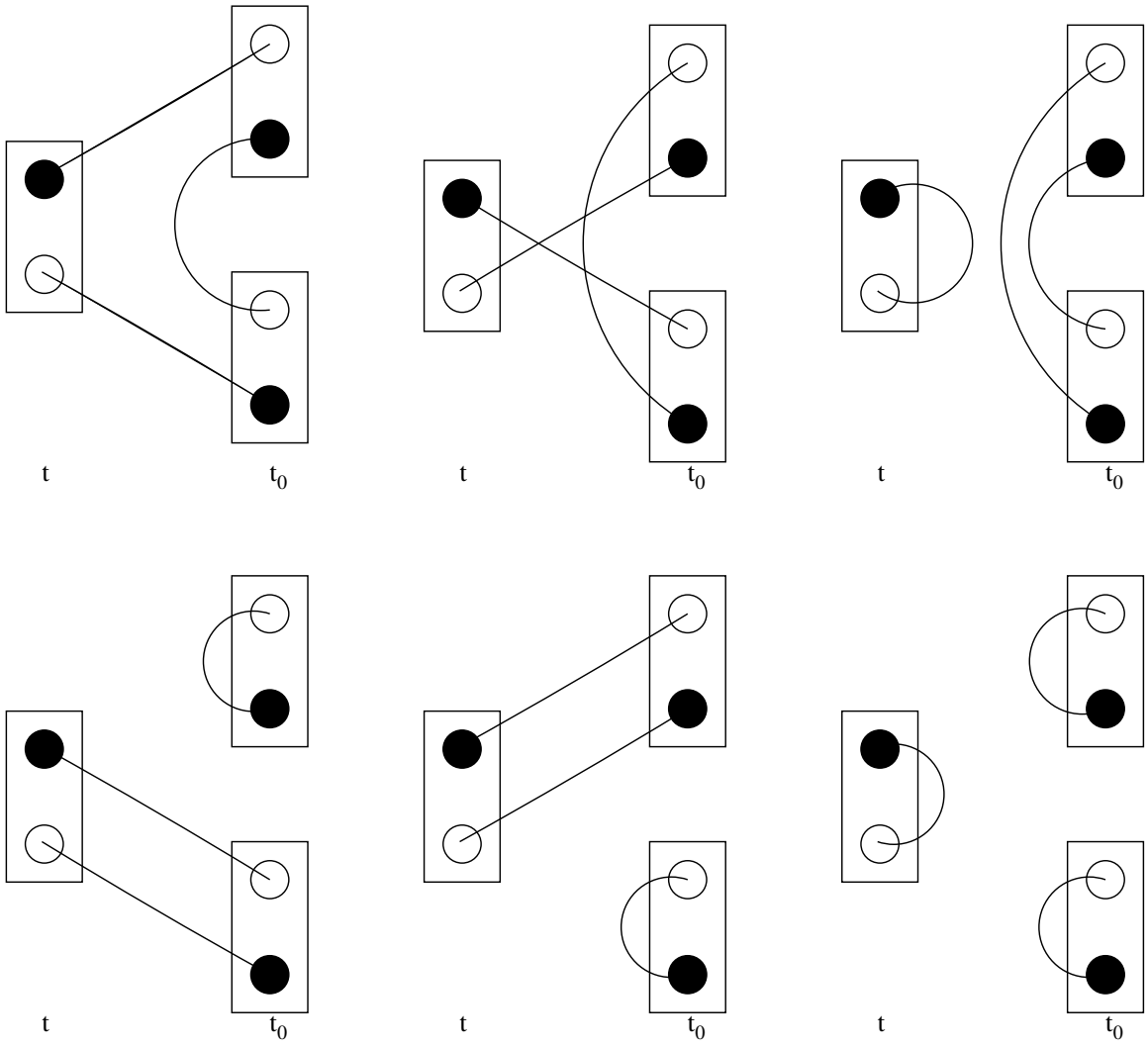

Figure 4.2: All possible Wick contractions for a meson-meson source to a single-meson sink. For a particular correlator, these are summed with appropriate signs, excluding any diagrams which connect two quarks of different flavors. A similar set of diagrams exists corresponding to the contractions for a single meson at the source and a meson-meson sink.

4.2 Stochastic LapH Method

Since all of our calculations are computed within a Monte Carlo estimate, exact inversions of the Dirac matrix are not needed. The statistical error due to the variance of the field configurations generated by our Markov chain is known as the *gauge noise limit*. What is needed is a method which is computationally easy which can approximate the inversion to an accuracy comparable to that of our Monte Carlo

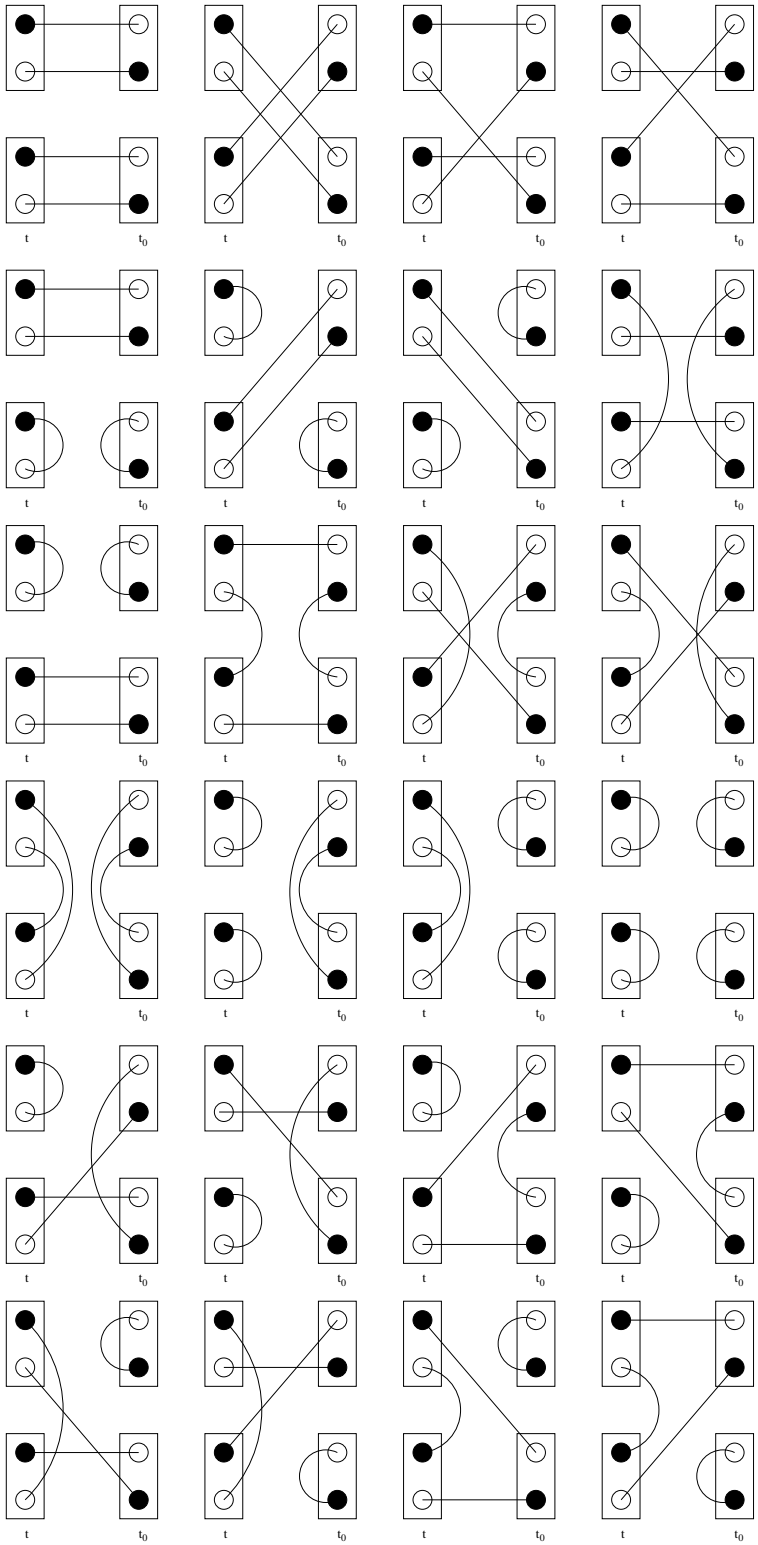

Figure 4.3: All possible Wick contractions for a meson-meson source to a meson-meson sink. For a particular correlator, these are summed with appropriate signs, excluding any diagrams which connect two quarks of different flavors.

estimates. We use the stochastic LapH method[15] to estimate the many quark lines involved in our correlators.

4.2.1 Stochastic estimation of matrix inverses

In one way to stochastically estimate a matrix inverse, a set of random noise vectors ρ_k are introduced, where the value of each component is randomly chosen from $1, -1, i, -i$ with equal probability, referred to as Z_4 noise. There are other possible choices for the noise vectors, but it is required that the noise vectors satisfy

$$E(\rho) = 0 \quad \text{and} \quad E(\rho\rho^\dagger) = I, \tag{4.9}$$

where $E(\rho)$ denotes the expected value. Other possible choices of noise could be Gaussian noise, $U(1)$ noise or other choices of Z_n noise. The choice of Z_4 is simple and has the desirable property that $\rho\rho^* = 1$ exactly, not just on average. To estimate the inverse of a matrix using such random noise vectors, the linear system $MX = \rho$ is solved for X. Once X is found, the expectation value of $X\rho$ yields the matrix inverse:

$$E(X_i\rho_j^*) = E\left(\sum_k M_{ik}^{-1}\rho_k\rho_j^*\right) = \sum_k M_{ik}^{-1}E(\rho_k\rho_j^*) = M_{ij}^{-1}. \tag{4.10}$$

Using this method, the inverse of M can be approximated by solving for X using many different random vectors and averaging.

Meson correlators contain products of Dirac matrix inverses, which can also be estimated stochastically. To estimate a product of matrix inverses without bias, two random noise vectors are used. Again, $MX^{(a)} = \rho^{(a)}$ is solved for $X^{(a)}$ and the product of inverses can be estimated by

$$E\left(X_i^1\rho_j^{1*}\, X_k^2\rho_\ell^{2*}\right) = \sum_p\sum_q M_{ip}^{-1}M_{kq}^{-1}E\left(\rho_p^2\rho_j^{1*}\,\rho_q^2\rho_\ell^{2*}\right) = M_{ij}^{-1}M_{k\ell}^{-1}. \tag{4.11}$$

In the case of two-meson correlators, there will be products of four inverses, which is a simple extension of this process. A noise vector is required for each quark line.

4.2.2 Variance Reduction using Noise Dilution

The stochastic method described above yields estimates with unacceptably large errors. Also, the error decreases only as $1/\sqrt{N}$ for N noise vectors. A significant variance reduction can be achieved using a method of *dilution*[22] by breaking the noise vectors into a sum of noise vectors $\rho = \sum_d \rho^{(d)}$. The inversions are then done on each of the smaller noise vectors and then summed to get the result.

A dilution scheme is defined by a set of projectors P^a. The vectors are then defined as a sum over projectors

$$\rho = \sum_a P^a \rho^a. \tag{4.12}$$

Since the inversions are done on each ρ^a, one can choose a set of projectors which gives the desired variance.

All-to-all correlators have values for each time slice, spatial location, color index, and spin index. We must introduce projectors which have support on only some of these values to minimize the number of inversions needed, while still getting good convergence to the exact correlator. We would like a dilution scheme which gives good results for a minimal number of projectors. For example, spatial dilution could be done "even-odd", in which each projector has support on either the even or odd sites on the lattice. Options such as blocking, where each projector has support on a group of adjacent indices, or interlacing, where each has support on every nth index for some value of n, are possible choices.

Since we are using LapH smeared quark fields, a dramatic reduction in variance can be achieved by introducing noise only in the LapH subspace. Recall from Sec. 3.1.2 that our smeared quark fields are defined using $VV^\dagger$, where the columns of V are the lowest-lying eigenvectors of minus the gauge-covariant Laplacian. The matrix V has $N_t N_s^3 N_c$ rows but the number of columns is $N_v N_t$ where N_v are the number of eigenmodes included on each time slice. We can then use random noise vectors of the form $\rho_{t\alpha n}$, where t indicates time, α is a Dirac spin component, and n is a LapH eigenvector number. Fig. 4.4 illustrates the reduction in the number of inversions required to get a small error between lattice noise and noise in the LapH subspace.

The LapH dilution schemes are denoted by a triplet (T,S,L) for time, spin and LapH eigenvector. Many different schemes were tested and the results are discussed in Ref. [23]. These tests were done on a small lattice where the exact results were

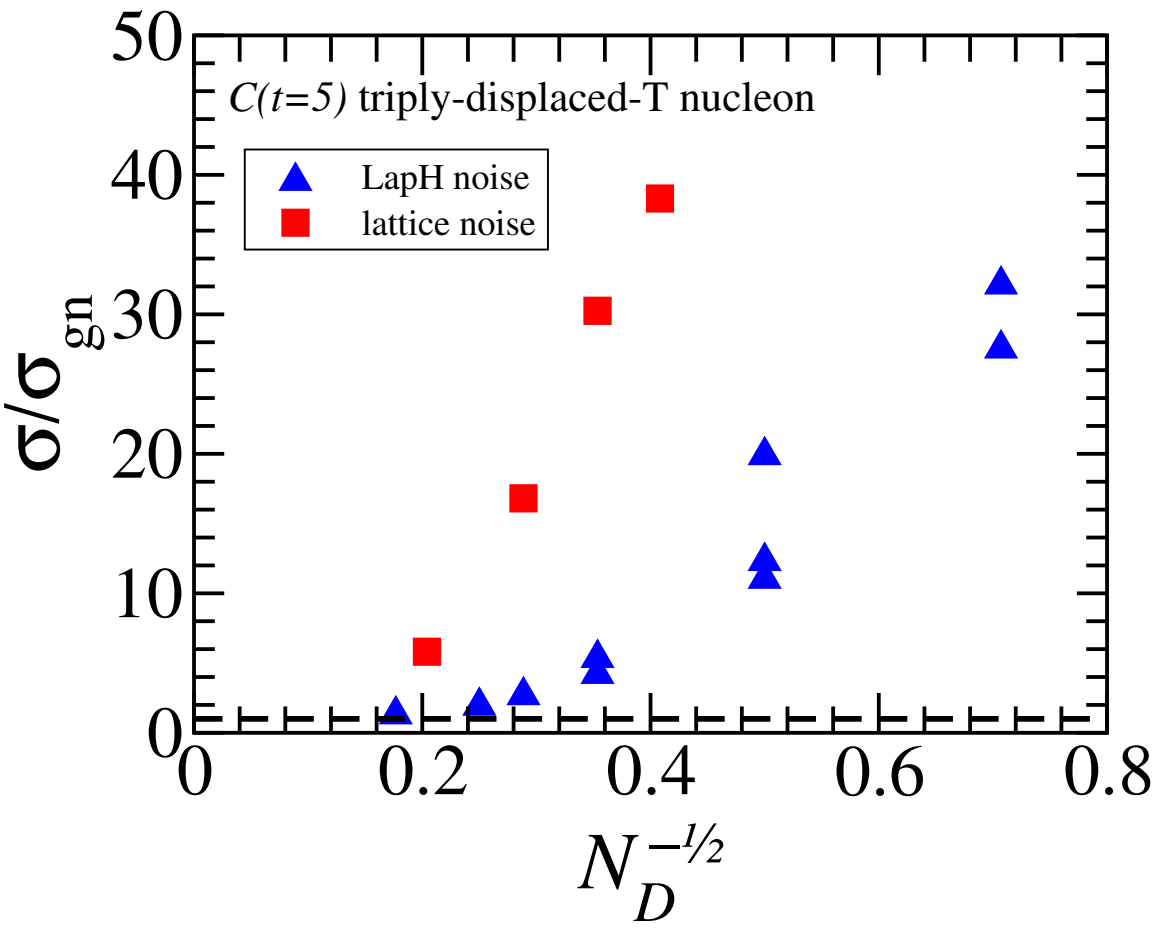

Figure 4.4: Comparison of the statistical error σ relative to the limiting noise from the gauge configurations σ_g using noise in the LapH subspace, or using the spatial lattice points and color. N_D is the number of dilution projectors. Results from the 16^3 lattice.

feasible to compute so they could be compared with the various dilution schemes. It was found that, provided there are enough projectors in the LapH subspace, there was little difference between interlacing or blocking the indices. It was also found that employing full spin dilution significantly reduced the variance in some disconnected diagrams. Using those tests, it was decided, for quark lines on different times, to use a dilution scheme of (TF, SF, LI8), which is full dilution in time and spin, and interlacing in the LapH subspace where each projector has support on every 8th eigenvector number. For quark lines which are on the same time, the dilution scheme (TI16, SF, LI8) was selected.

4.2.3 Stochastic Estimates of the Quark lines

Our quark lines are of the form

$$Q_{ij} = D_i V V^\dagger \Omega^{-1} V V^\dagger D_j^\dagger, \tag{4.13}$$

using Eq. (3.10) with $\mathcal{S} = VV^\dagger$ and $\Omega = \gamma_4 \mathcal{M}$. Since our diluted random noise vectors are in the LapH subspace, we insert them between the rightmost V matrices and our stochastic estimates have the form

$$Q_{ij} = \sum_a D_i V V^\dagger \Omega^{-1} V \, P^a E(\rho\rho^\dagger) P^{a\dagger} \, V^\dagger D_j^\dagger \tag{4.14}$$

$$= \sum_a E\left(\left(D_i V V^\dagger \Omega^{-1} V P^a \rho \right) \, \left(P^a V D_j \rho \right)^\dagger \right). \tag{4.15}$$

We define a stochastic source and sink by

$$\varrho_i^a(\rho) = D^i V P^a \rho, \tag{4.16}$$

$$\varphi_i^a(\rho) = D^i \mathcal{S} \Omega^{-1} V P^a \rho, \tag{4.17}$$

where ρ is a noise vector in time, spin and LapH eigenvector index. For each dilution projector, we must solve the linear system

$$\Omega X^a = V P^a \rho \tag{4.18}$$

for X such that $X = \Omega^{-1} V P^a \rho$. Obtaining these solutions is the most expensive part of the computations. Then our quark lines are estimated according to

$$Q_{ij} \approx \frac{1}{N} \sum_{n=1}^{N} \sum_a \varphi_i^a[n] \varrho_j^{a\dagger}[n]. \tag{4.19}$$

The stochastic sources and sinks are computed and combined into single-hadron sources and sinks. These are stored on disk and later combined to make all needed correlators. The factorization of the source and sink hadrons is an incredibly useful advantage of the stochastic LapH method. It dramatically simplifies the task of forming the correlators of many different operators.

To estimate backwards-time quark lines, one does not need to compute anything

new since we can take advantage of γ_5-Hermiticity to switch the source and the sink. Since $\mathcal{M}^\dagger = \gamma_5 \mathcal{M} \gamma_5$, $Q^\dagger$ can be found from

$$\begin{aligned} Q^\dagger &= \left(D\mathcal{S}\Omega^{-1}\mathcal{S}D^\dagger\right)^\dagger = D\mathcal{S}\Omega^{-1\dagger}\mathcal{S}D^\dagger = D\mathcal{S}\left(\gamma_4\mathcal{M}^{-1}\right)^\dagger \mathcal{S}D^\dagger \\ &= \gamma_4 D\mathcal{S}\left(\gamma_5\mathcal{M}^{-1}\gamma_5\right)\mathcal{S}D^\dagger = \gamma_4\gamma_5 D\mathcal{S}\mathcal{M}^{-1}\gamma_4\gamma_4\mathcal{S}D^\dagger\gamma_5 \\ &= -\gamma_5\gamma_4 Q\gamma_4\gamma_5, \end{aligned} \tag{4.20}$$

using $\gamma_4^2 = 1$ and the fact that the γ-matrices anti-commute. Define

$$\overline{\varrho}_i^a(\rho) = -\gamma_5\gamma_4\varrho \tag{4.21}$$

$$\overline{\varphi}_i^a(\rho) = \gamma_5\gamma_4\varphi, \tag{4.22}$$

and replace these for their counterparts in Eq. (4.19).

4.3 Computing Correlators

The stochastic LapH method allows us to estimate the quark lines needed for evaluating all temporal correlators. In summary, the steps involved in estimating the correlators using any Monte Carlo ensemble of gauge configuration are as follows:

- Evaluate the smeared gauge fields $\widetilde{U}$
  Although the dependence on $\widetilde{U}$ was left off in this chapter, the quark lines and stochastic sources all depend on the gauge field configurations generated using the methods in Sec. 2.3.1. These are smeared using stout smearing and stored on disk for each configuration.

- Evaluate the LapH eigenvectors V
  Using the smeared gauge fields on each configuration, the low-lying eigenvectors of the Laplacian are computed and stored on disk. These are used to smear the quark fields and must be read from disk when computing the stochastic sources and sinks. Only N_v vectors are computed and stored, where N_v is chosen for each lattice depending on its size.

- Randomly generate the noise vectors ρ
  For each gauge configuration, a set of Z_4 random noises are produced. These random noises are produced in the LapH subspace for each time and spin index.

The random values are produced using the Mersenne twister[24] pseudo-random number generator.

- Evaluate the quark sinks φ
  Using the random vectors ρ, quark sinks are computed by solving the linear system $\Omega X^a = VP^a\rho$ for X for each dilution projector. A multi-precision biconjugate gradient method is used. These solutions are obtained for each noise vector on each configuration. The quark sources can simply be computed when needed on the fly from ρ and V, which are already on disk.

- Compute the single-hadron sources and sinks
  Ultimately we want correlators between operators which have definite momenta and transformation properties as discussed in Chapter 3. These operators are produced by combinations of quark sinks and sources with some set of coefficients. So the φ, ϱ, $\overline{\varphi}$, and $\overline{\varrho}$ are put together to make the single-hadron line ends.

Once the operators are stored on disk, they are assembled into correlation functions. A set of operators of interest is used to make many correlators with the same quantum numbers allowing us to extract information about the energies of the stationary states on the lattice. The analysis of the correlation functions is discussed in the next chapter.

Chapter 5

Scattering Phase Shifts from Finite-Volume Energies

Monte Carlo calculations in lattice QCD are necessarily carried out in finite volume. However, most of the excited hadrons we seek to study are unstable resonances. In finite volume with particular boundary conditions, the eigenstates of the Hamiltonian are discrete since only certain momenta are allowed in order to satisfy the boundary conditions. Diagonalization of the Hamiltonian leads to a knowledge of the discrete stationary states. In infinite volume, a continuum of momenta are available and unstable excited hadrons decay to multi-hadron asymptotic states. In finite volume, there are no decays; instead, there is only quantum mechanical mixing between the Fock states. Fortunately, it is still possible to study the excited resonances by using finite-volume calculations. In this chapter, we show how the finite-volume stationary-state energies are related to particular infinite-volume scattering phase shifts. Once these phase shifts are determined, resonance energies and widths can then be deduced.

The idea that finite-volume energies can be related to infinite-volume scattering processes is actually rather old, dating back to Refs. [25, 26] in the mid-1950s. First suggestions of applying such techniques for gauge field theories appeared in Ref. [27]. In Ref. [28] in 1986, Lüscher studied the volume dependence of the energy spectrum of stable particle states in massive quantum field theories, then examined the volume dependence of scattering states in Ref. [29] soon thereafter. In Ref. [30] in 1991, Lüscher then found relationships between finite-volume energies and infinite-volume scattering phase shifts in the case of two identical spinless particles having zero total momentum and interacting via a central potential. The advantages of using sectors

with non-zero total momenta were then described by Rummukainen and Gottlieb in Ref. [31] in 1995. These calculations were later revisited in 2005 using an entirely field theoretic approach in the key work of Kim, Sachrajda, and Sharpe in Ref. [32]. This work focused on the case of a single channel of identical spinless particles, but the total momentum could be any value allowed by the boundary conditions. As lattice QCD computations improved to the point where it is now becoming possible to calculate scattering phase shifts with reasonable accuracy, the results of Ref. [32] were eventually generalized in Refs. [33–37], among others, to treat multi-channels with different particle masses and nonzero spins.

This chapter mainly follows Ref. [32], but the derivation has been generalized to arbitrary masses and spins and numbers of channels. The calculations are rather lengthy and complicated, but the final formulas that will be needed end up being fairly simple, when expressed in terms of certain generalized zeta functions.

5.1 Two-particle states and scattering phase shifts

We begin with a brief review of single- and two-particle states. For a detailed description of such states, see Refs. [38–40]. We then introduce the partial wave scattering phase shifts.

The concepts of orbital angular momentum and intrinsic spin can be generalized to relativistic situations using the Pauli-Lubanski tensor:

$$W^\mu = -\tfrac{1}{2}\epsilon^{\mu\nu\alpha\beta} M_{\nu\alpha} P_\beta, \tag{5.1}$$

where P^μ generates space-time shifts (a four momentum) and the antisymmetric tensor M combines generators of rotations and boosts:

$$K^i = M^{0i}, \qquad J^i = \frac{1}{2}\epsilon^{ijk} M_{jk}. \tag{5.2}$$

Note that

$$W^0 = \boldsymbol{P}\cdot\boldsymbol{J}, \qquad \boldsymbol{W} = P^0\boldsymbol{J} - \boldsymbol{P}\times\boldsymbol{K}. \tag{5.3}$$

For a particle of nonzero mass m, $P_\mu P^\mu = m^2$ and one can define intrinsic spin $\boldsymbol{S}$ and

orbital angular momentum $\boldsymbol{L}$ using

$$\begin{aligned} m\boldsymbol{S} &= \boldsymbol{W} - (m + P^0)^{-1}\boldsymbol{P}W^0, \quad (5.4) \\ \boldsymbol{L} &= \boldsymbol{J} - \boldsymbol{S}. \quad (5.5) \end{aligned}$$

Note that $\boldsymbol{S}^2 = -W^\mu W_\mu/m^2$ is a Lorentz invariant and that S^i and L^i satisfy the following:

$$\begin{aligned} [\ P^\mu, \boldsymbol{S}\ ] &= \boldsymbol{0}, & \boldsymbol{P}\cdot\boldsymbol{L} &= 0, \\ [\ S^i, S^j\ ] &= i\ \epsilon^{ijk}\ S^k, & [\ L^i, L^j\ ] &= i\ \epsilon^{ijk}\ L^k, \\ [\ J^i, S^j\ ] &= i\ \epsilon^{ijk}\ S^k, & [\ L^i, S^j\ ] &= 0. \end{aligned} \quad (5.6)$$

Single particle states can be labeled using the eigenvalues of a set of mutually commuting observables: the mass m from the eigenvalue m^2 of $P^\mu P_\mu$, where P^μ is the four-momentum operator, three-momentum $\boldsymbol{p}$ from the spatial components of P^μ, the spin s from the eigenvalue $s(s+1)$ of $-W^\mu W_\mu/m^2$, and a spin projection λ, usually the helicity from $(\boldsymbol{J}\cdot\boldsymbol{P})(\boldsymbol{P}\cdot\boldsymbol{P})^{-1/2} = (\boldsymbol{S}\cdot\boldsymbol{P})(\boldsymbol{P}\cdot\boldsymbol{P})^{-1/2}$ or the eigenvalue of S_3. We denote the single-particle states of definite momentum by $|\boldsymbol{p}s\lambda\rangle$ and the conventional normalization of such states has the Lorentz invariant form

$$\langle \boldsymbol{p}'s\lambda'|\boldsymbol{p}s\lambda\rangle = (2\pi)^3(2E_p)\delta^{(3)}(\boldsymbol{p}' - \boldsymbol{p})\delta_{\lambda'\lambda}, \quad (5.7)$$

where $E_p = \sqrt{\boldsymbol{p}^2 + m^2}$. The spin s is an intrinsic property of each particle, just like the mass m, which has only one value for each particle type. States of different particle types are taken to be orthogonal.

Two-particles states can be built out of direct products of these,

$$|\mathbf{p}_1 s_1\lambda_1, \mathbf{p}_2 s_2\lambda_2\rangle = |\mathbf{p}_1 s_1\lambda_1\rangle \otimes |\mathbf{p}_2 s_2\lambda_2\rangle. \quad (5.8)$$

To simplify notation, we will suppress the explicit s_1, s_2 quantum numbers in the two-particle basis states. These will be assumed implicit. The usual normalization convention for these states (for distinguishable particles) is the Lorentz invariant form below:

$$\langle \mathbf{p}'_1\lambda'_1; \mathbf{p}'_2\lambda'_2|\mathbf{p}_1\lambda_1; \mathbf{p}_2\lambda_2\rangle = 4E_1E_2(2\pi)^6\delta^{(3)}(\boldsymbol{p}'_1 - \boldsymbol{p}_1)\delta^{(3)}(\boldsymbol{p}'_2 - \boldsymbol{p}_2)\delta_{\lambda'_1\lambda_1}\delta_{\lambda'_2\lambda_2}, \quad (5.9)$$

where $E_1 = \sqrt{\boldsymbol{p}_1^2 + m_1^2}$ and $E_2 = \sqrt{\boldsymbol{p}_2^2 + m_2^2}$.

Such two-particle states have definite total linear momentum and relative momentum, but when dealing with scattering phase shifts, it is more convenient to work with states that have definite total linear momentum and definite *angular* momentum in the cm frame instead. As a first step towards creating such states, make a change of variables from $\boldsymbol{p}_1, \boldsymbol{p}_2$ to $\boldsymbol{P} = \boldsymbol{p}_1 + \boldsymbol{p}_2$ and $2\boldsymbol{q} = \boldsymbol{p}_1 - \boldsymbol{p}_2$, then express the relative momentum $\boldsymbol{q}$ in spherical components: magnitude q, polar angle θ, and azimuthal angle ϕ. Lastly, replace q by $E = P^0 = E_1 + E_2$, where $P = (P^0, \boldsymbol{P})$ is the total four momentum. With these variables, we label the two-particle states by $|P\Omega\lambda_1\lambda_2\rangle$, introducing the solid angle $\Omega = (\theta, \phi)$ and again suppressing the explicit s_1, s_2 labels, remembering that they are implicit. The normalization of the two-particle states in terms of these variables is given by

$$\langle P'\Omega'\lambda_1'\lambda_2'|P\Omega\lambda_1\lambda_2\rangle = \frac{4P^0}{q}(2\pi)^6\delta^{(4)}(P'-P)\delta^{(2)}(\Omega'-\Omega)\delta_{\lambda_1'\lambda_1}\delta_{\lambda_2'\lambda_2}. \tag{5.10}$$

Because these two-particle states are eigenstates of total four-momentum P^μ, it is often useful to write such states as

$$|P\Omega\lambda_1\lambda_2\rangle = (2\pi)^3\left[\frac{4P^0}{q}\right]^{1/2}|\Omega\lambda_1\lambda_2\rangle \otimes |P\rangle, \tag{5.11}$$

where the normalizations are chosen to be

$$\langle P'|P\rangle = \delta^{(4)}(P'-P), \tag{5.12}$$

$$\langle \Omega'\lambda_1'\lambda_2'|\Omega\lambda_1\lambda_2\rangle = \delta^{(2)}(\Omega'-\Omega)\delta_{\lambda_1'\lambda_1}\delta_{\lambda_2'\lambda_2}. \tag{5.13}$$

In order to construct states with definite total angular momentum, we must first make a choice of spin projection type. Often, it is most convenient to choose helicity which uses the direction of the momentum as the spin projection axis. Our goal here is to relate finite-volume energies to partial wave scattering phase shifts. Partial waves are generally defined in terms of parity eigenstates, and helicity states are not eigenstates of parity. States in the so-called LS basis, where S denotes the total intrinsic spin of the two particles, and L is related to the relative orbital angular momentum, are parity eigenstates, so we prefer to work in the LS basis. Since it is easier to form the LS states using single-particle states which are eigenstates of S_3,

we choose the z-axis as our spin projection axis.

For two-particle systems, intrinsic spin can be generalized by defining the two-body spin operators

$$\boldsymbol{S} = \boldsymbol{S}_1 + \boldsymbol{S}_2, \tag{5.14}$$

where $\boldsymbol{S}_1$ and $\boldsymbol{S}_2$ are the spins of particles 1 and 2, respectively. In the cm frame, the two-particle state with total spin S can be defined in terms of single particle states in the standard way,

$$|\Omega S m_S\rangle = \sum_{m_{s_1}, m_{s_2}} |\Omega, s_1 m_{s_1}, s_2 m_{s_2}\rangle \langle s_1 m_{s_1}, s_2 m_{s_2} | S m_S\rangle, \tag{5.15}$$

where $\langle s_1 m_{s_1}, s_2 m_{s_2} | S m_S\rangle$ denotes a Clebsch-Gordan coefficient. Lastly, we can transform from angular coordinates to states with definite orbital angular momentum by integration over all angles of the relative momentum with the appropriate spherical harmonic

$$|L m_L, S m_S\rangle = \int d^2\Omega \; Y_{L m_L}(\Omega) \; |\Omega, S m_S\rangle, \tag{5.16}$$

where m_L is the azimuthal component of the orbital angular momentum. Using Clebsch-Gordan coefficients, these states can be added appropriately to give a state with total angular momentum

$$|J m_J, LS\rangle = \sum_{m_L, m_S} |L m_L, S m_S\rangle \langle L m_L, S m_S | J m_J\rangle. \tag{5.17}$$

These states are orthonormal:

$$\langle J' m_{J'}, L' S' | J m_J, LS\rangle = \delta_{J' J} \delta_{m_{J'} m_J} \delta_{L' L} \delta_{S' S}, \tag{5.18}$$

ignoring other quantum numbers.

A key quantity in two-particle scattering processes is the so-called S-matrix: $\langle \boldsymbol{p}'_1 \lambda'_1, \boldsymbol{p}'_2 \lambda'_2 | S | \boldsymbol{p}_1 \lambda_1, \boldsymbol{p}_2 \lambda_2\rangle$. The S-matrix is often written in terms of the transition matrix T by $S = 1 + iT$. Uninteresting processes in which the particles fail to interact are described by the first term equal to unity, and the interesting interactions are govern by T. The transition matrix elements are usually evaluated using Feynman rules. Feynman rules in their usual form generally yield answers for the transition matrix in terms of the basis states $|\boldsymbol{p}_1 \lambda_1, \boldsymbol{p}_2 \lambda_2\rangle$. In other words, Feynman rules are

useful for evaluating the matrix elements

$$\langle \boldsymbol{p}_1'\lambda_1', \boldsymbol{p}_2'\lambda_2'|\ iT\ |\boldsymbol{p}_1\lambda_1, \boldsymbol{p}_2\lambda_2\rangle = \langle P'\Omega'\lambda_1'\lambda_2'|\ iT\ |P\Omega\lambda_1\lambda_2\rangle. \tag{5.19}$$

For processes of interest here, total four-momentum is conserved. Using Eq. (5.11) and writing $T = I \otimes T_P$, where I acts on the total four momentum degrees of freedom and T_P acts on the other degrees of freedom, then

$$\begin{aligned} \langle P'\Omega'\lambda_1'\lambda_2'|\ iT\ |P\Omega\lambda_1\lambda_2\rangle &= 4P^0 q^{-1}(2\pi)^6 \langle P'|I|P\rangle\ \langle \Omega'\lambda_1'\lambda_2'|\ iT_P\ |\Omega\lambda_1\lambda_2\rangle, \\ &= 4P^0 q^{-1}(2\pi)^6 \delta^{(4)}(P'-P)\ \langle \Omega'\lambda_1'\lambda_2'|\ iT_P\ |\Omega\lambda_1\lambda_2\rangle, \end{aligned} \tag{5.20}$$

The so-called invariant scattering amplitude $i\mathcal{M}$ is defined by

$$\langle \boldsymbol{p}_1'\lambda_1', \boldsymbol{p}_2'\lambda_2'|\ iT\ |\boldsymbol{p}_1\lambda_1, \boldsymbol{p}_2\lambda_2\rangle = (2\pi)^4 \delta^{(4)}(P'-P)\ \langle \boldsymbol{p}_1'\lambda_1', \boldsymbol{p}_2'\lambda_2'|\ i\mathcal{M}\ |\boldsymbol{p}_1\lambda_1, \boldsymbol{p}_2\lambda_2\rangle. \tag{5.21}$$

Thus, we have

$$\langle \Omega'\lambda_1'\lambda_2'|\ iT_P\ |\Omega\lambda_1\lambda_2\rangle = \frac{q}{16\pi^2 P^0}\ i\mathcal{M}, \tag{5.22}$$

and in terms of LS states, one obtains

$$\langle L'm_{L'}, S'm_{S'}|\ iT_P\ |Lm_L, Sm_S\rangle = \frac{q}{16\pi^2 P^0} \int d^2\Omega'\, d^2\Omega\ Y^*_{L'm_{L'}}(\Omega') Y_{Lm_L}(\Omega)\ i\mathcal{M}. \tag{5.23}$$

$i\mathcal{M}$ is the quantity that is directly computed with Feynman diagrams. Eq. (5.17) can then be used to obtain the matrix elements

$$\begin{aligned} \langle J'm_{J'}'L'S'|\ iT_P\ |Jm_J LS\rangle = &\sum_{m_{L'}m_L m_{S'}m_S} \langle J'm_{J'}|\ L'm_{L'}, S'm_{S'}\rangle \\ &\times \langle L'm_{L'}, S'm_{S'}|\ iT_P\ |Lm_L, Sm_S\rangle\ \langle Lm_L, Sm_S|Jm_J\rangle. \end{aligned} \tag{5.24}$$

The scattering processes we study conserve both total angular momentum J and the projection of total angular momentum, say M_J. Given orthonormal states, then the unitarity of the S-matrix tells us that

$$\langle J'm_{J'}'L'S'a'|\ S\ |Jm_J LSa\rangle = \delta_{J'J}\delta_{m_{J'}m_J}\ s^{(J)}_{L'S'a',\ LSa}(E), \tag{5.25}$$

where a', a denote other defining quantum numbers, such as channel, and $s^{(J)}$ is a

unitary matrix that is independent of m_J due to rotational invariance. If the two particles have zero spin $s_1 = s_2 = 0$ and there is only one channel, then

$$s^{(J)} = s^{(L)} = e^{2i\delta_L(E)}, \tag{5.26}$$

where $\delta_L(E)$ are known as the *scattering phase shifts*. The factor of 2 is conventional to agree with a certain definition when scattering from a central potential.

For systems that are rotationally invariant and invariant under parity, then

$$s^{(J)}_{L'S'a',\ LSa}(E) = 0 \quad \text{for } L - L' \text{ odd}, \qquad \text{(R+P invariance)}. \tag{5.27}$$

For systems invariant under rotations and time invariance,

$$s^{(J)}_{L'S'a',\ LSa}(E) = s^{(J)}_{LSa,\ L'S'a'}(E) \quad \text{(R+T invariance)}. \tag{5.28}$$

5.2 Quantization condition

We define our field theory within an L^3 spatial volume, where L is the extent along each of the three orthogonal Cartesian directions, and we assume the temporal extent is infinite. All fields are required to satisfy certain boundary conditions. The most commonly used boundary conditions are periodic $\psi(\boldsymbol{x} + \boldsymbol{n}L) = \psi(\boldsymbol{x})$, where $\boldsymbol{n}$ is an integer-triplet, but twisted boundary conditions $\psi(\boldsymbol{x} + \boldsymbol{n}L) = e^{i\boldsymbol{\theta}\cdot\boldsymbol{n}}\,\psi(\boldsymbol{x})$, where $0 \le \theta_j \le 2\pi$, are sometimes imposed. We work here in Minkowski space, instead of the usual Euclidean space of lattice QCD simulations, but the final results obtained will not depend on this.

Correlation functions, also known as n-point Green's functions, and physical observables, such as masses and energies, in the theory defined in the L^3 spatial volume differ from their counterparts in the infinite-volume theory. Typically, one finds two broad classes of differences: those that fall off slowly as a power of $1/L$, and those that fall off exponentially quickly as $e^{-L/r}$, where r is the range of the interactions between the hadrons. Here, we assume that L is much larger than r, so that $e^{-L/r}$ corrections can be safely neglected. Thus, we focus our study on the $1/L$ power-law corrections. We restrict attention to energies and momenta below all three- and four-particle thresholds.

We begin by introducing a two-body interpolating operator $\sigma(x)$ which couples to

all open two-body channels. Although this operator need not be local (that is, it can be spatially extended), we must be able to associate a single site x with it. Following Refs. [36] and [32], we define

$$C^L(P) = \int_L d^4x \; e^{i(Ex^0 - \boldsymbol{P}\cdot\boldsymbol{x})} \; \langle 0| \, \sigma(x)\sigma^\dagger(0) \, |0\rangle, \tag{5.29}$$

where $P = (E, \boldsymbol{P})$ is the total four momentum of the two particle system (in the frame where the finite volume condition is applied), and the spatial integration is over the L^3 volume, with the temporal integration of infinite extent. In infinite volume, $C^\infty(P)$ has branch cuts where the two-particle thresholds begin, but the quantization of momenta in finite volume causes these cuts to be replaced by a series of poles. The poles of C^L give the energy spectrum of the finite-volume theory (for those stationary states that couple to $\sigma(x)$), and thus, the condition that C^L diverge is the quantization condition we are after.

We write C^L in terms of the Bethe-Salpeter kernel, as illustrated in Fig. 5.1:

$$C^L(P) = \int_{L;q} \sigma_a(q) \, B_a^L(q) \, \sigma_a^\dagger(q) + \int_{L;q,q'} \sigma_a(q) \, B_a^L(q) \, iK_{ab}(q,q') \, B_b^L(q') \, \sigma_b^\dagger(q') + \cdots . \tag{5.30}$$

The notation here is as follows. Indices a, b, refer to the two-particle channel. $\sigma_a(q)$ and $\sigma_a^\dagger(q')$ are related to the Fourier transforms of $\sigma(x)$ and $\sigma^\dagger(x)$ and describe the coupling of the operators σ and $\sigma^\dagger$ to the two-particle channel a. Their detailed form is not relevant; all we need to know is that they are regular functions of q. The two-particle intermediate states are summed/integrated as is appropriate to finite spatial volume (infinite in time)

$$\int_{L;q} = \frac{1}{L^3} \sum_{\boldsymbol{q}} \int_{-\infty}^{\infty} \frac{dq^0}{2\pi} \, , \qquad \int_{L;q,q'} = \frac{1}{L^6} \sum_{\boldsymbol{q},\boldsymbol{q'}} \int_{-\infty}^{\infty} \frac{dq^0}{2\pi} \frac{dq'^0}{2\pi} \, , \qquad \ldots , \tag{5.31}$$

where the allowed momenta are $\boldsymbol{q} = (2\pi/L)\boldsymbol{n} + \boldsymbol{\theta}/L$ for integer triplet $\boldsymbol{n}$ and θ_j are the twist angles. For periodic boundary conditions, $\theta_j = 0$. Each component n_j is an unbounded sum over integers: $n_j = 0, \pm 1, \pm 2, \ldots$. If channel a consists of a hadron of type a_1 and another hadron of type a_2, then the factor $B_a^L(q)$, which is the product of the two fully-dressed propagators for particles a_1 and a_2, is given by

$$B_a^L(q) = \rho_a \big[z_{a_1}(q) \Delta_{a_1}(q) \big] \big[z_{a_2}(P-q) \Delta_{a_2}(P-q) \big] \, , \tag{5.32}$$

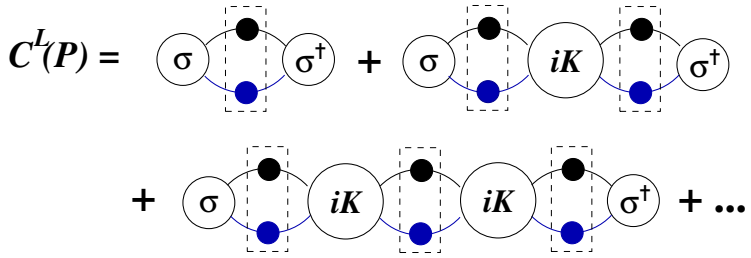

Figure 5.1: The initial series of ladder diagrams which builds up C^L (see Eq. (5.30)). The Bethe-Salpeter kernels iK are connected by fully dressed propagators. The dashed rectangle indicates finite volume momentum sum/integrals. The different colors of the single-particle propagators indicate different types of particles, but choosing the same color allows for identical particles. σ is the two-body interpolating operator that couples to all open two-body channels. Initial states are on the right, final states on the left.

where ρ_a is a possible symmetry factor for channel a and the fully-dressed propagator for a hadron of type α is given by

$$z_\alpha(q)\Delta_\alpha(q) = \int d^4x\, e^{iq\cdot x}\langle\phi_\alpha(x)\phi_\alpha^\dagger(0)\rangle, \quad \text{(no summation over } \alpha\text{)}, \tag{5.33}$$

$$\Delta_\alpha(q) = \frac{i}{q^2 - m_\alpha^2 + i\epsilon}\,. \tag{5.34}$$

Here ϕ_α denotes an interpolating field for a hadron of type α, chosen such that $z_\alpha = 1$ on shell. K is related to the Bethe-Salpeter kernel and is the sum of all amputated $a \leftarrow b$ scattering diagrams which are two-particle-irreducible in the s-channel. Recall that a Feynman diagram is n-particle irreducible if it is connected (all vertices are connected to all other vertices by lines) and cannot be disconnected by cutting n internal lines. Amputated refers to a Feynman diagram in which the external legs have been removed. Note that K can include diagrams with a single internal line, such as a ρ-meson. Allowed diagrams are shown in Fig. 5.2. We restrict our attention to energies E below all three- and four-particle thresholds, so intermediate states with three or more lines can be neglected. Keep in mind that for hadrons of nonzero spin, the residue functions z_α are tensors, and similarly, iK can have tensor indices, so the order of these terms in Eq. (5.30) is important. These tensor indices have been suppressed in Eq. (5.30).

We emphasize two important features of Eq. (5.30). First, it does not rely on

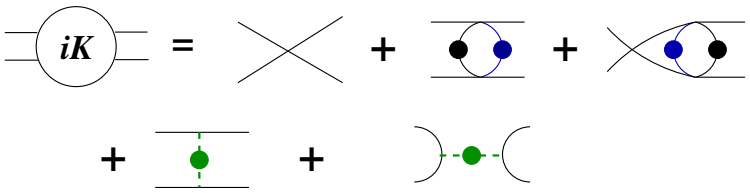

Figure 5.2: Allowed diagrams in the kernel iK which is the sum of all amputated $a \leftarrow b$ scattering diagrams that are two-particle-irreducible in the s-channel. Contact interactions (first diagram), t- and u-channel diagrams (second and third, respectively), and possible meson exchange diagrams (fourth) are included. An annihilation process through a single hadron (fifth diagram) may also be possible. Initial states are on the right, final states on the left.

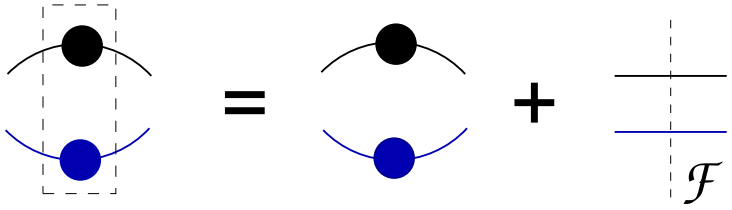

Figure 5.3: The finite-volume momentum sum/integration (indicated by the dashed rectangle) over the two single-particle fully-dressed propagators (shown on the left) equals the infinite-volume integration (first term on right with no dashed rectangle) plus a finite-volume *correction* $\mathcal{F}$ (the second term on the right). This expression essentially defines $\mathcal{F}$.

any choice of interactions between the hadrons. All the quantities that enter can be written in terms of non-perturbatively defined correlation functions. Second, the kernel iK and the propagator dressing, or residue, functions z_α have only exponentially suppressed dependence on the volume[28, 29]. Finite-volume changes loop-integrals to loop-momentum-sums. Later, we will see that the differences between these sums and integrals fall off exponentially fast for nonsingular, finite-ranged functions (see Eq. (5.47)). The residue functions z_α are smooth, and iK is also smooth well away from the t-channel cut. Single-particle propagators typically behave as modified K Bessel functions, which fall off exponentially at large distances. The t- and u-channel loops allowed in iK (see Fig. 5.2) have poles/branch cuts that are well away from the kinematical situation relevant for the s-channel scattering processes being consid-

ered here. Alternatively, consider the t- and u-channel loops in position space as the product of two propagators from, say, the origin to x, integrated over x. Each of the propagators equals the infinite-volume form plus a series of image contributions that are exponentially suppressed (and depend weakly on x). This is true for all x, and thus, the exponential suppression holds also after the integral over x. The fact that the integral runs only over the finite volume rather than infinite volume leads only to exponentially suppressed corrections. In the s-channel loops, we will see that one particular pole becomes relevant and causes non-exponentially small corrections.

Since we assume L is large enough so that such exponential corrections are negligible, we can take iK and the z_α to have their infinite-volume forms. The dominant power-law volume dependence enters through the momentum sums in the two-hadron loops. This is indicated by the dashed boxes in Fig. 5.1.

For the moment, we write $B^L = B + \mathcal{F}$, where $B = B^\infty$ is the value of B^L as $L \to \infty$, and $\mathcal{F}$ is the finite-volume correction. This is shown diagramatically in Fig. 5.3. Applying the substitutions shown in Fig. 5.3 to Fig. 5.1 leads to, using matrix notation (dropping all indices and summations)

$$C^L(P) = \sigma B^L \sum_{n=0}^{\infty} \left[(iK)B^L\right]^n \sigma^\dagger = \sigma(B+\mathcal{F}) \sum_{n=0}^{\infty} \left[(iK)(B+\mathcal{F})\right]^n \sigma^\dagger. \tag{5.35}$$

Now we expand this out and collect terms that have the same number of $\mathcal{F}$ insertions. Define

$$A = \sigma \sum_{n=0}^{\infty} (BiK)^n, \qquad A' = \sum_{n=0}^{\infty} (iKB)^n \, \sigma^\dagger, \qquad i\mathcal{M} = iK \sum_{n=0}^{\infty} (BiK)^n, \tag{5.36}$$

as shown in Fig. 5.4. Defining $C_{\text{sub}}(P) = C^L(P) - C^\infty(P)$, we obtain

$$C_{\text{sub}}(P) = A\mathcal{F} \sum_{n=0}^{\infty} (i\mathcal{M}\mathcal{F})^n \, A', \tag{5.37}$$

as depicted in Fig. 5.4. Notice that $i\mathcal{M}$ is the infinite-volume scattering amplitude. For a matrix X, it is easy to see that $(1-X)\sum_{n=0}^{\infty} X^n = 1$, which means that

$$\sum_{n=0}^{\infty} X^n = (1-X)^{-1}. \tag{5.38}$$

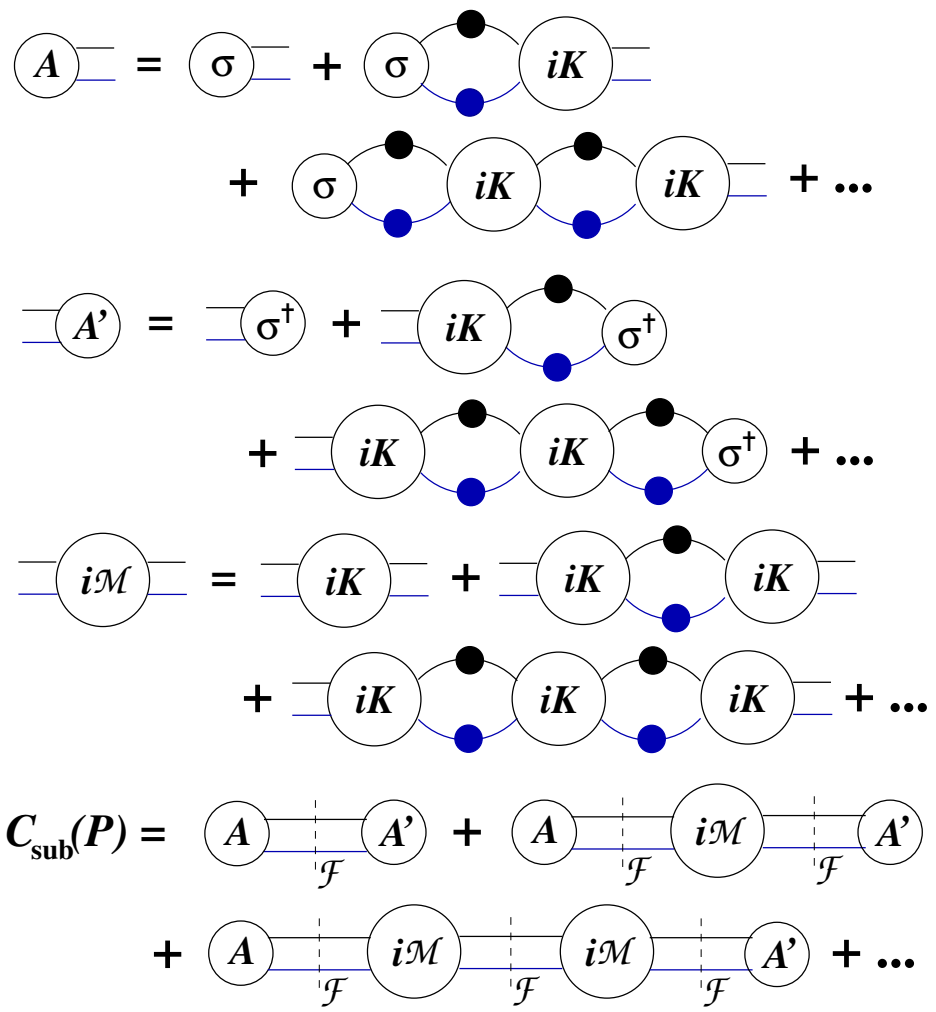

Figure 5.4: Expressing $C_{\rm sub}(P) = C^L(P) - C^\infty(P)$ in terms of $A, A', i\mathcal{M}$, defined above, and the $\mathcal{F}$ insertions.

We can use this result to get

$$C_{\rm sub}(P) = A\ \mathcal{F}(1 - i\mathcal{M}\mathcal{F})^{-1}\ A'. \tag{5.39}$$

We will see that $\mathcal{F}$ has poles at all energies corresponding to two free particles in the moving frame, but if $i\mathcal{M} \neq 0$, which should be true in the presence of interactions, the quantity $(1 - i\mathcal{M}\mathcal{F})^{-1}$ has zeros at all of these free energies. In other words, the free-energy poles in $\mathcal{F}$ in the numerator are cancelled by the same poles in $(1 - i\mathcal{M}\mathcal{F})$ in the denominator.

We will later find that $\det \mathcal{F} \neq 0$, so we can write $\mathcal{F} = (\mathcal{F}^{-1})^{-1}$ and use $X^{-1}Y^{-1} = (YX)^{-1}$ to obtain

$$C_{\text{sub}}(P) = A\ (\mathcal{F}^{-1} - i\mathcal{M})^{-1}\ A'. \tag{5.40}$$

The infinite-volume correlator $C^{\infty}(P)$ does not contain the poles that we are seeking. Since $C^{L}(P)$ does contain the poles we want, then $C_{\text{sub}}(P)$ must contain the poles we are after, as well as the cuts which must cancel those in $C^{\infty}(P)$. The poles do not come from the A, A' factors. The A, A' factors involve nonsingular terms involving the $\sigma, \sigma^{\dagger}$, and a geometric series of contributions with insertions of iK and infinite-volume loop momentum. These infinite-volume factors may produce branch cuts, but not the finite-volume poles we seek. Given the above expression, the poles can only occur whenever one encounters a zero eigenvalue of the matrix: $\mathcal{F}^{-1} - i\mathcal{M}$. Thus, the interacting poles of $C_{\text{sub}}(P)$ occur whenever one encounters

$$\det(\mathcal{F}^{-1} - i\mathcal{M}) = 0. \tag{5.41}$$

To put this into a more convenient form that does not require taking the inverse of a matrix, we multiply by $\det \mathcal{F} \neq 0$. Thus, an equivalent statement of the above condition is $\det \mathcal{F} \det(\mathcal{F}^{-1} - i\mathcal{M}) = 0$, which gives us

$$\det(1 - i\mathcal{F}\mathcal{M}) = 0. \tag{5.42}$$

This is the crucial *quantization condition* that relates the finite-volume two-particle energies to the infinite-volume scattering amplitudes $i\mathcal{M}$. Expressing the infinite-volume scattering amplitudes in terms of the scattering phase shifts allows us to determine these phase shifts from our finite-volume energies.

5.3 Finite-volume effects in the loop summation

To express the above quantization condition in a more useful form, we need to examine the quantity $\mathcal{F}$ in more detail. Using Eqs. (5.30), (5.32), (5.33), and (5.34), it is not difficult to see that $\mathcal{F}$ will involve an integral/summation of the form

$$I \equiv \frac{1}{L^3} \sum_{\boldsymbol{k}} \int \frac{dk_0}{2\pi} \frac{f(k_0, \boldsymbol{k})}{(k^2 - m_1^2 + i\varepsilon)((P-k)^2 - m_2^2 + i\varepsilon)}, \tag{5.43}$$

where $k = (k_0, \boldsymbol{k})$ and $P = (E, \boldsymbol{P})$ are four-vectors and

$$f(k^0, \boldsymbol{k}) = g_{K_L}(k)\ (i)^2\ \rho_a\ z_{a_1}(k)\ z_{a_2}(P-k)\ g_{K_R}(k), \tag{5.44}$$

with the factors g_{K_R} and g_{K_L} coming from the iK (or $\sigma, \sigma^\dagger$) factors on the right and left, respectively, of B^L. Since $E, \boldsymbol{P}$ are fixed, f can be expressed as a function of k alone. The only properties of f that we need are that is has no singularities for real $\boldsymbol{k}$, and its ultraviolet behavior is such as to render the integral and sum convergent.

5.3.1 Poisson summation

The well-known Poisson summation formula leads to

$$\frac{1}{L^3}\sum_{\boldsymbol{p}}\ \widetilde{g}(\boldsymbol{p}) = \int \frac{d^3k}{(2\pi)^3}\ \widetilde{g}(\boldsymbol{k}) + \sum_{\boldsymbol{l}\neq\boldsymbol{0}} \int \frac{d^3k}{(2\pi)^3}\ e^{iL\boldsymbol{k}\cdot\boldsymbol{l}}\widetilde{g}(\boldsymbol{k}), \tag{5.45}$$

where the summation on the left-hand side is over $\boldsymbol{p} = (2\pi/L)\boldsymbol{n}$ for integer-triplet $\boldsymbol{n}$, and on the right-hand side, $\boldsymbol{l}$ is an integer triplet that excludes $\boldsymbol{l} = (0,0,0)$. From now on, we assume periodic boundary conditions. Using the inverse Fourier transform, we obtain

$$\frac{1}{L^3}\sum_{\boldsymbol{p}}\ \widetilde{g}(\boldsymbol{p}) = \int \frac{d^3k}{(2\pi)^3}\ \widetilde{g}(\boldsymbol{k}) + \sum_{\boldsymbol{l}\neq\boldsymbol{0}} g(L\boldsymbol{l}). \tag{5.46}$$

Eq. (5.46) tells us that for functions $\widetilde{g}(\boldsymbol{k})$ whose inverse Fourier transforms in coordinate space $g(\boldsymbol{r})$ are nonsingular and either contained within a finite spatial region or decrease exponentially as $|\boldsymbol{r}| \to \infty$, the terms with $\boldsymbol{l} \neq 0$ on the right-hand side of Eq. (5.46) decrease at least exponentially as the box size L becomes large, so

$$\frac{1}{L^3}\sum_{\boldsymbol{p}}\ g_c(\boldsymbol{p}) = \int \frac{d^3k}{(2\pi)^3}\ g_c(\boldsymbol{k}) + O(e^{-mL}), \qquad (g_c(\boldsymbol{p}) \text{ spatially contained and regular}), \tag{5.47}$$

where $m \sim 1/r$ is some mass scale, such as the pion mass, with r being the typical range of interactions (assumed smaller than L). The key point here is that whenever we carry out a summation of a finite-ranged integrand without singularities, we can take the large L limit by replacing the momentum summation with a momentum integration, ignoring exponentially suppressed terms.

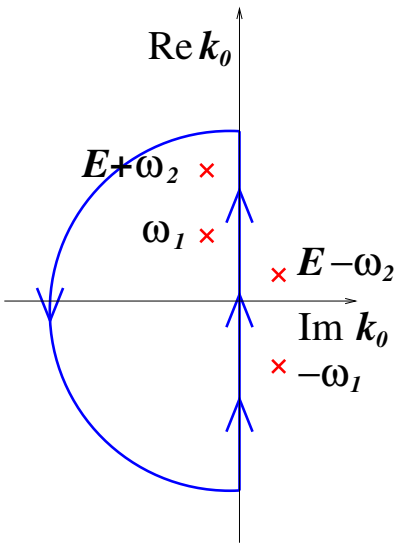

Figure 5.5: Poles in the complex k_0 plane for the integrand in Eq. (5.43). The contour used to do the k_0 integration is shown.

5.3.2 Isolating the finite volume effects

To isolate the finite-volume effects, we now proceed as described in Ref. [32]. First, we integrate over k_0. Define

$$\omega_1 = \sqrt{\boldsymbol{k}^2 + m_1^2}, \qquad \omega_2 = \sqrt{(\boldsymbol{P} - \boldsymbol{k})^2 + m_2^2}, \tag{5.48}$$

then the integrand in Eq. (5.43) has poles at

$$k_0 = \omega_1 - i\varepsilon, \quad k_0 = -\omega_1 + i\varepsilon, \quad k_0 = E + \omega_2 - i\varepsilon, \quad k_0 = E - \omega_2 + i\varepsilon, \tag{5.49}$$

where $\varepsilon > 0$ is any positive real infinitesimal quantity. Since E is the total energy of the system, we expect that E is greater than ω_2, so the poles in the complex k_0 plane look as shown in Fig. 5.5. We close the contour in the left half-plane since temporal evolution is expected to have the behavior e^{-iEt}, then the contribution from the half circle goes to zero as the radius of the contour becomes large. Thus, we obtain

$$I = \frac{-i}{L^3} \sum_{\boldsymbol{k}} \left\{ \frac{f(\omega_1, \boldsymbol{k})}{2\omega_1((E-\omega_1)^2 - \omega_2^2)} + \frac{f(E+\omega_2, \boldsymbol{k})}{2\omega_2((E+\omega_2)^2 - \omega_1^2)} \right\}, \tag{5.50}$$

from residue theory. We now drop the $i\varepsilon$ in the remaining summation, which assumes that the poles do not coincide with any of the allowed values of $\boldsymbol{k} = (2\pi/L)\boldsymbol{n}$, assuming periodic boundary conditions. Since the energies of interest are shifted by interactions away from those of two free particles, this should hold in general in finite volume. Of course, in infinite volume, an integral must be performed and the factors of $i\varepsilon$ must be retained.

Consider the second term above. Write the total energy as $E = \omega_1 + \omega_2 + \Delta$. For free particles, $\Delta = 0$. Note that Δ could be positive or negative depending on the interactions between the two particles. Substituting this expression for E into the denominator, we can then solve to find what values of Δ cause the denominator to become zero. We find that zeros occur when $\Delta = -2\omega_2$ and $\Delta = -2(\omega_1 + \omega_2)$. These are large negative values, indicating very strong binding. We work under the scattering assumption that the two-particle finite-volume energies do not deviate very much from their free values. Thus, the second term contains no singularities, so the summation will only have exponentially small corrections from the large-L limit. Since we are neglecting such terms, we can approximate the second term by its large-L value. The first term is a different matter, since it does contain a singularity and must be treated carefully. We, thus, write

$$I = I_1 + I_2, \tag{5.51}$$

where

$$I_1 = \frac{-i}{L^3} \sum_{\boldsymbol{k}} \frac{f(\omega_1, \boldsymbol{k})}{2\omega_1((E-\omega_1)^2 - \omega_2^2)}, \tag{5.52}$$

$$I_2 = -i \int \frac{d^3k}{(2\pi)^3} \frac{f(E+\omega_2, \boldsymbol{k})}{2\omega_2((E+\omega_2)^2 - \omega_1^2)}. \tag{5.53}$$

5.3.3 Center-of-mass variables

To continue with I_1, we now work in the center-of-mass (cm) frame which will facilitate an expansion in terms of partial waves. In the lab frame (in which the boundary conditions are imposed), the total four-momentum is $(E, \boldsymbol{P})$. We now boost to the cm frame in which the total four-momentum is $(E^*, \boldsymbol{0})$. Recall how energy and momentum

transform under a Lorentz boost (remember we use $c = 1$):

$$\boldsymbol{p}'_{\parallel} = \gamma(\boldsymbol{p}_{\parallel} - \boldsymbol{\beta}E), \qquad \boldsymbol{p}'_{\perp} = \boldsymbol{p}_{\perp}, \qquad E' = \gamma(E - \boldsymbol{\beta}\cdot\boldsymbol{p}_{\parallel}), \tag{5.54}$$

where $\gamma = (1-\boldsymbol{\beta}^2)^{-1/2}$ and $\boldsymbol{\beta}$ is the velocity of frame S' as seen in frame S. As viewed from the lab frame (unprimed), the cm frame (primed) moves with momentum $\boldsymbol{P}$. So with $\boldsymbol{p}_{\perp} = 0$ and $\boldsymbol{p}_{\parallel} = \boldsymbol{P}$, we want

$$\boldsymbol{p}'_{\parallel} = 0 = \gamma(\boldsymbol{P} - \boldsymbol{\beta}E). \tag{5.55}$$

This means $\boldsymbol{\beta} = \boldsymbol{P}/E$ and $\gamma = (1 - \boldsymbol{P}^2/E^2)^{-1/2}$. Then

$$E' = E^* = \gamma(E - \beta P) = \frac{(E - \boldsymbol{P}^2/E)}{\sqrt{1 - \boldsymbol{P}^2/E^2}} = \sqrt{E^2 - \boldsymbol{P}^2}. \tag{5.56}$$

Hence, for a known allowed total momentum $\boldsymbol{P} = (2\pi/L)\boldsymbol{d}$, where $\boldsymbol{d}$ is an integer triplet, we can determine the finite-volume energy E in our lattice calculations, then obtain E^* from the above formula. From the above expression for γ, we see that $\gamma = E/E^*$, and keep in mind that $\beta = |\boldsymbol{P}|/E$.

In what follows, the subscripts $\parallel$ and $\perp$ refer to the direction of $\boldsymbol{P}$. Again, $\boldsymbol{k}$ is the momentum of the particle of mass m_1 in the lab frame with $\omega_1 = \sqrt{\boldsymbol{k}^2 + m_1^2}$, then in the cm frame, denote its momentum by $\boldsymbol{k}^*$ and define $\omega_1^* = \sqrt{\boldsymbol{k}^{*2} + m_1^2}$, then

$$k^*_{\parallel} = \gamma(k_{\parallel} - \beta\omega_1), \qquad \boldsymbol{k}^*_{\perp} = \boldsymbol{k}_{\perp}, \qquad \omega_1^* = \gamma(\omega_1 - \beta k_{\parallel}). \tag{5.57}$$

The momentum of the second particle of mass m_2 in the lab frame is $\boldsymbol{P} - \boldsymbol{k}$ and remember that $\omega_2 = \sqrt{(\boldsymbol{P} - \boldsymbol{k})^2 + m_2^2}$. Then in the cm frame,

$$\omega_2^* = \gamma(\omega_2 - \beta(P - k_{\parallel})). \tag{5.58}$$

After some tedious algebraic manipulations, we find the denominator of 5.52 is

$$(E - \omega_1)^2 - \omega_2^2 = E^*(E^* - 2\omega_1^*) + m_1^2 - m_2^2 = E^*\left(E^* - 2\omega_1^* + \frac{(m_1^2 - m_2^2)}{E^*}\right). \tag{5.59}$$

With this, we can write I_1 as

$$I_1 = \frac{-i}{L^3}\frac{1}{E^*}\sum_{\boldsymbol{k}}\frac{1}{(2\omega_1)}\frac{f^*(\boldsymbol{k}^*)}{[E^* - 2\omega_1^* + (m_1^2 - m_2^2)/E^*]}, \tag{5.60}$$

where f^* is the function f rewritten in terms of the cm variables. Since ω_1^* is a dependent variable, we write f^* as a function of $\boldsymbol{k}^*$ alone.

We now introduce $\boldsymbol{q}^{*2}$, defined by

$$\sqrt{\boldsymbol{q}^{*2} + m_1^2} + \sqrt{\boldsymbol{q}^{*2} + m_2^2} = E^*. \tag{5.61}$$

Note that $\boldsymbol{q}^{*2}$ is the square of the three-momentum of each particle in the cm frame for a system of two *free* particles of masses m_1 and m_2 having total energy E^* in the cm frame. Solving for $\boldsymbol{q}^{*2}$ gives

$$\boldsymbol{q}^{*2} = \frac{1}{4}E^{*2} - \frac{1}{2}(m_1^2 + m_2^2) + \frac{(m_1^2 - m_2^2)^2}{4E^{*2}}. \tag{5.62}$$

This quantity will play a key role in the formulas developed below.

Returning our attention to I_1, first note that

$$\begin{aligned}
& [E^* + (m_1^2 - m_2^2)/E^* - 2\omega_1^*][E^* + (m_1^2 - m_2^2)/E^* + 2\omega_1^*] \\
= \;& [E^* + (m_1^2 - m_2^2)/E^*]^2 - 4\omega_1^{*2} \\
= \;& E^{*2} + 2(m_1^2 - m_2^2) + (m_1^2 - m_2^2)^2/E^{*2} - 4\boldsymbol{k}^{*2} - 4m_1^2 \\
= \;& E^{*2} - 2(m_1^2 + m_2^2) + (m_1^2 - m_2^2)^2/E^{*2} - 4\boldsymbol{k}^{*2} \\
= \;& 4(\boldsymbol{q}^{*2} - \boldsymbol{k}^{*2}).
\end{aligned} \tag{5.63}$$

With this, we can now massage I_1 into the form

$$I_1 = \frac{-i}{L^3}\frac{1}{(2E^*)}\sum_{\boldsymbol{k}}\frac{\omega_1^*}{\omega_1}\,\frac{f^*(\boldsymbol{k}^*)}{(\boldsymbol{q}^{*2} - \boldsymbol{k}^{*2})}\left(\frac{E^* + (m_1^2 - m_2^2)/E^* + 2\omega_1^*}{4\omega_1^*}\right). \tag{5.64}$$

A factor of $1/\omega_1$ has been deliberately not written in terms of cm variables in order to simplify a particular term later.

5.3.4 Expansion in partial waves

We continue along the lines described in Ref. [32]. Consider a momentum summation of the form

$$S(\boldsymbol{q}^{*2}) \equiv \frac{1}{L^3} \sum_{\boldsymbol{k}} \frac{\omega_1^*}{\omega_1} \frac{h_r(\boldsymbol{k}^*)}{(\boldsymbol{q}^{*2} - \boldsymbol{k}^{*2})}, \tag{5.65}$$

where the summation is over $\boldsymbol{k} = (2\pi/L)\boldsymbol{n}$, with $\boldsymbol{n}$ being a vector of integers, and the quantities $\boldsymbol{q}^{*2}, \boldsymbol{k}^*, \omega_1, \omega_1^*$ are cm factors as previously described. $h_r(\boldsymbol{k}^*)$ is a spatially contained, regular function. A summation of this form occurs in I_1.

If it were not for the $(\boldsymbol{q}^{*2} - \boldsymbol{k}^{*2})$ in the denominator, we could replace the summation with an integral and neglect the $O(e^{-mL})$ error made in doing this. Since we are trying to find a relationship between finite-volume energies and scattering phase shifts, and since phase shifts are generally expressed in terms of partial waves, we proceed by writing $\boldsymbol{k}^*$ in terms of spherical polar coordinates (k^*, θ^*, ϕ^*) and expanding h_r in terms of spherical harmonics Y_{lm}:

$$h_r(\boldsymbol{k}^*) = \sqrt{4\pi} \sum_{l=0}^{\infty} \sum_{m=-l}^{l} h_{lm}(k^*)\ k^{*l}\ Y_{lm}(\theta^*, \phi^*). \tag{5.66}$$

The factor $\sqrt{4\pi} = 1/Y_{00}$ is introduced to simplify subsequent expressions for $l = 0$. We will comment on the purpose of the k^{*l} factors below. From the above expression, one sees that

$$h_{lm}(k^*) = \frac{1}{\sqrt{4\pi}\ k^{*l}} \int d^2\Omega^* h_r(\boldsymbol{k}^*)\ Y_{lm}^*(\theta^*, \phi^*). \tag{5.67}$$

We now have

$$S(\boldsymbol{q}^{*2}) = \sum_{lm} S_{lm}(\boldsymbol{q}^{*2}), \qquad S_{lm}(\boldsymbol{q}^{*2}) = \frac{\sqrt{4\pi}}{L^3} \sum_{\boldsymbol{k}} \frac{\omega_1^*}{\omega_1} \frac{h_{lm}(k^*)}{(\boldsymbol{q}^{*2} - k^{*2})}\ k^{*l}\ Y_{lm}(\theta^*, \phi^*). \tag{5.68}$$

We can now focus on each $S_{lm}(\boldsymbol{q}^{*2})$ individually.

To isolate the effect of the pole at $k^* = q^* = \sqrt{\boldsymbol{q}^{*2}}$ (remember that k^* must be positive in spherical polar coordinates so the $-q^*$ pole cannot occur), we subtract a term chosen to cancel the pole, then add it back in:

$$S_{lm}(\boldsymbol{q}^{*2}) \;=\; \frac{\sqrt{4\pi}}{L^3} \sum_{\boldsymbol{k}} \frac{\omega_1^*}{\omega_1} \frac{[h_{lm}(k^*) - h_{lm}(q^*)e^{\lambda(q^{*2} - k^{*2})}]}{(q^* - k^*)(q^* + k^*)}\ k^{*l}\ Y_{lm}(\theta^*, \phi^*)$$

$$+\frac{\sqrt{4\pi}}{L^3}\sum_{\boldsymbol{k}}\frac{\omega_1^*}{\omega_1}\;\frac{h_{lm}(q^*)e^{\lambda(q^{*2}-k^{*2})}}{(q^{*2}-k^{*2})}\;k^{*l}\;Y_{lm}(\theta^*,\phi^*). \tag{5.69}$$

A Taylor expansion of $h_{lm}(k^*) = h_{lm}(q^*) + (k^*-q^*)h'_{lm}(q^*) + \ldots$ shows that the pole has been removed in the first term above. The exponential factors $e^{\lambda(q^{*2}-k^{*2})}$ with $\lambda > 0$ are included so that the subtraction does not introduce ultraviolet divergences.

Notice that a subtraction of the form $h_r(\boldsymbol{k}^*) - h_r(\boldsymbol{q}^*)$, done before the expansion in spherical harmonics, would not exactly cancel the pole. Also, one can now see that the k^{*l} factors are needed so the subtraction does not introduce a singularity at $k^* = 0$. The spherical harmonics for $l > 0$ are ill-defined at the origin, because the polar and azimuthal angles are ill-defined at the origin. Another way of saying this is that the result at the origin depends on the direction of approach. Thus, derivatives of some order are divergent, which means that if the harmonics are part of a summand that is otherwise smooth, one cannot replace the sum with an integral and make only exponentially small errors. The k^{*l} factors are exactly what are needed to avoid this problem: $k^{*l}Y_{lm}(\widehat{\boldsymbol{k}^*})$ are polynomials in the components of $\boldsymbol{k}^*$, and thus, infinitely differentiable. Note that the end results will *not* depend on the parameter λ. Any λ dependence will enter in the exponentially small terms which we ignore.

Using Eq. (5.47), we obtain

$$\begin{aligned} S_{lm}(\boldsymbol{q}^{*2}) &= \sqrt{4\pi}\;\mathcal{P}\int\frac{d^3k}{(2\pi)^3}\frac{\omega_1^*}{\omega_1}\;\frac{[h_{lm}(k^*)-h_{lm}(q^*)e^{\lambda(q^{*2}-k^{*2})}]}{(q^{*2}-k^{*2})}\;k^{*l}\;Y_{lm}(\theta^*,\phi^*) \\ &\quad +h_{lm}(q^*)\;\frac{\sqrt{4\pi}}{L^3}\sum_{\boldsymbol{k}}\frac{\omega_1^*}{\omega_1}\;\frac{e^{\lambda(q^{*2}-k^{*2})}}{(q^{*2}-k^{*2})}\;k^{*l}\;Y_{lm}(\theta^*,\phi^*), \end{aligned} \tag{5.70}$$

where $\mathcal{P}$ denotes principal value. The integrand in the first term is regular, so the principal value is superfluous at this point. In a moment, we will split up this integral, so we will need the principal value for the separate pieces. Using Eq. (5.57), we see that

$$\frac{dk_\parallel^*}{dk_\parallel} = \frac{d}{dk_\parallel}\gamma\left(k_\parallel - \beta\sqrt{k_\parallel^2+\boldsymbol{k}_\perp^2+m_1^2}\right) = \gamma - \beta\gamma\frac{k_\parallel}{\omega_1} = \gamma(\omega_1-\beta k_\parallel)/\omega_1 = \frac{\omega_1^*}{\omega_1}. \tag{5.71}$$

Since $\boldsymbol{k}_\perp^* = \boldsymbol{k}_\perp$, then

$$d^3k = \frac{\omega_1}{\omega_1^*}\;d^3k^* \tag{5.72}$$

and we obtain

$$S_{lm}(\boldsymbol{q}^{*2}) = \sqrt{4\pi}\ \mathcal{P}\int \frac{d^3k^*}{(2\pi)^3}\frac{[h_{lm}(k^*)-h_{lm}(q^*)e^{\lambda(q^{*2}-k^{*2})}]}{(q^{*2}-k^{*2})}\ k^{*l}\ Y_{lm}(\theta^*,\phi^*)$$
$$+h_{lm}(q^*)\ \frac{\sqrt{4\pi}}{L^3}\sum_{\boldsymbol{k}}\frac{\omega_1^*}{\omega_1}\ \frac{e^{\lambda(q^{*2}-k^{*2})}}{(q^{*2}-k^{*2})}\ k^{*l}\ Y_{lm}(\theta^*,\phi^*), \tag{5.73}$$

which now explains why the factor of ω_1^*/ω_1 was retained in Eq. (5.64). Having made this change of variables, the angular integrations can be done in the first term. All terms vanish except for the $l=0$ term:

$$S_{lm}(\boldsymbol{q}^{*2}) = \delta_{l0}\ \mathcal{P}\int \frac{d^3k^*}{(2\pi)^3}\frac{[h_{lm}(k^*)-h_{lm}(q^*)e^{\lambda(q^{*2}-k^{*2})}]}{(q^{*2}-k^{*2})}\ k^{*l}$$
$$+h_{lm}(q^*)\ \frac{\sqrt{4\pi}}{L^3}\sum_{\boldsymbol{k}}\frac{\omega_1^*}{\omega_1}\ \frac{e^{\lambda(q^{*2}-k^{*2})}}{(q^{*2}-k^{*2})}\ k^{*l}\ Y_{lm}(\theta^*,\phi^*). \tag{5.74}$$

Rewrite this as

$$S_{lm}(\boldsymbol{q}^{*2}) = \delta_{l0}\ \mathcal{P}\int \frac{d^3k^*}{(2\pi)^3}\frac{h_{lm}(k^*)}{(q^{*2}-k^{*2})}\ k^{*l} - \delta_{l0}\ h_{lm}(q^*)\ \mathcal{P}\int \frac{d^3k^*}{(2\pi)^3}\frac{e^{\lambda(q^{*2}-k^{*2})}}{(q^{*2}-k^{*2})}\ k^{*l}$$
$$+h_{lm}(q^*)\ \frac{\sqrt{4\pi}}{L^3}\sum_{\boldsymbol{k}}\frac{\omega_1^*}{\omega_1}\ \frac{e^{\lambda(q^{*2}-k^{*2})}}{(q^{*2}-k^{*2})}\ k^{*l}\ Y_{lm}(\theta^*,\phi^*). \tag{5.75}$$

This leads us to define

$$c_{lm}^{\boldsymbol{P}}(\boldsymbol{q}^{*2}) \equiv \frac{\sqrt{4\pi}}{L^3}\sum_{\boldsymbol{k}}\frac{\omega_1^*}{\omega_1}\ \frac{e^{\lambda(q^{*2}-k^{*2})}}{(q^{*2}-k^{*2})}\ k^{*l}\ Y_{lm}(\theta^*,\phi^*) - \delta_{l0}\ \mathcal{P}\int \frac{d^3k^*}{(2\pi)^3}\frac{e^{\lambda(q^{*2}-k^{*2})}}{(q^{*2}-k^{*2})}. \tag{5.76}$$

These coefficients will be very important in what follows. Returning to the original $S(\boldsymbol{q}^{*2})$, we now have

$$S(\boldsymbol{q}^{*2}) = \sum_{lm}\delta_{l0}\ \mathcal{P}\int \frac{d^3k^*}{(2\pi)^3}\frac{h_{lm}(k^*)}{(q^{*2}-k^{*2})}\ k^{*l} + \sum_{lm}h_{lm}(q^*)\ c_{lm}^{\boldsymbol{P}}(\boldsymbol{q}^{*2}). \tag{5.77}$$

Since the angular integration over Y_{lm} vanishes unless $l=0$, we can rewrite the first term

$$\sqrt{4\pi}\sum_{lm}\ \mathcal{P}\int \frac{d^3k^*}{(2\pi)^3}\frac{h_{lm}(k^*)Y_{lm}(\theta^*,\phi^*)}{(q^{*2}-k^{*2})}\ k^{*l}. \tag{5.78}$$

Now use Eq. (5.66) to obtain

$$S(\boldsymbol{q}^{*2}) = \mathcal{P}\int \frac{d^3k^*}{(2\pi)^3}\frac{h_r(\boldsymbol{k}^*)}{(q^{*2}-k^{*2})} + \sum_{lm} h_{lm}(q^*)\; c_{lm}^{\boldsymbol{P}}(\boldsymbol{q}^{*2}). \tag{5.79}$$

After a few more manipulations, we eventually find that we can write

$$I^{FV} = \int d^2\Omega\; \mathcal{I}^{FV}(\Omega), \tag{5.80}$$

where

$$\mathcal{I}^{FV}(\Omega) = \frac{q^* f(\boldsymbol{q}^*)}{32\pi^2 E^*}\left(1 - i(4\pi)^{3/2}\sum_{lm}\frac{Y_{lm}^*(\Omega)\; c_{lm}^{\boldsymbol{P}}(\boldsymbol{q}^{*2})}{q^{*(l+1)}}\right). \tag{5.81}$$

The quantity I^{FV} is the finite-volume correction related to the $\mathcal{F}$ factors we previously introduced. The coefficients $c_{lm}^{\boldsymbol{P}}(\boldsymbol{q}^{*2})$ are independent of the vertex factors and are completely defined by Eq. (5.76). We will look at these coefficients in more detail later.

5.4 Quantization condition revisited

A key point about the finite-volume correction is that the numerator function f^* is only needed at $\boldsymbol{k}^{*2} = \boldsymbol{q}^{*2}$ so that both particles are on mass shell. This results in an important simplification. Each renormalized fully-dressed single-particle propagator has the form

$$\frac{iz(p)}{(p^2 - m^2 + i\varepsilon)}, \tag{5.82}$$

where $z(p)$ is a matrix of functions of p depending on the spin of the particle. For example, the running mass can be accounted for in these functions. Regardless of how complicated the $z(p)$ functions are off-shell, the $z(p)$ for each renormalized propagator is required to be the identity matrix when $p^2 = m^2$ on the mass shell. Using Eq. (5.44), we then have

$$\mathcal{I}^{FV}(\Omega) = \frac{-\rho_a q^*}{32\pi^2 E^*}\; g_{K_L}(\boldsymbol{q}^*)\, g_{K_R}(\boldsymbol{q}^*)\left(1 - i(4\pi)^{3/2}\sum_{lm}\frac{Y_{lm}^*(\Omega)\; c_{lm}^{\boldsymbol{P}}(\boldsymbol{q}^{*2})}{q^{*(l+1)}}\right). \tag{5.83}$$

We now peel off the g_{K_L} and g_{K_L} factors that are not associated with $\mathcal{F}$ and restore the spin indices. Clearly, $\mathcal{F}$ is diagonal in channel space, and $\mathcal{F}$ is diagonal in the

particle helicities, or alternatively, in the single-particle spin projections onto the z-axis m_{S_1}, m_{S_2}. Given that $z(p)$ becomes the identity matrix on shell, this is equivalent to diagonality in total S and m_S. Hence, we can write

$$\langle \Omega' S' m_{S'} a' | \mathcal{F} | \Omega S m_S a \rangle = \delta_{a'a} \delta_{S'S} \delta_{m_{S'} m_S} \delta(\Omega' - \Omega) \mathcal{F}_P(\Omega), \tag{5.84}$$

where

$$\mathcal{F}_P(\Omega) = -\frac{\rho_a q^*}{32\pi^2 E^*} \left(1 - i(4\pi)^{3/2} \sum_{lm} \frac{Y^*_{lm}(\Omega)\ c^{\boldsymbol{P}}_{lm}(\boldsymbol{q}^{*2})}{q^{*(l+1)}} \right). \tag{5.85}$$

Rewrite Eq. (5.37) in the same form as the starting Eq. (5.30) to obtain

$$C_{\rm sub}(P) = \int \frac{d^4k}{(2\pi)^4} A(k) \mathcal{F}(k) A'(k) + \int \frac{d^4k}{(2\pi)^4} \frac{d^4k'}{(2\pi)^4}\ A(k) \mathcal{F}(k) i\mathcal{M}(k,k') \mathcal{F}(k') A'(k') + \ldots,$$

suppressing all spin indices. The function $\mathcal{F}(k)$ is defined so that, for example, in the first term, the integration gives

$$\int \frac{d^4k}{(2\pi)^4} A(k) \mathcal{F}(k) A'(k) = \int d^2\Omega\ A(\hat{k}) \mathcal{F}_P(\Omega) A'(\hat{k}), \tag{5.86}$$

remembering Eq. (5.84) with spin indices suppressed. Similarly, in the second term above, we will have

$$\begin{aligned} \int \frac{d^4k}{(2\pi)^4} \frac{d^4k'}{(2\pi)^4}\ A(k) \mathcal{F}(k) i\mathcal{M}(k,k') \mathcal{F}(k')\ A'(k') = \int d^2\Omega d^2\Omega' A(\hat{k}) \mathcal{F}_P(\Omega) \\ \times i\mathcal{M}(\hat{k},\hat{k}') \mathcal{F}_P(\Omega') A'(\hat{k}'). \end{aligned} \tag{5.87}$$

From Eq. (5.37) and pondering how Feynman rules are applied, one concludes that the $i\mathcal{M}(k,k')$ factors must correspond to the quantity $\langle P'\Omega' | iT_P | P\Omega \rangle$, where the normalization of these states is given in Eq. (5.10). We want to write this in terms of angular states that can be integrated to obtain orthonormalized Lm_L states, so we use Eq. (5.22) and write

$$i\mathcal{M}(k,k') = \frac{16\pi^2 E^*}{q^*} \langle \Omega | i\mathcal{M} | \Omega' \rangle, \tag{5.88}$$

with normalization $\langle\Omega|\Omega'\rangle = \delta^{(2)}(\Omega' - \Omega)$. Now use Eq. (5.16) to obtain

$$\langle Lm_L, Sm_S|i\mathcal{M}|L'm_{L'}, S'm_{S'}\rangle = \int d^2\Omega d^2\Omega'\; Y^*_{Lm_L}(\Omega)Y_{L'm_{L'}}(\Omega')\langle\Omega Sm_S|i\mathcal{M}|\Omega' S'm_{S'}\rangle.$$

Since we will always deal with the product $i\mathcal{F}\mathcal{M}$, we can absorb the factor in Eq. (5.88) into the definition of a rescaled $\mathcal{F}$ matrix, as well as absorb a minus sign:

$$F^{(\boldsymbol{P})}(\Omega) = -\frac{16\pi^2 E^*}{q^*}\mathcal{F}_P(\Omega) = \frac{\rho_a}{2}\left(1 - i(4\pi)^{3/2}\sum_{lm}\frac{Y^*_{lm}(\Omega)\; c^{\boldsymbol{P}}_{lm}(\boldsymbol{q}^{*2})}{q^{*(l+1)}}\right). \tag{5.89}$$

We can now use Eq. (5.16) to find the matrix elements of F in the Lm_L basis:

$$\begin{aligned}\langle L'm_{L'}S'm_{S'}a'|F^{(\boldsymbol{P})}|Lm_LSm_Sa\rangle &= \delta_{a'a}\delta_{S'S}\delta_{m_{S'}m_S}\\ \times\int d^2\Omega' d^2\Omega\delta(\Omega' - \Omega)F^{(\boldsymbol{P})}(\Omega)\; Y_{Lm_L}(\Omega)Y^*_{L'm_{L'}}(\Omega').\end{aligned} \tag{5.90}$$

Substitute in the expression for $F^{(\boldsymbol{P})}(\Omega)$ and simplify. Define

$$W^{(\boldsymbol{s},\gamma,u)}_{L'm_{L'};\; Lm_L} = -i(4\pi)^{3/2}\sum_{lm}\frac{c^{\boldsymbol{P}}_{lm}(\boldsymbol{q}^{*2})}{q^{*(l+1)}}\int d^2\Omega\; Y^*_{L'm_{L'}}(\Omega)Y^*_{lm}(\Omega)Y_{Lm_L}(\Omega) \tag{5.91}$$

then

$$\langle L'm_{L'}S'm_{S'}a'|F^{(\boldsymbol{P})}|Lm_LSm_Sa\rangle = \delta_{a'a}\delta_{S'S}\delta_{m_{S'}m_S}\frac{\rho_a}{2}\left(\delta_{L'L}\delta_{m_{L'}m_L} + W^{(\boldsymbol{s},\gamma,u)}_{L'm_{L'};\; Lm_L}\right). \tag{5.92}$$

Use Eq. (5.17) to express the above matrix elements in terms of those in the $|Jm_J, LS, a\rangle$ basis states:

$$\begin{aligned}\langle J'm_{J'}, L'S'a'|F^{(\boldsymbol{P})}|Jm_J, LS, a\rangle &= \langle L'm_{L'}S'm_{S'}a'|F^{(\boldsymbol{P})}|Lm_LSm_Sa\rangle\\ \times\langle J'm_{J'}|L'm_{L'}S'm_{S'}\rangle\langle Lm_LSm_S|Jm_J\rangle.\end{aligned} \tag{5.93}$$

We end up with

$$\begin{aligned}\langle J'm_{J'}, L'S'a'|F^{(\boldsymbol{P})}|Jm_J, LS, a\rangle &= \delta_{a'a}\delta_{S'S}\;\frac{\rho_a}{2}\Big\{\delta_{J'J}\delta_{m_{J'}m_J}\delta_{L'L}\\ +\langle J'm_{J'}|L'm_{L'}Sm_S\rangle\langle Lm_LSm_S|Jm_J\rangle W^{(\boldsymbol{s},\gamma,u)}_{L'm_{L'};\; Lm_L}\Big\}.\end{aligned} \tag{5.94}$$

The quantization condition of Eq. (5.42)

$$\det[1 + F^{(\boldsymbol{P})}(S - 1)] = 0, \tag{5.95}$$

is then ready for straightforward use in the $|Jm_J, LS, a\rangle$ basis states.

So far, our manipulations above assumed that the two particles were distinguishable. In such a case, we set $\rho_a = 1$. For indistinguishable particles, we must divide by 2 between all matrices in Eq. (5.37) due to how the closure relation changes in terms of the particle creation/annihilation operators. The second effect of indistinguishable particles comes in the evaluation of $\mathcal{F}$ itself. Given that the two particles are identical, there are two ways of forming the two-particle loops. Hence, we must multiply by 2 for each $\mathcal{F}$. The end effect is to replace $\mathcal{F}$ by $\frac{1}{2}\mathcal{F}$ in Eq. (5.37). Thus, we set $\rho_a = \frac{1}{2}$ for identical particles.

5.5 The RGL shifted zeta functions

In Eq. (5.76), the following quantities emerged as very important:

$$c_{lm}^{\boldsymbol{P}}(\boldsymbol{q}^{*2}) = \frac{\sqrt{4\pi}}{L^3} \sum_{\boldsymbol{k}} \frac{\omega_1^*}{\omega_1} \frac{k^{*l} Y_{lm}(\widehat{\boldsymbol{k}}^*)}{(\boldsymbol{q}^{*2} - \boldsymbol{k}^{*2})} e^{\lambda(\boldsymbol{q}^{*2} - \boldsymbol{k}^{*2})} - \delta_{l0} \mathcal{P} \int \frac{d^3k^*}{(2\pi)^3} \frac{e^{\lambda(\boldsymbol{q}^{*2} - \boldsymbol{k}^{*2})}}{(\boldsymbol{q}^{*2} - \boldsymbol{k}^{*2})}, \tag{5.96}$$

where $\boldsymbol{k} = (2\pi/L)\boldsymbol{n}$ for integer triplets $\boldsymbol{n}$, $\mathcal{P}$ denotes a principal value, $\omega_1 = \sqrt{\boldsymbol{k}^2 + m_1^2}$, and $\omega_1^*, \boldsymbol{k}^*$ are given in Eq. (5.57). These coefficients also depend on m_1 and m_2, in addition to $\boldsymbol{q}^{*2}$, but this dependence is left implicit to simplify the notation.

The summation in Eq. (5.96) is over $\boldsymbol{k} = (2\pi/L)\boldsymbol{n}$, where $\boldsymbol{n}$ is a vector of integers, which are the allowed momenta of the particle of mass m_1. Except for the $\omega_1 = \sqrt{\boldsymbol{k}^2 + m_1^2}$ factor, the summand is expressed entirely in terms of $\boldsymbol{k}^*$. The vector $\boldsymbol{k}^* = \boldsymbol{k}^*(\boldsymbol{k})$ is rather complicated to determine. From Eq. (5.57), we see that

$$k_\parallel^* = \gamma(k_\parallel - \beta\sqrt{\boldsymbol{k}^2 + m_1^2}), \qquad \boldsymbol{k}_\perp^* = \boldsymbol{k}_\perp, \tag{5.97}$$

and the factor $\omega_1^*(\boldsymbol{k})/\omega_1(\boldsymbol{k})$ is similarly complicated. More specifically, the quantities ω_1^*, ω_1 and the Cartesian components of $\boldsymbol{k}^*$ are not simple polynomials of $\boldsymbol{k}^2$.

It has become customary to express these coefficients in terms of functions that were introduced by Lüscher in Ref. [29] for $\boldsymbol{P} = 0$ and generalized by Rummukainen

and Gottlieb for nonzero $\boldsymbol{P}$ in Ref. [31] which involve a summation over a vector $\boldsymbol{r}(\boldsymbol{k})$ given by

$$\boldsymbol{r}_\parallel = \gamma^{-1}(\boldsymbol{k}_\parallel - \varrho \boldsymbol{P}), \quad \boldsymbol{r}_\perp = \boldsymbol{k}_\perp, \quad \gamma = E/E^*, \quad \varrho = \frac{1}{2}\left(1 + \frac{(m_1^2 - m_2^2)}{E^{*2}}\right). \quad (5.98)$$

Although $\boldsymbol{k}^*(\boldsymbol{k})$ and $\boldsymbol{r}(\boldsymbol{k})$ are both dependent on $\boldsymbol{k}$, the key point here is that $\boldsymbol{r}$ is a simpler function of $\boldsymbol{k}$. The manipulations to re-express the coefficients in terms of $\boldsymbol{r}$ are described in Ref. [32].

After a fair bit of work, one finds the following. For a given total momentum $\boldsymbol{P} = (2\pi/L)\boldsymbol{d}$, where $\boldsymbol{d}$ is a vector of integers, we determine the total energy E in the lab frame for a particular two-particle interacting state in our lattice QCD simulations. Then

$$\begin{aligned}
E^* &= \sqrt{E^2 - \boldsymbol{P}^2}, && (5.99)\\
\gamma &= \frac{E}{E^*}, && (5.100)\\
\boldsymbol{q}^{*2} &= \frac{1}{4}E^{*2} - \frac{1}{2}(m_1^2 + m_2^2) + \frac{(m_1^2 - m_2^2)^2}{4E^{*2}}, && (5.101)\\
u^2 &= \frac{L^2 \boldsymbol{q}^{*2}}{(2\pi)^2}, && (5.102)\\
\boldsymbol{s} &= \left(1 + \frac{(m_1^2 - m_2^2)}{E^{*2}}\right)\boldsymbol{d}, && (5.103)\\
\boldsymbol{z} &= \boldsymbol{n} - \gamma^- 1 \left[\frac{1}{2} + (\gamma - 1)s^{-2}\boldsymbol{n}\cdot\boldsymbol{s}\right]\boldsymbol{s}, && (5.104)
\end{aligned}$$

then the coefficients are given by

$$c_{lm}^{\boldsymbol{P}}(\boldsymbol{q}^{*2}) = -\frac{\sqrt{4\pi}}{\gamma L^3}\left(\frac{2\pi}{L}\right)^{l-2} \mathcal{Z}_{lm}(\boldsymbol{s}, \gamma, u^2). \quad (5.105)$$

We define the Rummukainen-Gottlieb-Lüscher (RGL) shifted zeta functions by

$$\mathcal{Z}_{lm}(\boldsymbol{s}, \gamma, u^2) = \sum_{\boldsymbol{n}\in\mathbb{Z}^3} \frac{\mathcal{Y}_{lm}(\boldsymbol{z})}{(\boldsymbol{z}^2 - u^2)} e^{\lambda(u^2 - \boldsymbol{z}^2)} - \frac{\delta_{l0}\gamma}{\sqrt{4\pi}}\mathcal{P}\int d^3y \, \frac{e^{\lambda(u^2 - y^2)}}{(y^2 - u^2)}, \quad (5.106)$$

for constant shift vector $\boldsymbol{s}$, constant boost factor γ, and with ultraviolet regulator

$\lambda \to 0$, and where

$$\mathcal{Y}_{lm}(\boldsymbol{x}) = |\boldsymbol{x}|^l \; Y_{lm}(\widehat{\boldsymbol{x}}) \tag{5.107}$$

are polynomials in the components of $\boldsymbol{x}$. We assume the components of $\boldsymbol{s}$ are real, and that γ, u^2 are real.

To determine the functions $\mathcal{Y}_{lm}(\boldsymbol{x})$ from the standard spherical harmonics, express the integer vector $\boldsymbol{x}$ in spherical polar coordinates (x, θ, ϕ): $x_1 = x\sin\theta\cos\phi$, $x_2 = x\sin\theta\sin\phi$, and $x_3 = x\cos\theta$. Then

$$x\sin\theta e^{i\phi} = x_1 + ix_2, \qquad x\cos\theta = x_3. \tag{5.108}$$

For $m \geq 0$, we have

$$\mathcal{Y}_{lm}(\boldsymbol{x}) = \frac{(-1)^m}{2^l l!}\sqrt{\frac{(2l+1)}{4\pi}\frac{(l-m)!}{(l+m)!}}\;(x_1+ix_2)^m x^{l-m}\left[\frac{d^{(m+l)}}{dv^{(m+l)}}(v^2-1)^l\right]_{v=x_3/x} \tag{5.109}$$

where $x = (x_1^2 + x_2^2 + x_3^2)^{1/2}$, and $\mathcal{Y}_{l,-m}(\boldsymbol{x}) = (-1)^m \mathcal{Y}^*_{lm}(\boldsymbol{x})$. The lowest few functions are found to be

$$\begin{aligned}
\mathcal{Y}_{00}(\boldsymbol{x}) &= \frac{1}{\sqrt{4\pi}}, \\
\mathcal{Y}_{11}(\boldsymbol{x}) &= -\sqrt{\frac{3}{8\pi}}\;(x_1+ix_2), \\
\mathcal{Y}_{10}(\boldsymbol{x}) &= \sqrt{\frac{3}{4\pi}}\;(x_3), \\
\mathcal{Y}_{22}(\boldsymbol{x}) &= \sqrt{\frac{15}{32\pi}}\;(x_1+ix_2)^2, \\
\mathcal{Y}_{21}(\boldsymbol{x}) &= -\sqrt{\frac{15}{8\pi}}\;(x_1+ix_2)\,x_3, \\
\mathcal{Y}_{20}(\boldsymbol{x}) &= \sqrt{\frac{5}{16\pi}}\;\Big(2x_3^2 - x_1^2 - x_2^2\Big).
\end{aligned}$$

The most straightforward way to evaluate the zeta functions is to simply perform the summation in Eq. (5.106) numerically with a computer for various decreasing values of λ, then extrapolate the results to $\lambda \to 0$. Unfortunately, for larger values of l, this is difficult to do, even given the incredible speed of modern computers. Convergence of the $l > 0$ summations depends on subtle angular cancellations due

to the spherical harmonics. Another method is needed. Using tricks described in Ref. [30, 33, 41] finds

$$\begin{aligned}\mathcal{Z}_{lm}(\boldsymbol{s},\gamma,u^2) &= \sum_{\boldsymbol{n}\in\mathbb{Z}^3}\frac{\mathcal{Y}_{lm}(\boldsymbol{z})}{(\boldsymbol{z}^2-u^2)}e^{-\Lambda(\boldsymbol{z}^2-u^2)}+\delta_{l0}\gamma\pi e^{\Lambda u^2}\left(2uD(u\sqrt{\Lambda})-\Lambda^{-1/2}\right)\\ &+ \frac{i^l\gamma}{\Lambda^{l+1/2}}\int_0^1 dt\left(\frac{\pi}{t}\right)^{l+3/2}e^{\Lambda t u^2}\sum_{\substack{\boldsymbol{n}\in\mathbb{Z}^3\\ \boldsymbol{n}\neq 0}}e^{\pi i\boldsymbol{n}\cdot\boldsymbol{s}}\mathcal{Y}_{lm}(\boldsymbol{w})\ e^{-\pi^2\boldsymbol{w}^2/(t\Lambda)}, \quad (5.110)\end{aligned}$$

where $D(x)$ is the Dawson function, defined by

$$D(x) = e^{-x^2}\int_0^x dt\ e^{t^2}. \quad (5.111)$$

We choose $\Lambda \approx 1$, although the final answer is independent of this choice. Choosing Λ near unity allows sufficient convergence speed of the summations. We have written a C++ subroutine to evaluate these functions. Gauss-Legendre quadrature is used to perform the integral, and the method described in Numerical Recipes [42] is used to evaluate the Dawson function, with modifications for double precision.

5.6 The angular integrations

The relationship between the finite-volume two-particle energy E and the infinite-volume scattering amplitudes (and phase shifts) is encoded in the matrix equation:

$$\det[1 + F^{(\boldsymbol{s},\gamma,u)}(S-1)] = 0, \quad (5.112)$$

where S is the usual S-matrix whose elements can be written in terms of the scattering phase shifts, and the F matrix is given by

$$\begin{aligned}F^{(\boldsymbol{s},\gamma,u)}_{J'm_{J'}L'S'a';\ Jm_JLSa} = \frac{\rho_a}{2}\delta_{a'a}\delta_{S'S}\Bigg\{&\delta_{J'J}\delta_{m_{J'}m_J}\delta_{L'L}+W^{(\boldsymbol{s},\gamma,u)}_{L'm_{L'};\ Lm_L}\\ &\times\langle J'm_{J'}|L'm_{L'},Sm_S\rangle\langle Lm_L,Sm_S|Jm_J\rangle\Bigg\}, \quad (5.113)\end{aligned}$$

(S is a total intrinsic spin in the above equation) with

$$W^{(\boldsymbol{s},\gamma,u)}_{L'm_{L'};\ Lm_L} = \frac{2i}{\pi\gamma u^{l+1}} \mathcal{Z}_{lm}(\boldsymbol{s},\gamma,u^2) \int d^2\Omega\ Y^*_{L'm_{L'}}(\Omega) Y^*_{lm}(\Omega) Y_{Lm_L}(\Omega). \tag{5.114}$$

Notice that $F^{(\boldsymbol{s},\gamma,u)}$ is diagonal in channel space, but mixes different total angular momentum sectors, whereas S is diagonal in angular momentum, but has off-diagonal elements in channel space. Also, the matrix elements of $F^{(\boldsymbol{s},\gamma,u)}$ depend on the total momentum $\boldsymbol{P}$ through $\boldsymbol{s}$, whereas the matrix elements of S do not.

To proceed, examine the symmetries and transformation properties of the W matrix in Eq. (5.114). First, if the $m_L, m_{L'}$ parameters change signs, we find that

$$W^{(\boldsymbol{s},\gamma,u)}_{L',-m_{L'};\ L,-m_L} = (-1)^{m_{L'}+m_L+1}\ W^{(\boldsymbol{s},\gamma,u)*}_{L',m_{L'};\ L,m_L}. \tag{5.115}$$

Under interchange of the rows and columns of W, we have

$$W^{(\boldsymbol{s},\gamma,u)}_{Lm_L;\ L'm_{L'}} = -W^{(\boldsymbol{s},\gamma,u)*}_{L',m_{L'};\ L,m_L}. \tag{5.116}$$

If we define

$$w_{lm} = \frac{\mathcal{Z}_{lm}(\boldsymbol{s},\gamma,u^2)}{\gamma\pi^{3/2}u^{l+1}}, \tag{5.117}$$

then explicit expressions for some elements of W are given below:

$$\begin{aligned}
-iW_{0,0;\,0,0} &= w_{0,0} \\
-iW_{0,0;\,1,-1} &= w_{1,-1} \\
-iW_{0,0;\,1,0} &= w_{1,0} \\
-iW_{0,0;\,1,1} &= w_{1,1} \\
-iW_{1,0;\,1,-1} &= \frac{\sqrt{15}}{5} w_{2,-1} \\
-iW_{1,0;\,1,0} &= w_{0,0} + \frac{2\sqrt{5}}{5} w_{2,0} \\
-iW_{1,0;\,1,1} &= \frac{\sqrt{15}}{5} w_{2,1} \\
-iW_{1,1;\,1,-1} &= -\frac{\sqrt{30}}{5} w_{2,-2} \\
-iW_{1,1;\,1,0} &= -\frac{\sqrt{15}}{5} w_{2,-1}
\end{aligned}$$

$$-iW_{1,1;\,1,1} \;=\; w_{0,0} - \frac{\sqrt{5}}{5} w_{2,0}. \tag{5.118}$$

5.7 Block diagonalization

So far we have determined both the matrix F and the scattering matrix S in terms of the basis states labelled $|Jm_J LSa\rangle$. In this basis, the quantization condition

$$\det[1 + F^{(\boldsymbol{s},\gamma,u)}(S-1)] = 0, \tag{5.119}$$

is often problematic due to the need to evaluate the determinant. If we can switch to a basis in which both F and S are block diagonal, then we only need to evaluate the determinant separately in each block.

Define the unitary matrix

$$B^{(R)}_{J'm_{J'}L'S'a';\;Jm_JLSa} = \delta_{J'J}\delta_{L'L}\delta_{S'S}\delta_{a'a} D^{(J)*}_{m_{J'}m_J}(R). \tag{5.120}$$

Under an ordinary spatial rotation R, one can show that

$$F^{(R\boldsymbol{s},\gamma,u)} = B^{(R)}\; F^{(\boldsymbol{s},\gamma,u)}\; B^{(R)\dagger}. \tag{5.121}$$

The above expression also applies for improper transformations R that involve spatial inversion or other reflections.

The result in Eq. (5.121) is very important since it will allow us to substantially reduce (that is, block diagonalize) the F matrix. If R is an element of the little group of $\boldsymbol{P}$ and hence, $\boldsymbol{s}$, then $R\boldsymbol{s} = \boldsymbol{s}$ and we have

$$F^{(\boldsymbol{s},\gamma,u)} = B^{(R)}\; F^{(\boldsymbol{s},\gamma,u)}\; B^{(R)\dagger}, \qquad (R \text{ in little group of } \boldsymbol{P}). \tag{5.122}$$

Multiply by $B^{(R)}$ on the right of both sides of the above equation and use the unitarity of $B^{(R)}$ to obtain

$$F^{(\boldsymbol{s},\gamma,u)}\; B^{(R)} = B^{(R)}\; F^{(\boldsymbol{s},\gamma,u)}. \tag{5.123}$$

Eq. (5.123) tells us that the F matrix commutes with the matrix B. This means that we can simultaneously diagonalize F and B. By rotating into a basis formed by the eigenvectors of B, we can reduce the F matrix into a block diagonal form

which should simplify the evaluation of the determinant needed in the quantization condition. The matrix B involves $D^{(J)*}$, which is the complex conjugate of $D^{(J)}$, so if we use $D^{(J)}$, then we can block diagonalize F^*. But if F^* is block diagonal, then so is the matrix F.

Given the sparseness of the B matrix, a partial diagonalization of F can be achieved by diagonalizing $D^{(J)}_{m'm}(R)$ for each J, or equivalently, by projecting onto the irreducible representations of the little group. These eigenvectors or projections can be labelled by the irrep Λ and irrep row λ of the little group, and possibly an integer n identifying each occurrence of the irrep Λ in the $D^{(J)}_{m'm}(R)$ reducible representation. In other words, we do a change of basis:

$$|\Lambda\lambda n JLSa\rangle = \sum_{m_J} c^{\Lambda\lambda n}_{Jm_J} |Jm_J LSa\rangle \tag{5.124}$$

Making such a change of basis, F will be diagonal in Λ, λ, but not in n_Λ. We can now focus on the matrix elements:

$$F^{(\boldsymbol{s},\gamma,u)(\Lambda,\lambda)}_{J'n'L'S'a';\ JnLSa}. \tag{5.125}$$

To construct the states that transform irreducibly under the little group, for a given J, we apply the standard group theoretical projections onto the $2(2J+1)$ basis vectors $|J^P, J\rangle, |J^P, J-1\rangle, \ldots, |J^P, -J\rangle$ for parity $P = \pm 1$, for the first row $\lambda = 1$ of each irrep of the little group

$$|\Lambda\lambda\rangle = \frac{d_\Lambda}{g_\mathcal{G}} \sum_{R\in\mathcal{G}} \Gamma^{(\Lambda)*}_{\lambda\lambda}(R) D^{(J)}_{m'm_J}(R)\ |J^P m'\rangle, \tag{5.126}$$

where $\mathcal{G}$ denotes the little group, $g_\mathcal{G}$ is the order of the little group (the number of elements), and d_Λ is the dimension of the irrep Λ, and $\Gamma^{(\Lambda)}(R)$ is the unitary matrix representing R in the Λ irrep. The matrix of spatial inversion is diagonal, with $+1$ on the diagonal elements corresponding to the even parity states and -1 for the diagonal elements associated with the odd parity states. If the irrep Λ does not occur in the J rep of $SU(2)$ subduced to $\mathcal{G}$, all of the resulting vectors will be zero. If the irrep Λ occurs once in the subduction, then only one nonzero resulting vector will occur, which can then be suitably normalized. If the Λ irrep occurs more than once, then there is some freedom in choosing the basis vectors. We make an arbitrary choice

Table 5.1: The basis vectors that block diagonalize the F matrix for total zero momentum. Each basis vector is labelled by an irreducible representation Λ of the little double group O_h^D, the row λ (as defined in Ref. [18]), the spin J, and the occurrence number n of Λ in the subduction of J^η to the little group. In the first column, $\eta = g$ for even parity, $\eta = u$ for odd parity. In the last column, $|J^\eta, m_J\rangle$ refers to $|Jm_JLSa\rangle$, where $\eta = \eta_1\eta_2(-1)^L$ and η_j is the intrinsic parity of particle $j = 1, 2$. Only spins $J \leq 1$ are considered in this table.

Λ	λ	J	n	Basis vectors
$A_{1\eta}$	1	0	1	$\|0^\eta, 0\rangle$
$T_{1\eta}$	1	1	1	$\frac{1}{\sqrt{2}}(-\|1^\eta, 1\rangle + \|1^\eta, -1\rangle)$
$T_{1\eta}$	2	1	1	$\frac{i}{\sqrt{2}}(\|1^\eta, 1\rangle + \|1^\eta, -1\rangle)$
$T_{1\eta}$	3	1	1	$\|1^\eta, 0\rangle$

based on simplicity of the results, but ensuring the choices are orthonormal. We apply a Gram-Schmidt procedure to the resulting vectors.

Once we have basis vectors for the first row $\lambda = 1$ of all Λ irreps, we then obtain the partner basis vectors for the other rows μ using the transfer operation

$$|\Lambda\mu\rangle = \frac{d_\Lambda}{g_\mathcal{G}} \sum_{R\in\mathcal{G}} \Gamma^{(\Lambda)*}_{\mu\lambda}(R)\ R|\Lambda\lambda\rangle. \tag{5.127}$$

Our choices of irreducible representation matrices are presented in Ref. [18], and the irrep labels for the various little groups are listed in Ref. [18] as well. Given these choices, we apply the above procedure, and the resulting basis states are summarized in Tables 5.1, 5.2, 5.3, and 5.4, for spins $J \leq 1$.

5.8 Application to $\pi\pi$ scattering

For single-channel $\pi\pi$ scattering, $s_1 = s_2 = 0$, so $S = 0$ and $J = L$, in which case Eq. (5.113) simplifies to

$$F^{(\boldsymbol{s},\gamma,u)}_{L'm_{L'};\ Lm_L} = \frac{\rho_a}{2}\left(\delta_{L'L}\delta_{m_{L'}m_L} + W_{L'm_{L'};\ Lm_L}\right). \tag{5.128}$$

Table 5.2: The basis vectors that block diagonalize the F matrix for on-axis total momentum (0,0,1). Each basis vector is labelled by an irreducible representation Λ of the little double group C_{4v}^D, the row λ (as defined in Ref. [18]), the spin J, and the occurrence number n of Λ in the subduction of J^P to the little group. In the last column, $|J^\eta, m_J\rangle$ refers to $|Jm_JLSa\rangle$, where $\eta = \eta_1\eta_2(-1)^L$ and η_j is the intrinsic parity of particle $j = 1, 2$. Only integer spins $J \leq 1$ are considered in this table.

Λ	λ	J	n	Basis vectors
A_1	1	0	1	$\|0^+, 0\rangle$
A_2	1	0	1	$\|0^-, 0\rangle$
A_1	1	1	1	$\|1^-, 0\rangle$
A_2	1	1	1	$\|1^+, 0\rangle$
E	1	1	1	$\frac{1}{\sqrt{2}}(\|1^+, 1\rangle + \|1^+, -1\rangle)$
E	2	1	1	$\frac{i}{\sqrt{2}}(-\|1^+, 1\rangle + \|1^+, -1\rangle)$
E	1	1	2	$\frac{1}{\sqrt{2}}(-\|1^-, 1\rangle + \|1^-, -1\rangle)$
E	2	1	2	$\frac{i}{\sqrt{2}}(\|1^-, 1\rangle + \|1^-, -1\rangle)$

Table 5.3: The basis vectors that block diagonalize the F matrix for planar-diagonal total momentum (0,1,1). Each basis vector is labelled by an irreducible representation Λ of the little double group C_{2v}^D, the row λ (as defined in Ref. [18]), the spin J, and the occurrence number n of Λ in the subduction of J^P to the little group. In the last column, $|J^\eta, m_J\rangle$ refers to $|Jm_JLSa\rangle$, where $\eta = \eta_1\eta_2(-1)^L$ and η_j is the intrinsic parity of particle $j = 1, 2$. Only integer spins $J \leq 1$ are considered in this table.

Λ	λ	J	n	Basis vectors
A_1	1	0	1	$\|0^+, 0\rangle$
A_2	1	0	1	$\|0^-, 0\rangle$
A_1	1	1	1	$\frac{1}{2}(\|1^-, 1\rangle - i\sqrt{2}\|1^-, 0\rangle + \|1^-, -1\rangle)$
A_2	1	1	1	$\frac{1}{2}(\|1^+, 1\rangle - i\sqrt{2}\|1^+, 0\rangle + \|1^+, -1\rangle)$
B_1	1	1	1	$\frac{1}{2}(\|1^+, 1\rangle + i\sqrt{2}\|1^+, 0\rangle + \|1^+, -1\rangle)$
B_1	1	1	2	$\frac{1}{\sqrt{2}}(-\|1^-, 1\rangle + \|1^-, -1\rangle)$
B_2	1	1	1	$\frac{1}{\sqrt{2}}(\|1^+, 1\rangle - \|1^+, -1\rangle)$
B_2	1	1	2	$\frac{1}{2}(\|1^-, 1\rangle + i\sqrt{2}\|1^-, 0\rangle + \|1^-, -1\rangle)$

Table 5.4: The basis vectors that block diagonalize the F matrix for cubic-diagonal total momentum (1,1,1). Each basis vector is labelled by an irreducible representation Λ of the little double group C_{3v}^D, the row λ (as defined in Ref. [18]), the spin J, and the occurrence number n of Λ in the subduction of J^P to the little group. In the last column, $|J^\eta, m_J\rangle$ refers to $|Jm_JLSa\rangle$, where $\eta = \eta_1\eta_2(-1)^L$ and η_j is the intrinsic parity of particle $j = 1, 2$. Only integer spins $J \leq 1$ are considered in this table.

Λ	λ	J	n	Basis vectors
A_1	1	0	1	$\|0^+, 0\rangle$
A_2	1	0	1	$\|0^-, 0\rangle$
A_1	1	1	1	$-\frac{1}{\sqrt{6}}(-\sqrt{2}\|1^-, 1\rangle + (1+i)\|1^-, 0\rangle + i\sqrt{2}\|1^-, -1\rangle)$
A_2	1	1	1	$-\frac{1}{\sqrt{6}}(-\sqrt{2}\|1^+, 1\rangle + (1+i)\|1^+, 0\rangle + i\sqrt{2}\|1^+, -1\rangle)$
E	1	1	1	$\frac{1}{\sqrt{6}}(\|1^+, 1\rangle + (1+i)\sqrt{2}\|1^+, 0\rangle - i\|1^+, -1\rangle)$
E	2	1	1	$\frac{1}{\sqrt{2}}(i\|1^+, 1\rangle - \|1^+, -1\rangle)$
E	1	1	2	$\frac{1}{\sqrt{2}}(\|1^-, 1\rangle + i\|1^-, -1\rangle)$
E	2	1	2	$\frac{1}{\sqrt{6}}(i\|1^-, 1\rangle - (1-i)\sqrt{2}\|1^-, 0\rangle + \|1^-, -1\rangle)$

5.8.1 S-wave scattering

In the simplest case of S-wave scattering, assume $\langle L'm_{L'}|S-1|Lm_L\rangle = 0$ for $L, L' > 0$. Then the determinant equation $\det[1 + F^{(\boldsymbol{s},\gamma,u)}(S-1)] = 0$ becomes very simple. The matrix $F^{(\boldsymbol{s},\gamma,u)}(S-1)$ has nonzero entries only in its first column corresponding to $L = m_L = 0$. Hence, the diagonal elements of $1 + F^{(\boldsymbol{s},\gamma,u)}(S-1)$ are all unity, except for the first element, and the off-diagonal elements are nonzero only in its first column. Taking the determinant is simple, yielding

$$\det[1 + F^{(\boldsymbol{s},\gamma,u)}(S-1)] = 1 + \tfrac{1}{2}(1 + iw_{00})(e^{2i\delta_0} - 1) = 0. \tag{5.129}$$

Using

$$e^{2i\delta_0} - 1 = \frac{2i}{\cot\delta_0 - i}, \tag{5.130}$$

the above equation becomes

$$\cot\delta_0 = w_{00} = \frac{\mathcal{Z}_{00}(\boldsymbol{s}, \gamma, u^2)}{\gamma\pi^{3/2}u}, \tag{5.131}$$

assuming the particles are *not* identical, such as in $\pi^+\pi^-$ scattering. Note that $w_{0,0}$ is real since $\mathcal{Z}_{l0}$ is real. To emphasize this, we write

$$\cot\delta_0 = \mathrm{Re}w_{00} = \frac{\mathrm{Re}\mathcal{Z}_{00}(\boldsymbol{s},\gamma,u^2)}{\gamma\pi^{3/2}u}. \tag{5.132}$$

5.8.2 P-wave scattering

In the case of P-wave scattering, we assume $\delta_L = 0$ for all L except $L = 1$. Hence, the matrix elements of $S-1$ are all zero, except for diagonal entries with $L = 1$. This means the matrix $F(S-1)$ has non-zero entries only for *columns* with $L = 1$. The matrix $1 + F(S-1)$ has the form

$$Q = 1 + F(S-1) = \begin{bmatrix} 1 & Q^{(a)} & 0 \\ 0 & Q^{(d)} & 0 \\ 0 & Q^{(b)} & 1 \end{bmatrix},$$

where $Q^{(d)}$ refers to the block whose columns and rows involve $L = 1$ only. Given the above form, one easily sees that $\det[1 + F(S-1)] = \det Q^{(d)}$. So we only need to consider the block involving $L = 1$ only. The $Q^{(d)}$ block is a 3×3 matrix. The basis states are $|1^-, 1\rangle,\ |1^-, 0\rangle,\ |1^-, -1\rangle$. The parity must be $\eta_\pi^2(-1)^L = -1$. In all cases, we will be able to reduce the 3×3 matrix to diagonal form, where each diagonal element has the form

$$F = \tfrac{1}{2}(1 + i\mathcal{W}). \tag{5.133}$$

Then the determinant equation is trivial (using $\rho_a = 1$ for distinguishable pions):

$$1 + \tfrac{1}{2}(1 + i\mathcal{W})(e^{2i\delta_1} - 1) = 0. \tag{5.134}$$

Using

$$e^{2i\delta_1} - 1 = \frac{2i}{\cot\delta_1 - i}, \tag{5.135}$$

the above equation becomes

$$\cot\delta_1 = \mathcal{W}. \tag{5.136}$$

Since we will only need the matrix elements of $\mathcal{W}$ corresponding to the three states

Table 5.5: Expressions for the P-wave phase shifts relevant for $I = 1$ $\pi\pi$ scattering.

$\boldsymbol{d}$	Λ	$\cot\delta_1$
(0,0,0)	T_{1u}^+	$\mathrm{Re}\ w_{0,0}$
(0,0,1)	A_1^+	$\mathrm{Re}\ w_{0,0} + \frac{2}{\sqrt{5}}\mathrm{Re}\ w_{2,0}$
	E^+	$\mathrm{Re}\ w_{0,0} - \frac{1}{\sqrt{5}}\mathrm{Re}\ w_{2,0}$
(0,1,1)	A_1^+	$\mathrm{Re}\ w_{0,0} + \frac{1}{2\sqrt{5}}\mathrm{Re}\ w_{2,0} - \sqrt{\frac{6}{5}}\mathrm{Im}\ w_{2,1} - \sqrt{\frac{3}{10}}\mathrm{Re}\ w_{2,2}$,
	B_1^+	$\mathrm{Re}\ w_{0,0} - \frac{1}{\sqrt{5}}\mathrm{Re}\ w_{2,0} + \sqrt{\frac{6}{5}}\mathrm{Re}\ w_{2,2}$,
	B_2^+	$\mathrm{Re}\ w_{0,0} + \frac{1}{2\sqrt{5}}\mathrm{Re}\ w_{2,0} + \sqrt{\frac{6}{5}}\mathrm{Im} w_{2,1} - \sqrt{\frac{3}{10}}\mathrm{Re}\ w_{2,2}$
(1,1,1)	A_1^+	$\mathrm{Re}\ w_{0,0} + 2\sqrt{\frac{6}{5}}\mathrm{Im}\ w_{2,2}$
	E^+	$\mathrm{Re}\ w_{0,0} - \sqrt{\frac{6}{5}}\mathrm{Im}\ w_{2,2}$

$|1^-,1\rangle,\ |1^-,0\rangle,\ |1^-,-1\rangle$, we only have to consider

$$\begin{aligned} -iW_{1,1;\,1,1} &= w_{0,0} - \tfrac{1}{\sqrt{5}} w_{2,0} \\ -iW_{1,1;\,1,0} &= -\sqrt{\tfrac{3}{5}} w_{2,-1} \\ -iW_{1,1;\,1,-1} &= -\sqrt{\tfrac{6}{5}} w_{2,-2} \\ -iW_{1,0;\,1,0} &= w_{0,0} + \tfrac{2}{\sqrt{5}} w_{2,0}. \end{aligned} \tag{5.137}$$

We can use Eqs. (5.115) and (5.116) to get the other needed matrix elements. Also, we know that w_{l0} is real for all l.

We carry out the block diagonalization using the results given in Tables 5.2, 5.3, and 5.4, and evaluate the resulting determinants. We summarize our results in Table 5.5.

Chapter 6

Analysis

6.1 Energy Extraction from Correlators

The spectral representation of the correlation functions is given by Eq. 2.29. This indicates that the spectrum of stationary states excited by a particular operator can be determined by the decay rates in the temporal evolution of the correlator. The lowest energy can be extracted by looking at the large time behavior of the correlator since the excited states decay away more quickly. However, the signal to noise ratio falls with time, so the correlator must be analyzed at times before the signal is dominated by statistical noise.

6.2 The effective mass

A common way of visualizing the properties of a correlator is to compute and plot a so-called "effective mass" defined by

$$m^{\text{eff}}(t) = -\frac{1}{\Delta t} \ln \left(\frac{C(t+\Delta t)}{C(t)} \right). \tag{6.1}$$

The effective mass is a function of time separation t that tends to the exact energy of the lowest-lying state created by the operator of the correlator as t becomes large. Generally, the effective mass decreases with time until it levels off at its plateau value when the contributions from higher-lying states become negligible. Fig. 6.1 is an example of a correlator and the corresponding effective mass. At times before the

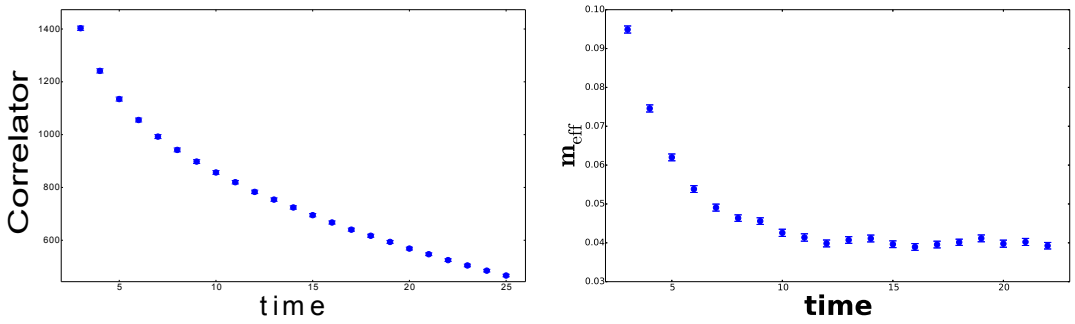

(a) Correlator (b) Effective Mass

Figure 6.1: Plot of an example two-point correlation function (left) and its effective mass (right). At small times, the effective mass is decreasing, but at larger times, the effective mass levels off at a plateau, indicating the correlator is dominated by a single exponential decay. This correlator is for the $I = 1$, $S = 0$, A_{1u}^- channel (corresponding to the pion) using the same single-hadron operator on the source and sink.

plateau, the effective mass shows contributions from higher energy levels. Effective masses often have error bars which increase significantly for larger time separations.

6.3 Correlator Matrices

It is not feasible to extract more than one energy by fitting to a single correlation function given the small number of times at which we can typically estimate the correlator. To determine the energies of higher-lying states, the best way to proceed is to determine estimates for a matrix of correlators and exploit orthogonality.

For a particular channel, we design a set of N interpolating operators $\{O_i\}$ which have the same transformation properties, then evaluate the matrix elements

$$C_{ij}(t) = \langle 0|O_i(t+t_0)O_j^\dagger(t_0)|0\rangle. \tag{6.2}$$

This is an $N \times N$ matrix for each t, which is the temporal separation between the source time t_0 and the sink time $t_f = t + t_0$ requiring that t be positive due to time ordering. We design our operators such that $C_{ij}(t)$ is Hermitian, so to save on computing resources, we only have to produce the upper or lower triangle of the

matrix. It is convenient to work with a rescaled correlation matrix

$$\hat{C}_{ij}(t) = \frac{C_{ij}(t)}{\sqrt{C_{ii}(t_n)C_{jj}(t_n)}}, \tag{6.3}$$

where the reference normalization time t_n is chosen to be a very early time, such as $t_n = 3$, where the error on the correlator is small. This rescaled correlator matrix is the starting point for our analysis.

The rescaled matrix $\hat{C}$ is then rotated to produce a matrix $\widetilde{C}$ that is diagonal on two time slices τ_i and τ_d. Rotating the matrix to be diagonal is tantamount to defining a new set of operators using linear combinations of the original set such that each only has significant overlap with a single level. The rotated correlation matrix will be the identity matrix at τ_i and exactly diagonal at time τ_d. The rotation coefficients are determined by solving the generalized eigenvalue problem specified by

$$\hat{C}(\tau_d)y = \lambda\hat{C}(\tau_i)y. \tag{6.4}$$

Alternatively, one can solve

$$\hat{C}(\tau_i)^{-1/2}\hat{C}(\tau_d)\hat{C}(\tau_i)^{-1/2}x = \lambda x, \tag{6.5}$$

where $x = \hat{C}(\tau_i)^{1/2}y$. Using the eigenvectors y as columns, we build a matrix U. This is a unitary matrix which can be used to rotate our correlator matrix. The rotated correlator matrix is defined by

$$\widetilde{C}_{ij}(t) = U^\dagger\hat{C}(t)U. \tag{6.6}$$

This guarantees that $\widetilde{C}_{ij}(\tau_i) = I$ and $\widetilde{C}_{ij}(\tau_d)$ is diagonal. However, we try to choose values of τ_i and τ_d such that $\widetilde{C}(t)$ remains diagonal for all $t > \tau_d$. After the rotation, the off-diagonals are inspected to ensure they are zero within statistical error.

If the set of operators is not sufficiently linearly independent, the matrix can become ill-conditioned. Due to statistical fluctuations, the matrix may have zero or even negative eigenvalues at large times. This poses a serious problem as the formulas above are not valid if $\hat{C}$ is not positive definite. As N becomes large, it often becomes necessary to inspect the eigenvectors of $\hat{C}$ and exclude those vectors which correspond to a negative or very small eigenvalue.

6.4 Error Estimation

We use standard resampling techniques to evaluate the statistical uncertainties in our Monte Carlo estimates. In particular, we use the jackknife and bootstrap resampling methods.

6.4.1 Jackknife

A Monte Carlo estimate of an observable, f, is given by its mean value

$$\langle f \rangle = \frac{1}{N} \sum_i f(U_i), \tag{6.7}$$

where $f(U_i)$ is the value of f using the i-th gauge-field configuration in the Monte Carlo ensemble, and N is the number of such configurations in the ensemble. We assume the number of RHMC trajectories between retained configurations in the ensemble is such that autocorrelations are negligible. The jackknife variance is then defined by

$$\sigma^2(f) = \frac{N-1}{N} \sum_{i=1}^{N} \left(\langle f \rangle_i - \langle f \rangle \right)^2 \tag{6.8}$$

where $\langle f \rangle_i$ is the mean value of f using all configurations in the ensemble *except* the i-th one. In this work, we use jackknife errors for simple observables, such as the correlator values and effective masses. For more complicated observables, such as parameters obtained from fitting functional forms to our Monte Carlo estimates, bootstrap resampling is used.

6.4.2 Bootstrap

The bootstrap resampling method works by building new sets of configurations from the original set randomly with repeats allowed. A sufficiently large number N_b is chosen to be the number of new configuration sets to generate. Generally, N_b is set to ≈ 1000. For each new bootstrap set of configurations, N configurations from the original set are selected randomly with equal probabilities, allowing the same configuration to be chosen more than once. This results in N_b samplings of N data values each. The observable, such as a fit, is computed on each of the N_b samplings.

Let f_b denote the mean value of f evaluated using the b-th sampling. Two quantities are calculated

$$\widetilde{f} = \frac{1}{N_b}\sum_{b=1}^{N_b} f_b, \quad \text{and} \quad \sigma_{\widetilde{f}}^2 = \frac{1}{N_b}\sum_{b=1}^{N_b}(f_b - \widetilde{f})^2, \tag{6.9}$$

where $\widetilde{f}$ is the bootstrap estimate of the mean value and $\sigma_{\widetilde{f}}^2$ is the bootstrap estimate of the variance. The observable is then reported either using $\widetilde{f} \pm \sigma_{\widetilde{f}}$ or $\widetilde{f}^{+\sigma_{\text{up}}}_{-\sigma_{\text{down}}}$, where 84% of all bootstrap samplings lie below $\widetilde{f} + \sigma_{\text{up}}$ and 84% lie above $\widetilde{f} - \sigma_{\text{down}}$. This gives asymmetric errors that correspond within a standard deviation. Additionally, one can use the difference of the bootstrap average $\widetilde{f}$ and the average on the full data set to give the bias of the bootstrap resampling. If this difference is large, the number of bootstrap samples may be too low, or indicates that the true average may be far from the average given by limited statistics.

6.5 Fitting

The Monte Carlo method gives us statistical estimates of the correlation functions $C_{ij}(t)$. The spectral representations of the correlators can then be used to extract the physical observables, such as energies. Typically, this involves fitting the correlator estimates using fit forms involving the physical observables. This section describes how such fits are carried out, and what fit forms are used.

6.5.1 Correlated-χ^2 fitting

If N quantities are believed to be described by some model function $f(\alpha, i)$ involving some number of parameters α, then estimates of the parameters α are usually determined by minimizing

$$\chi^2 = \sum_{i=1}^{N} \frac{(d_i - f(\alpha, i))^2}{\sigma_i^2}, \tag{6.10}$$

where d_i denote the mean values of the measurements of the N quantities, and σ_i are the variances of the measurements. The above formula assumes that the measurements of the quantities are all done independently.

Here, this is not true since the estimates of all correlators are done using the same Monte Carlo ensemble. To account for this, we perform a correlated-χ^2 minimization which incorporates the covariances of the measurements:

$$\chi^2 = \sum_{i,j=1}^{N} (d_i - f(\alpha, i))\ \mathrm{Cov}_{ij}^{-1}\ (d_j - f(\alpha, j)). \tag{6.11}$$

Note that the model function $f(\alpha, i)$ can explicitly depend only on the parameters α and other exactly known identifying information i about the data, but not on the values of the data d_i in the above equation.

In our study, the stationary-state energies are determined by fitting a model function to a temporal correlation function. Here, each "data" points is the value of a rotated correlator at a particular time separation: $\widetilde{C}(t)$, and we estimate the covariance matrix using

$$\mathrm{Cov}(t, t') \approx \frac{1}{N-1} \left\langle \left(\widetilde{C}(t) - \left\langle \widetilde{C}(t) \right\rangle \right) \left(\widetilde{C}(t') - \left\langle \widetilde{C}(t') \right\rangle \right) \right\rangle \tag{6.12}$$

where the angle brackets indicate average over all of the configurations. Using this, we define our correlator χ^2 to be

$$\chi^2 = \sum_{t,t'} \left(\widetilde{C}(t) - f(t) \right) \mathrm{Cov}^{-1}(t, t') \left(\widetilde{C}(t') - f(t') \right). \tag{6.13}$$

To perform fits to the scattering phase shift requires fitting to a function which has uncertainty in the center of mass energy which is the input to the fit function. This uncertainty is correlated with the uncertainty of the phase shift, δ. To account for this the total co-variance is computed using a fit function $f(\alpha, E_i)$

$$\mathrm{Cov}(\delta_i, \delta_j) + \frac{\partial f}{\partial E_i} \frac{\partial f}{\partial E_j} \mathrm{Cov}(E_i, E_j) - \frac{\partial f}{\partial E_j} \mathrm{Cov}(\delta_i, E_j) - \frac{\partial f}{\partial E_i} \mathrm{Cov}(E_i, \delta_j) \tag{6.14}$$

We carry out the minimization using the *Minuit* minimization suite [43]. Mean values of the parameters are determined from a fit using the entire ensemble. Bootstrap resampling is then done to estimate the uncertainities on the fit parameters.

6.5.2 Single Exponential Fits and Temporal Wrap Around

Because the lattice is periodic in time, for particles with large correlation lengths, we can expect there to be small signals from particles/antiparticles propagating backwards in time. To take this into account, we can use a fit function

$$f^{(0)}(t) = A\exp(-Et) + A\exp(-E\,(T-t)), \tag{6.15}$$

where T is the temporal length of the lattice, or equivalently, we can use the form

$$f'^{(0)}(t) = A'\cosh\left(-E\left(t-\frac{T}{2}\right)\right), \tag{6.16}$$

where the fit parameters are the energy E and the overlaps A or A'. Both forms above assume that the operator creating the forward-propagating and backward-propagating particles/antiparticles is either symmetric or antisymmetric under time reversal.

The wrap around effects are more complicated for two-meson states. Then one has the additional possibility of one meson propagating forward in time and the other propagating backward. This contributes a factor $\propto \exp(-E_m T)$ where E_m is the energy of one of the mesons. Since this is not dependent on time, it is simply a constant and can be mocked up by adding a constant as a new parameter to the fit function as below:

$$f^{(1)}(t) = A\exp(-Et) + A\exp(-E\,(T-t)) + D \tag{6.17}$$

Alternatively, this can be removed by defining a subtracted correlator by $C'(t) = C(t_s) - C(t)$ and then fitting to $C'(t)$ with an appropriate adjusted fit function. The subtracted correlator method uses one less parameter in the fit function, but testing found that fitting to the three parameter fit with a constant always gave equivalent results. The effects due to temporal wrap around are nonnegligible on our smaller lattices. However, on the $32^3 \times 256$ lattice, the temporal extent is so large that the constant term was always found to be negligible.

We can fit to each diagonal element of the rotated correlator matrix for a range of time separations $t_{\min}$ to $t_{\max}$ using the above model functions. Such fits are known as "single exponential" fits, even though a cosh behavior is used, since the forward exponential tends to dominate the signal, and hence, the fit. One would like to choose

t_{min} as small as possible to make use of a large number of data points. However, contributions from higher-lying states eventually cause the quality of fit to dramatically drop as t_{min} is made smaller and smaller. Thus, finding an appropriate t_{min} can be time consuming, especially when fitting to a large number of correlators. We must use a t_{min} that produces a good quality of fit. At large times, the correlator can be fit out to t_{max} until the value of the correlator is consistent with zero. A measurement of the correlator which is consistent with zero indicates the signal is indistinguishable from statistical noise.

The effect of t_{tmin} can be seen in Fig. 6.2 showing the fit value for the energy parameter against t_{min} for a fixed t_{max} on an example correlator. The color on the plot indicates the quality of fit. We can see that including early times in the fit gives a larger fit value, but the quality of fit is unacceptable. Eventually, the fit values reach a plateau once the correlator is dominated by a single exponential. The single exponential fit gives a good χ^2 value for the region without excited state contamination. It is possible to programmatically determine the appropriate fit range using the quality of the fit, but this can be time consuming, especially when fitting to a large number of correlators.

6.5.3 Two-exponential Fits

The so-called "single exponential" fits described in the previous section tend to be sensitive to the choice of t_{min}. An easy way to avoid this sensitivity is to use a "two-exponential" fit form. It is not actually expected that the excited-state contamination will be contributing from only a single level, but the extra parameters from the second exponential are able to effectively mock up their effect. Provided there is enough data in the region dominated by the single exponential, the fit values of the parameters in the asymptotic exponential should agree with those obtained from single-exponential fits. The two-exponential function can also incorporate the effects of finite temporal extent discussed in the previous section giving a form:

$$f^{(2)} = A\exp(-Et)\left[1 + B\exp(-\Delta^2 t)\right] + A\exp(-E\,(T-t))\left[1 + B\exp(-\Delta^2\,(T-t))\right]. \quad (6.18)$$

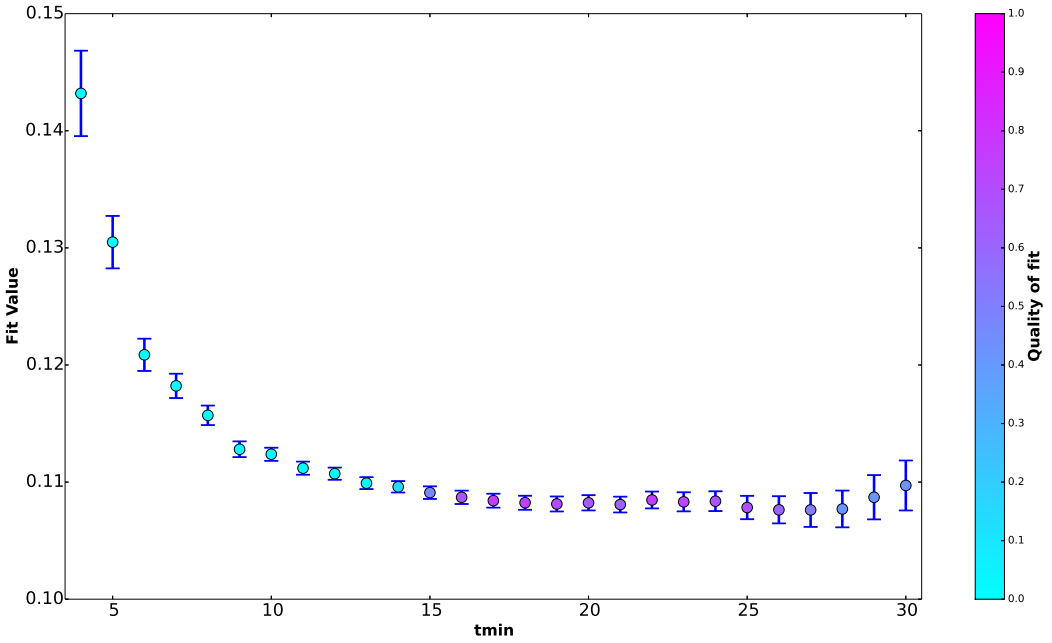

Figure 6.2: A plot of the fit values of the energy parameter using a cosh model function. For each point, the same value of t_{max} is used, but the choice of t_{min} is varied, and shown on the horizontal axis. The color of each point indicates the quality of the fit. Choosing a t_{min} to be in the region dominated by a single exponential gives a good fit and is stable to changes of t_{min}. This correlator is for the lightest state in the channel with $P = (0, 0, 1)$, $I = 1$, $S = 0$, A_1^+.

Writing the two exponential function in this way includes a second exponential with an amplitude of $A_2 = AB$ and a decay rate of $E_2 = E + \Delta^2$, ensuring $E_2 > E$.

Using a two-exponential fit allows a larger range of times to include when fitting. In particular, t_{min} can be chosen much smaller and still maintain a good quality of fit. Also, we can often get good qualities of fit for a large number of different correlators using the same t_{min}, which dramatically simplifies the analysis of our spectrum and phase shifts. Note that adequate statistics and enough time separations are needed to be able to minimize with respect to the four parameters in the model function. If the minimizer fails, we fall back to the single exponential fit. However, this does not happen very often, and usually only for very high lying levels.

For the two-exponential fits, t_{max} was chosen to be the largest time separation for which the correlator value was still comparable to or larger than its stastistical uncertainty. Usually, this was the largest time separation which was computed. The start of the fit range t_{min} was chosen to be typically between 3 and 8.

Chapter 7

Results

Our main results using the analysis described in the previous chapters are described in this chapter. These results are obtained from correlators on the large 32^3_860 lattice. First, the energy spectrum of the stationary states of the $I = 1, S = 0$, T_{1u}^+ channel of zero total momentum which can be created by our single and two hadron operators is presented. Previous analysis of this channel has been done on the smaller 24^3_840 lattice in Ref. [44]. Secondly, the $I = 1$, $\pi\pi$ scattering phase shift is computed from the finite-volume energies of the two-pion states in many channels with zero and nonzero total momenta below the inelastic threshold. The mass and width of the ρ resonance are then deduced from this phase shift.

7.1 Computational Details

Generating the Monte Carlo ensembles of gauge configurations was carried out mainly on the Department of Energy (DOE) sponsored Jaguar system at Oak Ridge National Laboratory's Leadership Computing Facility and on the University of Tennessee Kraken system, sponsored by the National Science Foundation (NSF). For the ensembles used in our work, approximately 200 million core-hours were used in this first stage.

The second stage of the computations involves computing the quark propagators Q^{-1}. Our software was written in C++ with MPI and OpenMP threading, and the USQCD QDP++ library[45] was used. A key component of this stage of the computations, as well as the first stage, is multiplying the Dirac matrix $\mathcal{M}$ onto a vector. Much work has gone into optimizing this operation since it dominates

the computational cost. Even-odd preconditioning is used, and some of the low-level matrix multiplies were written in assembly language with SSE3 Intel intrinsics. Calculations in this second phase were done mainly on Kraken, totally approximately 100 million core-hours, with jobs typically utilizing a few thousand cores.

The later stages of the computations involve evaluating the hadron source and sink functions and carrying out the correlator contractions that tie together the $\mathcal{M}^{-1}$ elements. These operations are dependent on I/O. Access to large lustre partitions is crucial in the final stages, making systems such as those available through the Extreme Science and Engineering Discovery Environment (XSEDE) of the NSF ideal. We are currently using Stampede at the Texas Advanced Computing Center (TACC) for this final part of our computations. Computing the hadrons and making the correlators has utilized about 40 million core-hours to date, and storage of intermediate quantities totals nearly 300 terabytes on TACC's Ranch tape system.

The software used in our calculations is driven by input in XML format. Given the multi-stage nature of the computations and the need to represent thousands of different single- and multi-hadron operators, as well as the myriad of files that must be accessed, the XML input files required are rather complicated. The complex logistics of carrying out the tens of thousands of runs done for our study and handling the thousands of file movements between tape and scratch disk with checksum testing necessitated the use of a sophisticated scripting language. The object-oriented Ruby language was used and worked very well for us. With Ruby, we were able to build up the complicated XML structures needed to drive our code and to make the job-submission scripts. In fact, the time spent developing our ruby scripts was not a negligible fraction of that taken to develop our C++ code.

7.2 T_{1u}^{+} Spectrum on 32^3_860

This section presents the results of the spectrum of stationary states excited by our $q\overline{q}$ and multi-meson operators for the $I = 1$, $S = 0$, T_{1u}^{+} channel of zero total momentum. In the continuum, this channel should contain the $\rho(770)$ meson, as well has a handful of its excitations. In addition to the spin-1 ρ resonances, the T_1 irrep of O_h also includes the spin-3 states, such as the $\rho_3(1690)$.

7.2.1 Operator Selection

Operators were selected with the goal of having some coupling to all stationary states with significant single-hadron and two-meson content and energies below $\approx$ 2GeV. This was done by selecting a large number of single and two-particle operators with the appropriate symmetries which roughly matched the states expected to appear in the absence of interactions. This selection utilized a list of the expected states by assuming non-interacting energies and simply summing the masses of meson pairs which can be produced in this channel. This is just a guide to select enough operators of each flavor and momentum which should have large overlaps with the states we are interested in. In reality, our operators will not couple to a single stationary state, but will excite many states. However, choosing operators using some information about what states are expected to appear should ensure that no expected states are missed.

More specifically, 10 single-hadron operators that transformed according to the T_{1u}^{+} irrep at rest were included. Tables 7.1-7.2 contain lists of two-meson combinations with particular momenta which are expected to appear in this channel below $\approx$ 2GeV. For each meson pair in the table, one or more operators were included. Such operators were referred to as primary two-meson operators. As an example, the lightest expected two-hadron state in the channel is two pions, each with a single unit of momentum. This corresponds to operators where each meson is an isovector, with one unit of momentum, and each transforms as A_2^-. This is because pions are spin zero particles with negative parity, which at rest corresponds to A_{1u} subduced to the little group A_2 for on-axis momenta. This process is repeated for each of the two-meson expected levels. In order to ensure many of the low-lying states have good signals, a handful of additional operators, known as secondary operators, were selected which are listed in Table 7.3.

Correlators for all of the operators listed were evaluated. However, some of the operators turned out to be unacceptably noisy, and did not couple strongly to any of the low-energy states. The operators whose diagonal correlators were zero within error before time-slice 20 were removed in the subsequent analysis. The list was pruned down to a total of 63 operators.

Our goal was to ensure that all of the lowest energy states dominated by single-meson and two-meson components had a large overlap with at least one of the operators included. By including as many operators as were feasible, we minimized the possibility of our operator set missing important levels. Note that some three- and

Meson 1	Meson 2	operators
$\pi(140)[1]$	$\pi(140)[1]$	A_2^- SS1 – A_2^- SS1
$\pi(140)[2]$	$\pi(140)[2]$	A_2^- SS0 – A_2^- SS0
$\overline{K}(497)[1]$	$K(497)[1]$	A_2 SS1 – A_2 SS1
$\pi(140)[3]$	$\pi(140)[3]$	A_2^- SS0 – A_2^- SS0
$\omega(782)[1]$	$\pi(140)[1]$	E^- SS1 – A_2^- SS1
$\overline{K}(497)[2]$	$K(497)[2]$	A_2 SS0 – A_2 SS0
$\pi(140)[4]$	$\pi(140)[4]$	A_2^- SS1 – A_2^- SS1
$h_1(1170)[0]$	$\pi(140)[0]$	T_{1g}^- SS0 – A_{1u}^- SS0
$\omega(782)[2]$	$\pi(140)[2]$	B_1^- SS1 – A_{1u}^- SS0 B_2^- SS1 – A_{1u}^- SS0
$\pi(140)[0]$	$a_1(1260)[0]$	A_{1u}^- SS0 – T_{1g}^- SS0
$\phi(1020)[1]$	$\pi(140)[1]$	E^- SS1 – A_2^- SS1
$\eta(547)[1]$	$\rho(770)[1]$	A_2^+ SS1 – E^+ SS1
$\overline{K}(497)[3]$	$K(497)[3]$	A_2 SS0 – A_2 SS0
$\pi(140)[5]$	$\pi(140)[5]$	A_2^- SS0 – A_2^- SS0
$\overline{K}(497)[1]$	$K^*(892)[1]$	E SS2 – A_2 SS1
$\omega(782)[3]$	$\pi(140)[3]$	E^- SS1 – A_2^- SS0
$\eta(547)[2]$	$\rho(770)[2]$	A_2^+ SS0 – A_2^+ SS1 A_2^+ SS0 – B_2^+ SS2
$h_1(1170)[1]$	$\pi(140)[1]$	E^- SS2 – A_2^- SS1 A_2^- LSD3 – A_2^- SS1
$\overline{K}(497)[4]$	$K(497)[4]$	A_2 SS1 – A_2 SS1
$\pi(140)[2]$	$\phi(1020)[2]$	B_1^- SS1 – A_{1u}^- SS0 B_2^- SS2 – A_{1u}^- SS0
$\pi(140)[6]$	$\pi(140)[6]$	A_2^- SS0 – A_2^- SS0

Table 7.1: Expected two-meson states below 2 GeV in the absence of meson interactions. For each two-meson expected state, an operator is included with the appropriate flavor structure and internal momenta. For isoscalar mesons, such as ϕ, ω, η, and h_1, two operators were added for each level: one operator using only light quarks, and one using strange quarks. The third column lists the irrep and displacements selected. Some states there have multiple irreps possible, and an operator is chosen for each. The number in square brackets indicates the momentum squared, e.g. [2] $\rightarrow \boldsymbol{d}^2 = 2$ or $\boldsymbol{d} = (0, 1, 1)$.

Meson 1	Meson 2	Operators
$\pi(140)[1]$	$a_1(1260)[1]$	A_2^- SS1 – A_2^- SS0
		A_2^- SS1 – E^- SS0
$\overline{K}(497)[2]$	$K^*(892)[2]$	B_1 SS1 – A_2 SS0
		B_2 SS3 – A_2 SS0
$\rho(770)[1]$	$\rho(770)[1]$	A_1^+ SS1 – A_1^+ SS1
		A_1^+ SS1 – E^+ SS1
		E^+ SS1 – E^+ SS1
$\omega(782)[4]$	$\pi(140)[4]$	E^- SS1 – A_2^- SS1
$\eta(547)[3]$	$\rho(770)[3]$	A_2^+ SS0 – E^+ SS1
$\pi(140)[1]$	$\pi(1300)[1]$	A_2^- SS1 – A_2^- TSD0
$\overline{K}(497)[5]$	$K(497)[5]$	A_2^- SS0 – A_2^- SS0
$\pi(140)[1]$	$a_2(1320)[1]$	A_2^- SS1 – E^- TSD1
$\omega(782)[0]$	$a_0(980)[0]$	T_{1u}^- SS0 – A_{1g}^- SS0
$\overline{K}(497)[0]$	$K_1(1270)[0]$	T_{1g} SS0 – A_{1u}^- SS0
$\phi(1020)[3]$	$\pi(140)[3]$	E^- SS1 – A_2^- SS1
$h_1(1170)[2]$	$\pi(140)[2]$	A_2^- SS0 – A_2^- SS0
		B_1^- SS2 – A_2^- SS0
		B_2^- SS0 – A_2^- SS0
$\eta(547)[0]$	$b_1(1235)[0]$	A_{1u}^+ SS0 – T_{1g}^+ SS0
$\pi(140)[1]$	$\pi_1(1400)[1]$	A_2^- SS1 – E^- LSD1
$\rho(770)[2]$	$\rho(770)[2]$	A_1^+ SS2 – A_1^+ SS2
		A_1^+ SS2 – B_1^+ SS1
		A_1^+ SS2 – B_2^+ SS2
$\overline{K}(497)[3]$	$K^*(892)[3]$	E SS1 – A_2 SS0
$\pi(140)[2]$	$a_1(1260)[2]$	A_2^- SS0 – A_2^- SS1
		A_2^- SS0 – B_1^- SS0
		A_2^- SS0 – B_2^- SS0
$\pi(140)$ [2]	$\pi(1300)$ [2]	A_2^- SS1 – A_2^- TSD0

Table 7.2: Expected two-meson states continued.

π [0] A_{1u}^- TDO1	π [0] T_{1g}^- SS0
π [1] A_2^- TSD2	π [1] A_2^- TSD1
π [2] A_2^- SS1	π [2] A_2^- SS0
π [4] A_2^- SS1	π [4] A_2^- TSD0
η [0] T_{1g}^- SD1	π [0] A_{1u}^- SS0
η [3] E^- SD6	π [3] A_2^- SS0
K [1] E SS3	$\overline{K}$ [1] A_2 SS0
K [2] A_2 SS0	$\overline{K}$ [2] A_2 SS1
K [3] A_2 SS0	$\overline{K}$ [3] A_2 SS1

Table 7.3: Additional operators included to get a better signal for some of the lower energy states.

four-meson levels are expected in the energy range we study. The couplings of our operators to such states are expected to be dramatically suppressed by factors proportional to the inverse of the spatial volume. This initial study did not attempt to include three- and four-meson operators, since our main goal was finding the single-meson states.

Once the operator list was determined, a correlator matrix was produced as described in Sec. 6.3. These correlation functions were computed for time separations between $3a_t$ and $25a_t$, inclusively. The matrix was then diagonalized using $\tau_i = 5$ and $\tau_d = 8$, which was sufficiently large for the matrix's off-diagonal elements to be consistent with zero for the ranges of t that the fits were performed as seen in Fig. 7.1. The matrix was ill conditioned, due to some of the single-hadron operators being insufficiently independent one all others, so removal of the eigenvectors corresponding to the noisy directions as described in Sec. 6.3 was applied. Removing just one level resulted in a condition number of ≈ 400.

Fits to the diagonal correlators were carried out to get the spectrum of energies. This was done using the bootstrap method with 1000 bootstrap resamplings. Each sampling was fit using the periodic two-exponential function given in Eq. (6.18), and according to the methodology described in Sec. 6.5.3. The levels were then numbered according to increasing best-fit values of the energies. Many of the correlators with higher energies were noisy, and the energies as well as the error bars increased dramatically after the first 50 levels, corresponding to an energy near 2 GeV. Our operator sets were selected to saturate all single-meson and two-meson levels below 2 GeV, so energies above this chosen cutoff were not seriously considered.

#	$(t_{\min}, t_{\max})$	Fit Energy	χ^2/dof	note
0	5, 25	0.1284(14)	0.8471	ρ
1	7, 25	0.1371(74)	0.7385	$\pi[1] - \pi[1]$
2	5, 25	0.177(11)	1.6523	$\pi[2] - \pi[2]$
3	5, 25	0.208(13)	2.1665	$\eta[1] - \pi[1]$
4	8, 25	0.2084(19)	1.0349	$K[1] - \overline{K}[1]$
5	5, 25	0.238(14)	1.3133	
6	4, 25	0.243(11)	1.3221	$\phi[3] - \pi[3]$
7	5, 25	0.249(10)	1.2780	$\phi[1] - \pi[1]$
8	3, 25	0.2497(40)	1.9590	$K[2] - \overline{K}[2]$
9	3, 23	0.253(12)	1.0498	$\pi[0] - \pi[0]$
10	3, 25	0.2713(10)	1.7219	
11	4, 23	0.276(20)	1.5506	
12	4, 25	0.2793(99)	0.7780	
13	5, 25	0.2852(39)	1.3607	$\phi[2] - \pi[2]$
14	3, 25	0.2875(61)	2.1628	$K[3] - \overline{K}[3]$
15	4, 23	0.288(19)	1.4598	$K[2] - \overline{K}[2]$
16	4, 25	0.2890(72)	1.6656	
17	3, 23	0.2918(62)	1.4153	
18	3, 25	0.2943(75)	2.2117	$K[1] - \overline{K}[1]$
19	3, 25	0.2977(78)	1.3868	$q\overline{q}$
20	4, 23	0.2982(75)	2.3735	
21	3, 25	0.299(11)	1.2518	
22	3, 25	0.3003(96)	1.2973	
23	3, 25	0.3053(68)	1.6659	
24	3, 25	0.305(10)	0.8332	

Table 7.4: The results of periodic two-exponential fits to the first 25 the diagonal levels. The note on certain levels indicates that a particular operator has overlaps with only a single level. If that is the case the flavor and internal momentum of the operator is listed.

The diagonal correlators for the 50 low-lying levels are displayed in Figs. 7.2 and 7.3, with the fit function plotted as a dashed line. The effective masses (eq. 6.1) corresponding to these correlators are shown in Figs. 7.4 and 7.5. These plots include the effective mass of the fit function, and a band indicating the value and standard deviation of the fitted mass parameter.

#	$(t_{\min}, t_{\max})$	Fit Energy	χ^2/dof	notes
25	4, 25	0.3066(59)	0.8744	$\phi[3] - \pi[3]$
26	3, 23	0.3094(51)	2.1435	
27	4, 21	0.310(24)	1.1783	$q\overline{q}$
28	3, 25	0.3114(91)	1.2336	
29	3, 25	0.313(20)	1.6611	
30	3, 22	0.3138(85)	1.1806	$q\overline{q}$
31	4, 24	0.317(18)	0.8966	$\pi[2] - \pi[2]$
32	5, 25	0.317(14)	0.8218	
33	5, 22	0.323(15)	1.2148	
34	4, 24	0.324(13)	0.4844	
35	4, 25	0.3254(83)	1.2818	
36	5, 25	0.3274(50)	0.8198	$\phi[2] - \pi[2]$
37	3, 22	0.3274(89)	1.0671	
38	3, 25	0.328(13)	1.9359	$K[0] - \overline{K}[0]$
39	3, 24	0.3286(80)	0.9472	
40	3, 22	0.330(10)	1.0911	$q\overline{q}$
41	3, 22	0.333(23)	2.0288	
42	4, 25	0.3340(82)	1.0978	
43	4, 25	0.336(13)	0.4344	
44	3, 21	0.3361(88)	0.8062	
45	3, 23	0.3405(88)	0.7079	
46	4, 23	0.3490(86)	1.5028	
47	3, 19	0.353(19)	1.7727	
48	3, 24	0.3607(64)	1.1605	$\phi[2] - \pi[2]$
49	3, 15	0.378(39)	1.6047	$q\overline{q}$

Table 7.5: The results of periodic two-exponential fits to diagonal levels 25-49.

7.2.2 Level Identification

Ideally, one would like to identify which of the stationary energy levels correspond to single hadron resonances, and which are two-particle states. However, this is difficult as we are simulating a fully interacting theory in a finite volume, and the stationary states are not likely to be exact one-meson or two-meson states. Additionally, most of our operators have overlaps with many states. In fact, if operators only coupled to a certain set of states, there would be no need to include multi-hadron operators to extract the spectrum of excited mesons, as single hadron operators would be sufficient.

The correlators between operators with different internal flavor structure and momenta are usually small. If these cross correlators were exactly zero, we could classify

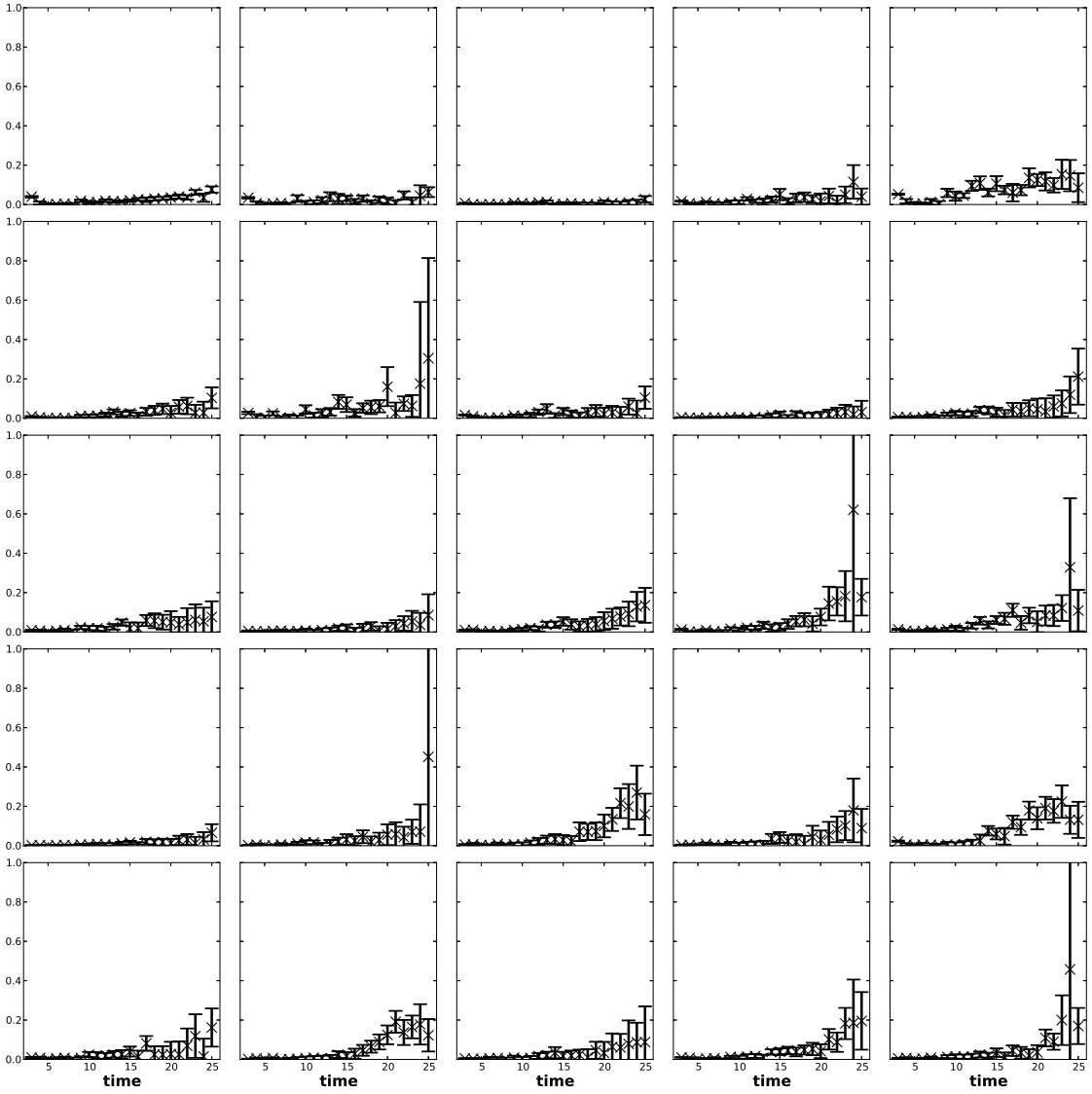

Figure 7.1: The off-diagonal correlators for the matrix after variational improvement for the lowest energy state with the first 25 states performing diagonalization at $\tau_i = 5$ and $\tau_d = 8$.

each lattice state as an excited meson, a $\pi - \pi$ state, a $K - \overline{K}$ state, etc, depending on which type of operator overlapped with that state. We do observe mixing, so a strict identification is not possible. In some cases, an operator will overlap significantly with only a single state, in which case, identifying that particular state with the features of the creating operator is reasonable. When an operator only overlaps with a single state, the identification is listed in Tables 7.4-7.5. In most cases, operators overlap

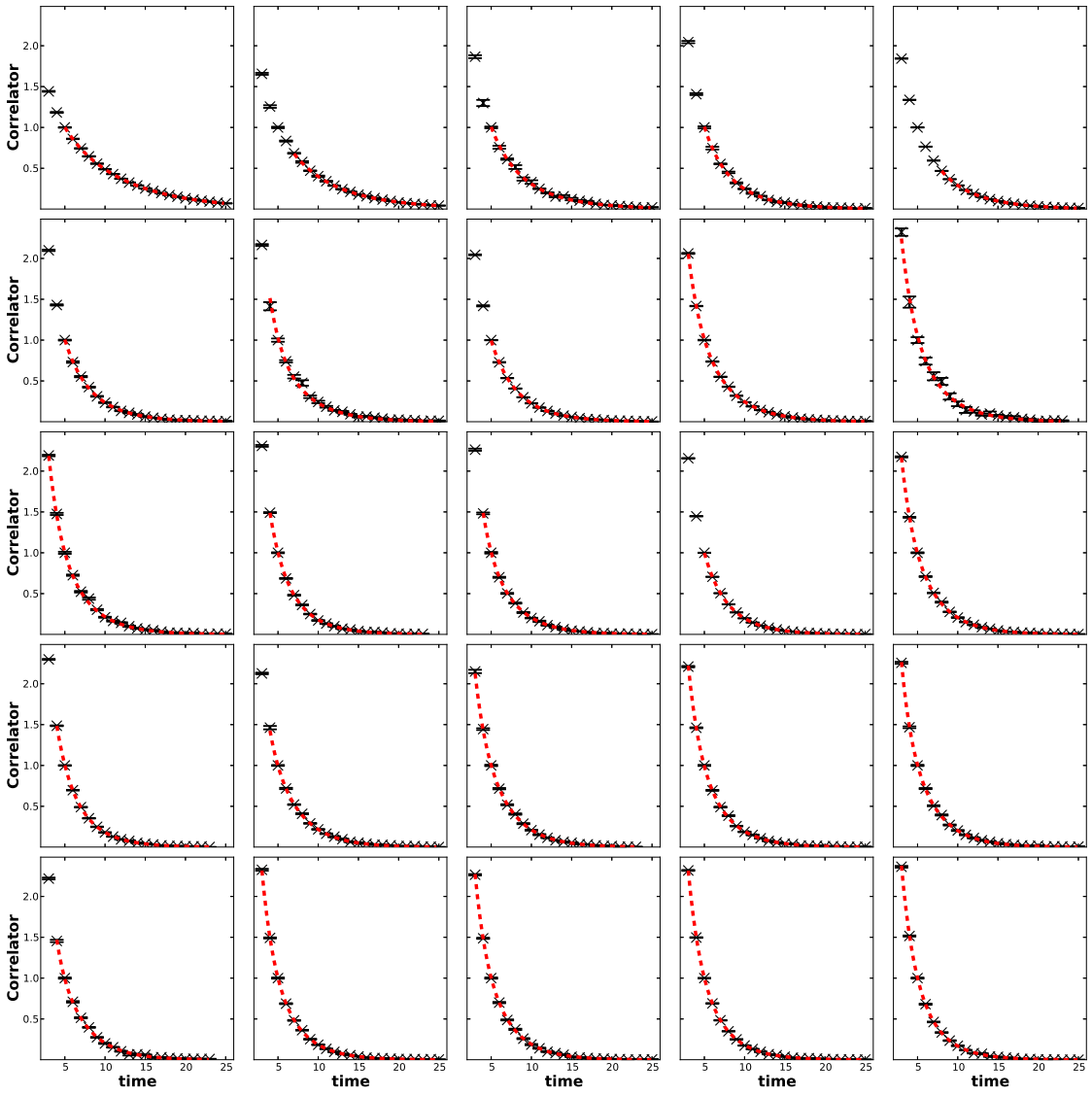

Figure 7.2: The first 25 diagonal correlators of the rotated correlator matrix for the T_{1u}^{+} channel. The dashed line indicates the best fit of the function in Eq. (6.18).

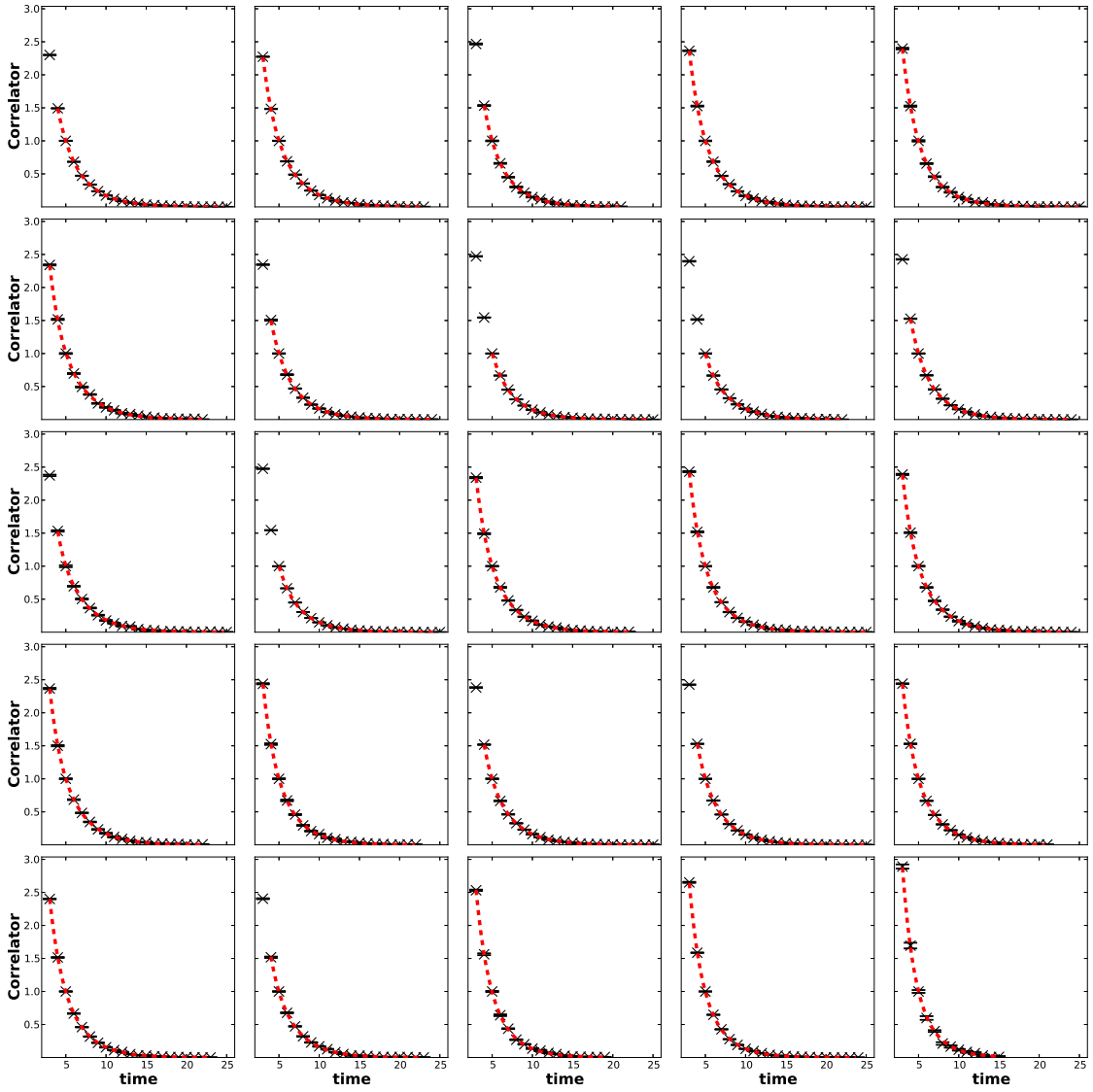

Figure 7.3: The diagonal correlators 25-49 of the rotated correlator matrix for the T_{1u}^{+} channel. The dashed line indicates the best fit of the function in Eq. (6.18).

significantly with more than one state. This can be seen in Fig. 7.6, which compares the overlaps of two single-hadron operators of different displacements. One operator has overlaps which are overwhelmingly dominated by a single state, while the other couples to many of the stationary states.

Our main goal here is to determine the pattern of energies corresponding to quark-antiquark resonances in infinite volume. To accomplish this, we first inspect a matrix built of the subset of operators including only the single hadron $q\overline{q}$ operators. This

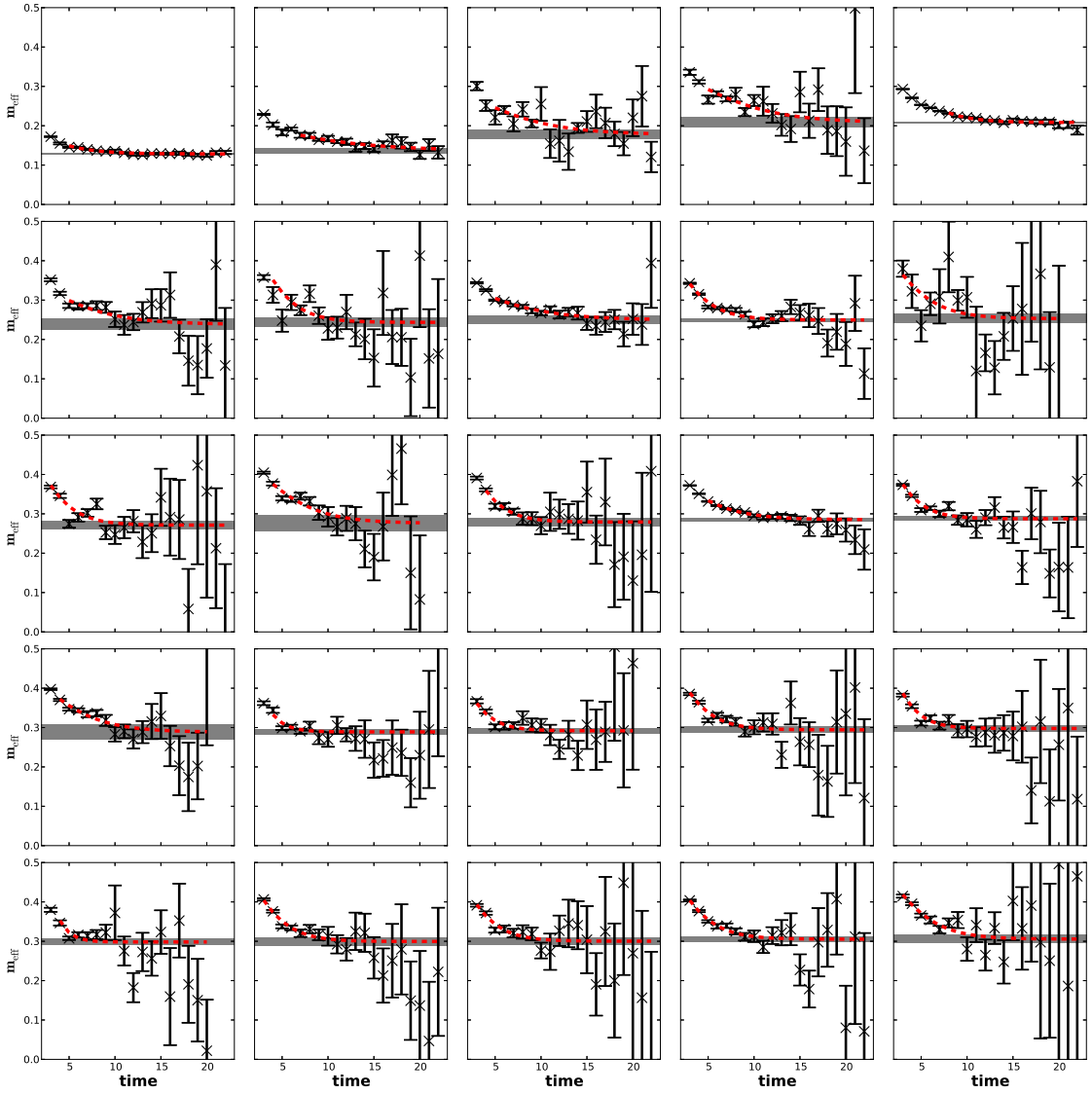

Figure 7.4: Effective masses using $\Delta t = 3$ of the correlators displayed in Fig. 7.2. The dashed line is the effective mass of the fit function. The gray band shows the standard deviation in the best fit value of the mass parameter.

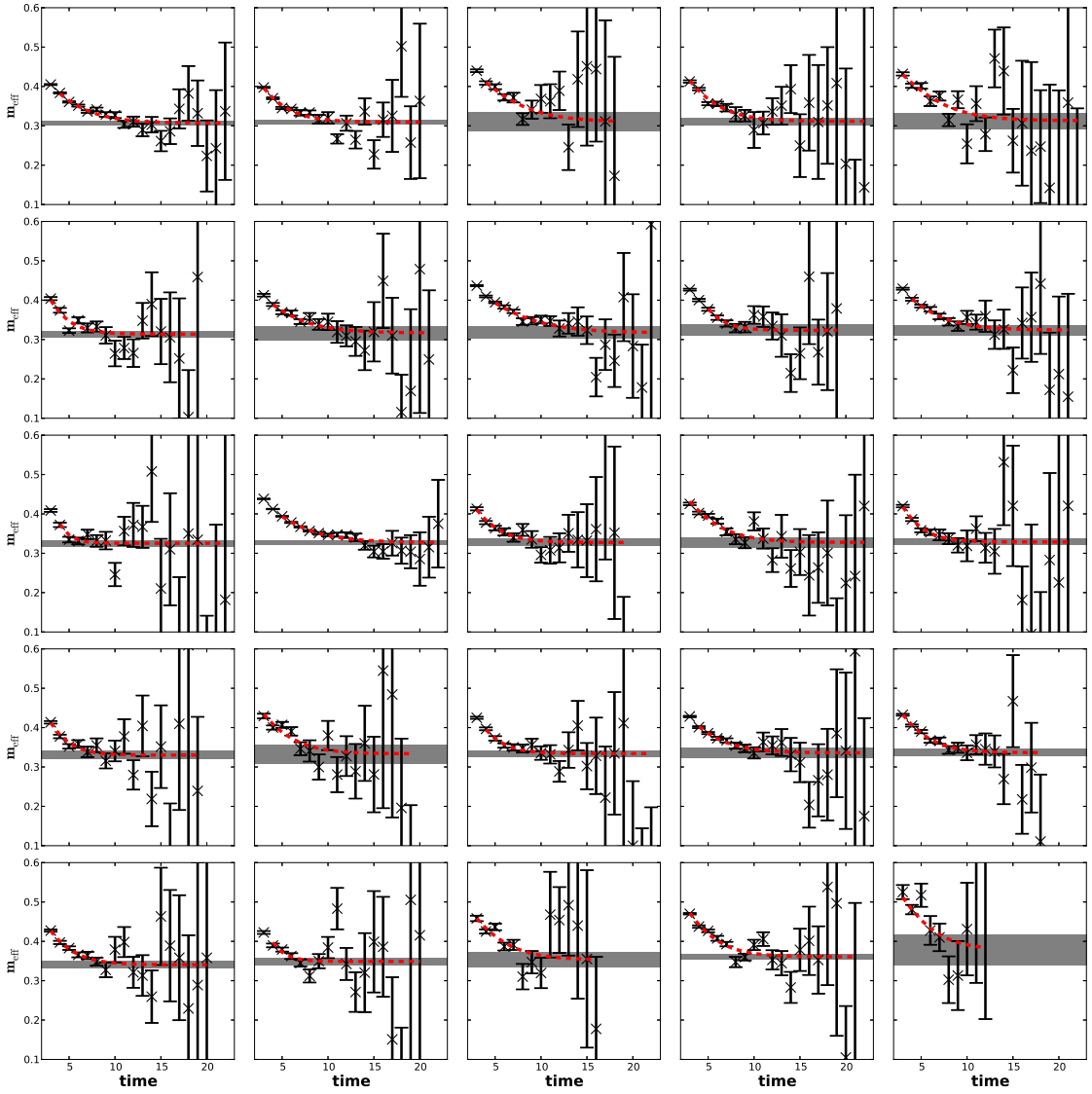

Figure 7.5: Effective masses using $\Delta t = 3$ of the correlators displayed in Fig. 7.3. The dashed line is the effective mass of the fit function. The gray band shows the standard deviation in the best fit value of the mass parameter.

matrix is diagonalized to find linear combinations which are orthogonal to get the spectrum if only these operators were included. These linear combinations of operators we refer to as "optimized" single-hadron operators. We then look at the overlaps of these operators with the stationary states determined by the entire correlation matrix. The overlaps with the optimized linear combinations are shown in Fig. 7.7. In all cases, either one level or a handful of levels have significant overlaps, and in

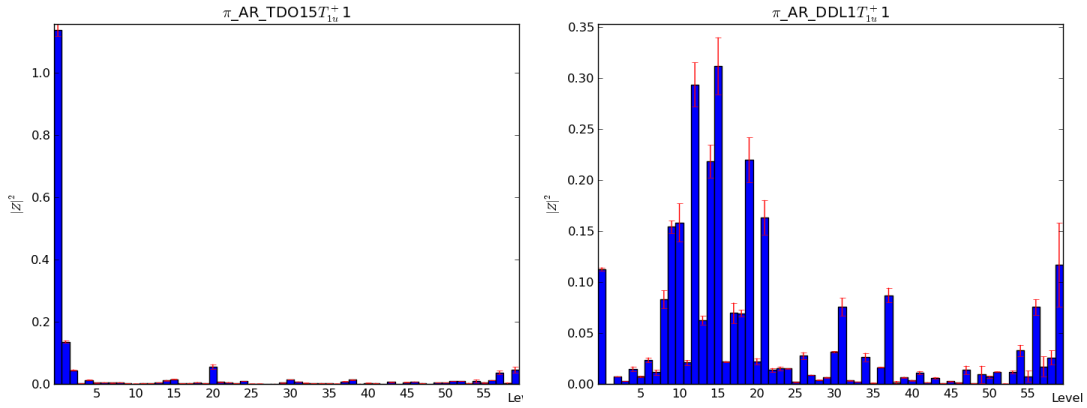

(a) TDO1 (b) DDL1

Figure 7.6: Overlaps $|Z_j^n|^2$ for hadron operators j with displacement TDO (left) and DDL (right) with the levels n. The TDO operator is dominated by a single state while the DDL operator has significant coupling to several levels.

cases where there are several large overlaps, the energies of those levels are all the same within errors. Hence, we can use the energy of these levels of largest overlaps as a qualitative estimate of the quark-antiquark resonance energies.

The energies of all states are plotted in Fig. 7.8, which we affectionately refer to as a *staircase* plot, with indicators of which states are dominated by single hadron operators. For each of the optimized linear combinations of the single-hadron operators, the state which has the largest overlap is marked in dark blue indicating a $q\overline{q}$ state. To indicate that some of the combinations do not couple to only a single state, states which have overlaps $>75\%$ of the largest are outlined in dark blue, indicating significant mixing with our $q\overline{q}$ operators.

This spectrum of $q\overline{q}$ states agrees with the findings in reference [44] which used similar analysis on a $24^3 \times 128$ lattice with pion mass of 390MeV. His results also indicate five $q\overline{q}$ states below 2GeV with the lightest state being much lighter than the other four. Comparison of two particle states is not useful as the allowed momenta do not match on the different lattices. The extraction of 50 energy levels by including two-hadron operators is unprecedented and there are no other results for comparison.

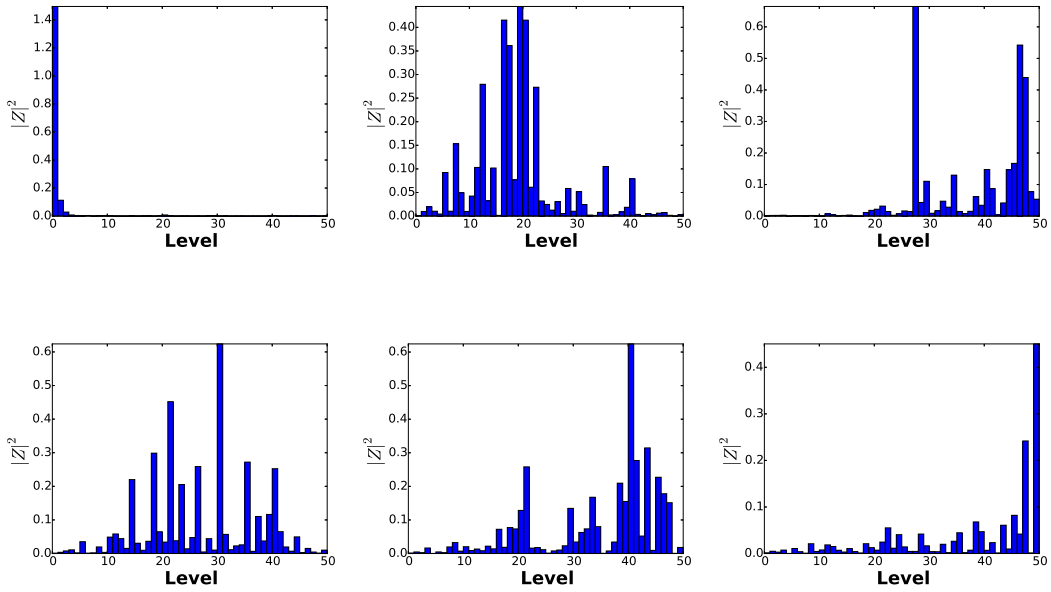

Figure 7.7: Overlap $|Z_j^n|^2$ of each of the "optimized" single-hadron operators j with levels n.

7.2.3 Comparing to Experiment

The energies in our calculations are determined in terms of the temporal lattice spacing a_t, but energy ratios are well defined and can be compared directly with experiment. The mass of the kaon is a convenient reference energy. We present our results as ratios with the kaon rest mass, which occurs as the lightest state in the A_{1u} channel with zero total momentum and strangeness $S = 1$. Two exponential fits to this state yield a measurement of $a_t m_K = 0.083538 \pm 0.00015$ for the kaon mass. The experimental value for the kaon mass was taken from the PDG[46] average of the K^+ and K^0 as 495.6MeV.

The T_1 channel in a cubic volume contains states in the continuum with spins 1, 3, 4, 5, and so on. The relevant experimental resonances which should show up in the T_{1u}^+ channel below $\approx$ 2GeV are the spin-1 ρ, $\rho(1450)$, $\rho(1570)$, $\rho(1700)$, $\rho(2150)$; and spin-3 $\rho_3(1690)$, $\rho_3(1990)$. Most of these states have large widths, on the order of 100 MeV. A comparison of the experimental spectrum with our finite-volume results is shown in Fig. 7.9. The energies shown on the right-hand side of this figure are the same as the dark blue results in Fig. 7.8.

Fig. 7.9 compares our results with experiment. Note that our results are believed to be quark-antiquark excitations, identified as previously described. Since our ener-

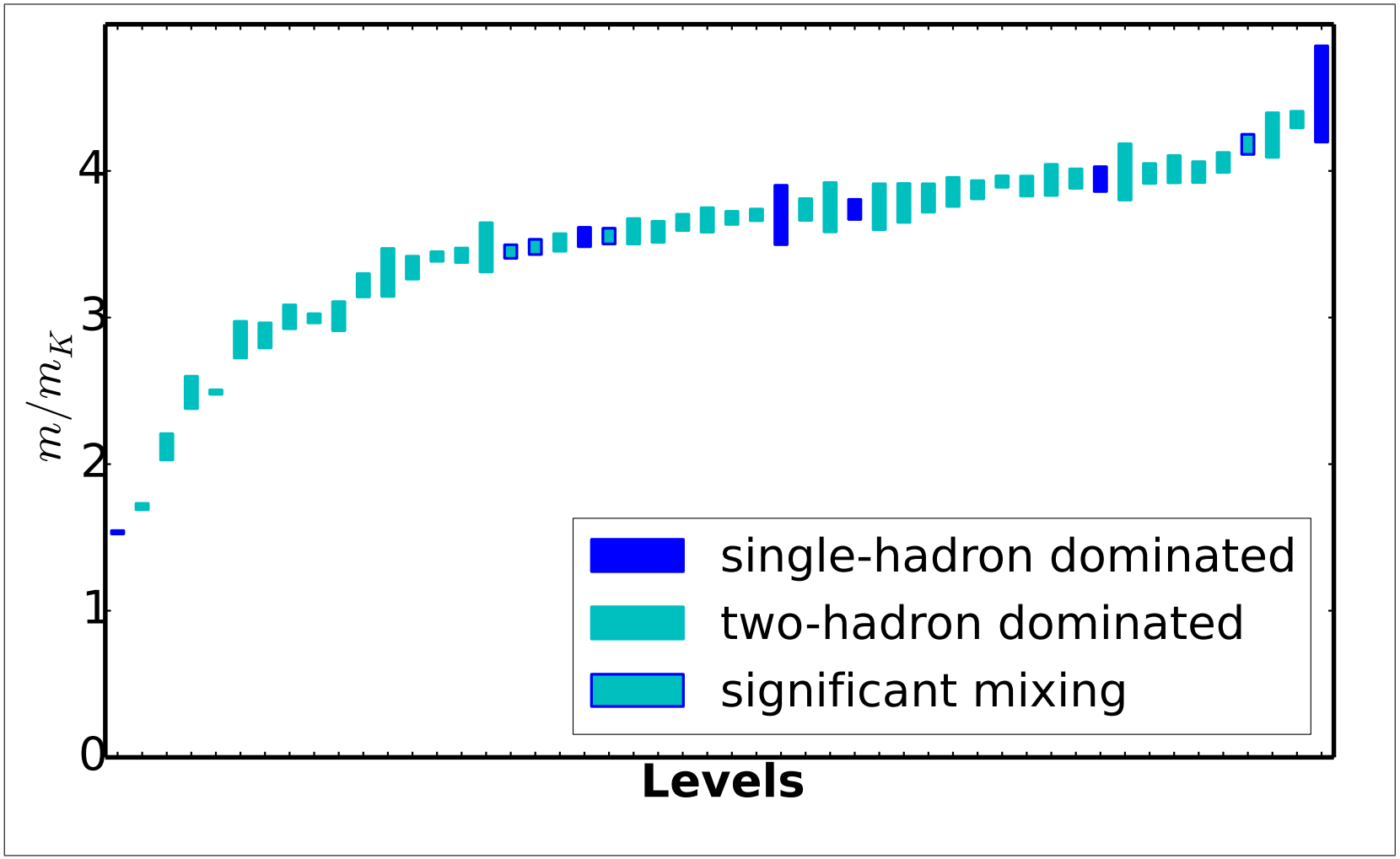

Figure 7.8: Spectrum of the first 50 states excited by our single- and two-hadron operators in the T_{1u}^+ channel. For each optimized single-hadron operator, the level of maximum overlap is indicated by dark blue, and levels with overlaps $> 75\%$ of the largest are indicated by a dark blue outline.

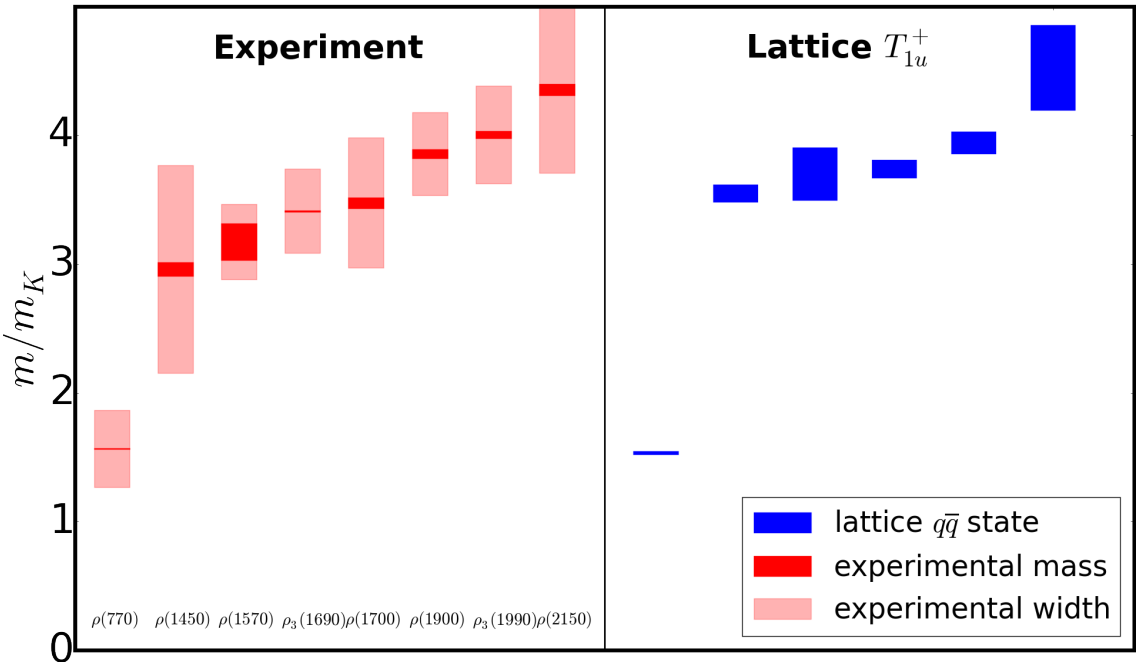

Figure 7.9: Comparison of the experimental spectrum of resonances with our finite-volume energies corresponding to quark-antiquark excitations. In the left hand side of the figure, dark red boxes indicate the experimental masses, with the vertical heights showing the uncertainties in the mass measurements. The light red boxes indicate the experimental widths of the resonances. In the right hand side, our results are shown by dark blue boxes, whose heights indicate statistical uncertainties only. The experimental results include both ρ (spin 1) and ρ_3 (spin 3) states.

gies are determined in finite volume, we can expect agreement with experiment only within the widths of the corresponding infinite-volume resonances. Such agreement is observed, without exception. We do not find any quark-antiquark excitations at energies where experiment observes nothing. However, experiment observes more resonances than indicated by our calculations. First, some of the experimental determinations are still controversial. Secondly, our current analysis can only identify quark-antiquark excitations. Resonances that do not correspond to quark-antiquark excitations, such as meson-meson "molecular" type states, have to be identified with the scattering phase shift techniques described later. The analysis of this spectrum is not yet finished. In the future, we will examine the spin structure of our levels, as well as the dominant two-meson mixing modes, which should help us identify the correspondences between our levels and the experimental resonances.

7.3 The Width of the ρ Resonance

Chapter 5 presented a method of determining scattering phase shifts in the continuum from the energies of stationary states in finite volume. In this section, we look at the spectrum of energies in channels which have zero and nonzero total momentum in which the ρ meson appears. We compute the P-wave $\pi\pi$ scattering phase shifts from these energies, and then deduce the mass and width of the ρ resonance.

7.3.1 $\pi\pi$ $I = 1$ Energies

At rest, the spin 1, positive G-parity ρ meson appears in the T_{1u}^+ channel, but for nonzero total momenta, we must use Table 3.2 to see which little groups will contain the ρ. We can see that the ρ will appear in irreps A_1^+ and E^+ of C_{4v} for on-axis momenta, in the A_1^+, B_1^+ and B_2^+ irreps of C_{2v} for planar-diagonal momenta, and A_1^+ and E^+ irreps of C_{3v} for cubic-diagonal momenta. The spectrum of energies from each of these channels can be used to compute the $I = 1$ $\pi\pi$ P-wave scattering phase shift, and hence, determine the mass and width of the ρ resonance.

In determining the $\pi\pi$ scattering phase shifts, only energy levels below the inelastic thresholds can be used. In each of the above channels, we need to include enough two-pion operators of different individual momenta to get a good signal for all states below such thresholds. Operator selection is again done as previously described, using the expected energies in the absence of interactions as a guide. Using the single-hadron energies and the momenta allowed on our 32^3 lattice, there are between one and four pion-pion states which are expected to be below inelastic thresholds in the above channels. The thresholds in these channels are two-meson states which are either a $\overline{K} - K$ state or a $\pi - \omega$. Two-pion operators were included to couple to the expected two-meson states for the expected levels up to the inelastic threshold.

For each of the channels, a correlator matrix was produced and diagonalized. The correlation functions for these channels were produced for time separations of $3a_t$ to $38a_t$. The time extent was chosen larger than used in the previous section due to the lower energies involved and the need for greater accuracy here. The correlator matrices encountered were all well conditioned, and diagonalizations were performed using $\tau_i = 5$, $\tau_d = 8$, which was sufficient for the off-diagonal elements to be consistent with zero. The energies determined for the levels below threshold in each of the channels are given in Tables 7.6-7.9. Each channel has between 1 and 5 levels with

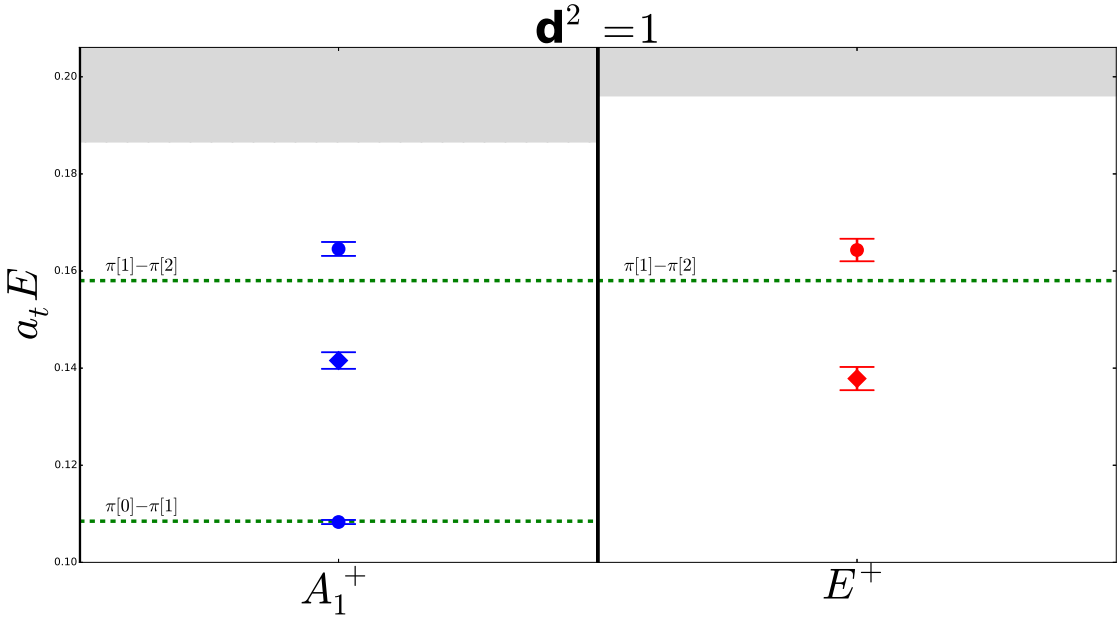

Figure 7.10: Energies of $\pi\pi$ states with $\boldsymbol{d}^2 = 1$. Dashed lines indicate the non-interacting energies of allowed $\pi\pi$ states. The shaded region indicates the inelastic thresholds. Diamond markers indicate levels with large overlaps with the $q\bar{q}$ ρ operator.

energies below the inelastic thresholds. Figs. 7.10-7.13 display the energies for the levels, along with the energies of allowed $\pi\pi$ states in the absence of meson-meson interactions. The non-interacting energies plotted come from summing the energies of the individual pions from Table 7.10.

Irrep	Level	$(t_{\text{min}}, t_{\text{max}})$	Fit Energy	χ^2/dof
A_1^+	0	7, 38	0.10831(43)	0.6539
A_1^+	1	7, 38	0.1416(17)	0.6373
A_1^+	2	7, 38	0.1632(16)	1.3688
E^+	0	8, 38	0.1378(24)	0.8939
E^+	1	7, 38	0.1643(23)	1.1575

Table 7.6: The fitted energies for $I = 1$ $\pi\pi$ with $\boldsymbol{d}^2 = 1$.

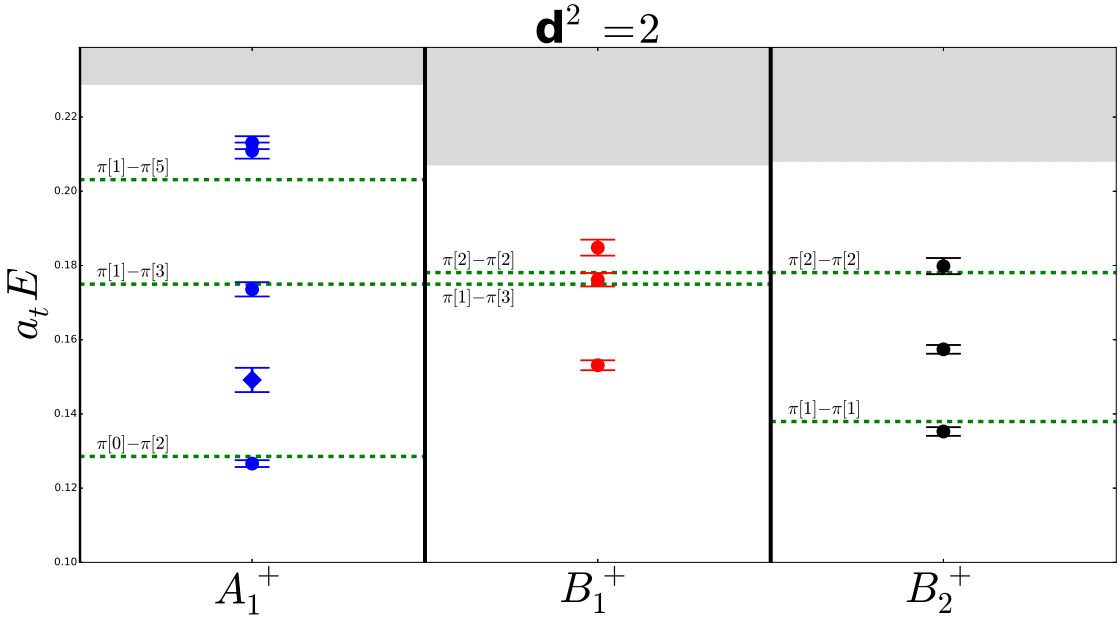

Figure 7.11: Energies of $\pi\pi$ states with $\boldsymbol{d}^2 = 2$. Dashed lines indicate the non-interacting energies of allowed $\pi\pi$ states. The shaded region indicates the inelastic thresholds. Diamond markers indicate levels with large overlaps with the $q\bar{q}$ ρ operator.

Irrep	Level	$(t_{\min}, t_{\max})$	Fit Energy	χ^2/dof
A_1^+	0	9, 38	0.12661(91)	0.8932
A_1^+	1	9, 38	0.1492(32)	1.8102
A_1^+	2	7, 38	0.1735(19)	1.0632
A_1^+	3	5, 38	0.2109(22)	0.9061
A_1^+	4	4, 38	0.2131(7)	1.1036
B_1^+	0	6, 38	0.1531(13)	1.2569
B_1^+	1	7, 38	0.1761(18)	0.8562
B_1^+	2	7, 38	0.1848(22)	1.4645
B_2^+	0	8, 38	0.1353(12)	0.8600
B_2^+	1	6, 38	0.1574(12)	0.9689
B_2^+	2	7, 38	0.1798(22)	1.0992

Table 7.7: The fitted energies for $I = 1$ $\pi\pi$ with $\boldsymbol{d}^2 = 2$.

7.3.2 Measurement of the Anisotropy

To compute the scattering phase-shifts using the energies for nonzero total momenta, transformation to the center-of-mass frame is required. Since we are using

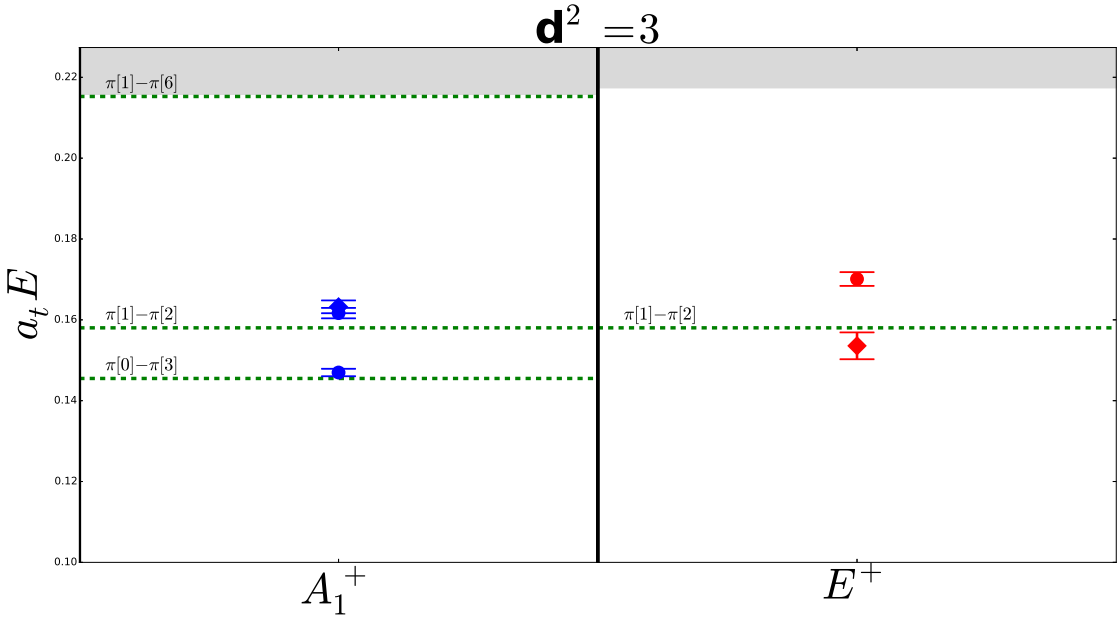

Figure 7.12: Energies of $\pi\pi$ states with $\boldsymbol{d}^2 = 3$. Dashed lines indicate the non-interacting energies of allowed $\pi\pi$ states. The shaded region indicates the inelastic thresholds. Diamond markers indicate levels with large overlaps with the $q\bar{q}$ ρ operator.

Irrep	Level	$(t_{\min}, t_{\max})$	Fit Energy	χ^2/dof
A_1^+	0	5, 38	0.14697(93)	1.3660
A_1^+	1	7, 38	0.1616(13)	1.3692
A_1^+	2	5, 38	0.1632(16)	0.8673
E^+	0	9, 38	0.1536(33)	0.6078
E^+	1	5, 38	0.1701(17)	0.9030

Table 7.8: The fitted energies for $I = 1$ $\pi\pi$ with $\boldsymbol{d}^2 = 3$.

an anisotropic lattice, energies are measured in terms of the temporal spacing a_t, while the momenta are in terms of the larger spatial spacing a_s. This means changing frames requires a precise knowledge of the renormalized anisotropy $\xi = a_s/a_t$.

One way to determine the anisotropy is using the dispersion relation of a particle with various momenta. The energy of a free particle with momentum $\boldsymbol{P} = (2\pi/L)\boldsymbol{d}$ is given by

$$(a_t E_{\boldsymbol{d}})^2 = (a_t m)^2 + \frac{1}{\xi^2}\left(\frac{2\pi}{L/a_s}\right)^2 \boldsymbol{d}^2. \tag{7.1}$$

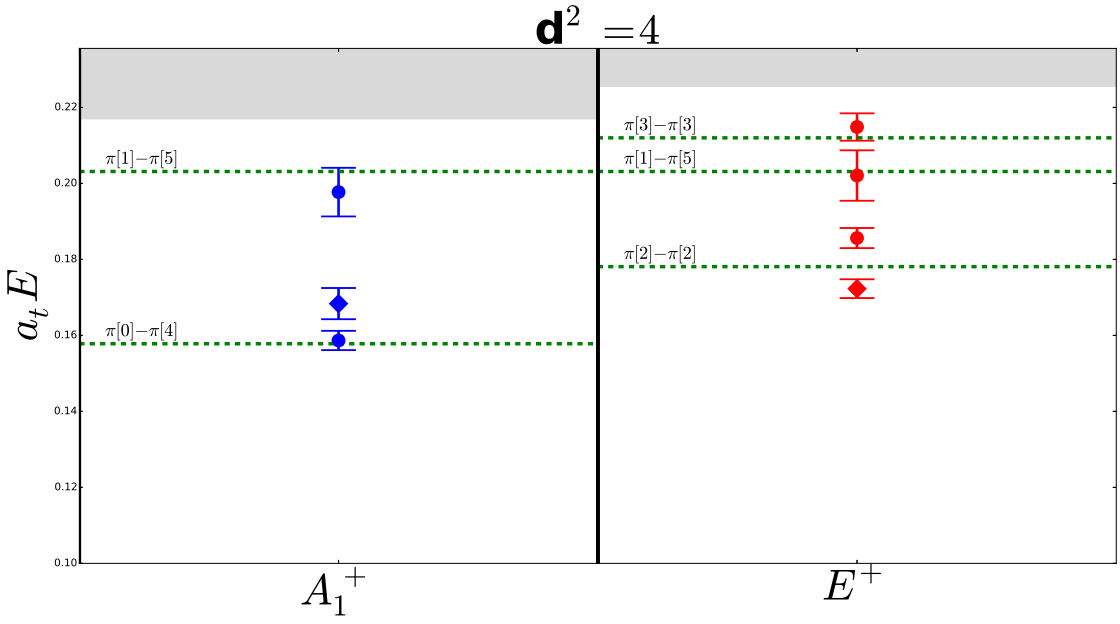

Figure 7.13: Energies of $\pi\pi$ states with $\boldsymbol{d}^2 = 4$. Dashed lines indicate the non-interacting energies of allowed $\pi\pi$ states. The shaded region indicates the inelastic thresholds. Diamond markers indicates levels with large overlaps with the $q\bar{q}$ ρ operator.

Irrep	Level	$(t_{\text{min}}, t_{\text{max}})$	Fit Energy	χ^2/dof
A_1^+	0	6, 38	0.1587(26)	1.1336
A_1^+	1	4, 38	0.0.1737(18)	0.8538
A_1^+	2	6, 36	0.2044(49)	1.364
E^+	0	5, 38	0.1723(25)	1.1061
E^+	1	7, 38	0.1856(26)	0.9369
E^+	2	6, 38	0.2021(66)	1.3147
E^+	3	5, 35	0.2148(36)	1.3647

Table 7.9: The fitted energies for $I = 1$ $\pi\pi$ with $\boldsymbol{d}^2 = 4$.

So by evaluating the energies of a particle with different momenta, ξ can be determined.

Table 7.10 shows the energies for pions at 8 different momenta, which are plotted in Fig. 7.14. These were determined by two-exponential fits to a correlator of just a single operator with itself for many different momenta. The parameter ξ was fit using a standard least squares fit on each bootstrap resampling. The average fit value of ξ in the function in Eq. (7.1) is shown in Fig. 7.15. The anisotropy was computed

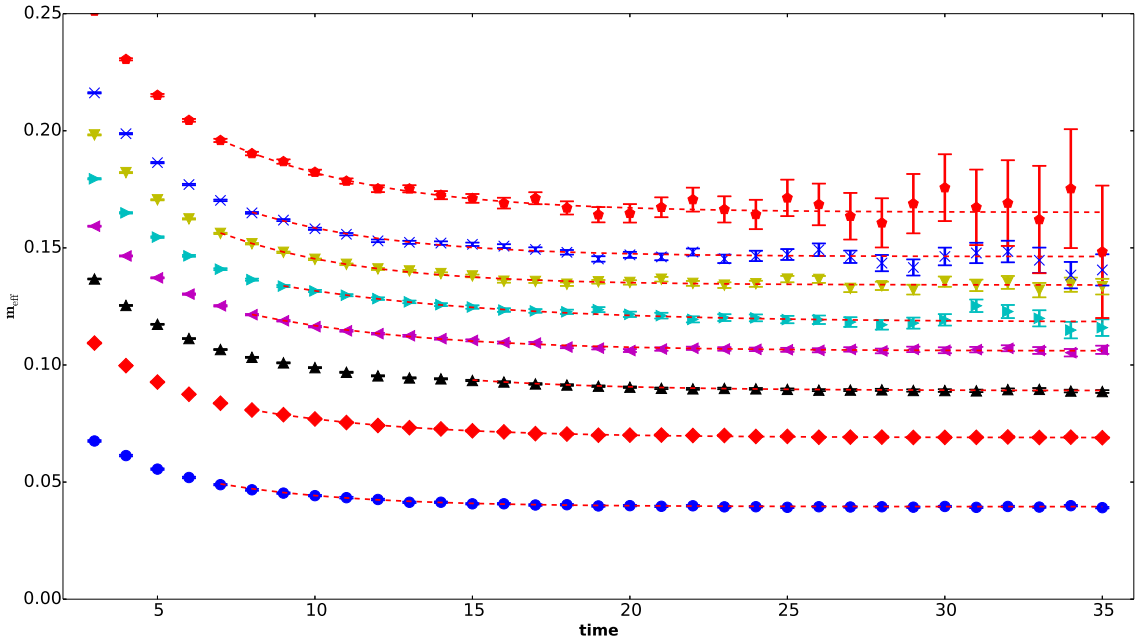

Figure 7.14: Effective masses for pion correlators corresponding to various momenta. From bottom to top, $\boldsymbol{d}^2 = 0, 1, 2, 3, 4, 5, 6, 8$. Dashed lines show two-exponential best-fit results, without errors.

separately on each bootstrap sample, so it may be used in computing the scattering phase shift independently for each bootstrap.

$\boldsymbol{d}^2$	Fit Energy	χ^2/dof
0	0.03950(20)	0.9342
1	0.06898(21)	0.8441
2	0.08904(44)	0.8927
3	0.10599(63)	1.1042
4	0.1183(16)	1.0125
5	0.13415(65)	1.2313
6	0.1463(11)	1.2460
8	0.1652(26)	0.5999

Table 7.10: Fit values for pion energies for various $\boldsymbol{d}^2$.

7.3.3 Scattering Phase Shift Results

For each of the energies displayed in Tables 7.6-7.9, as well as the lowest three states from the results at rest in Table 7.4, the δ_1 phase shift was computed using the

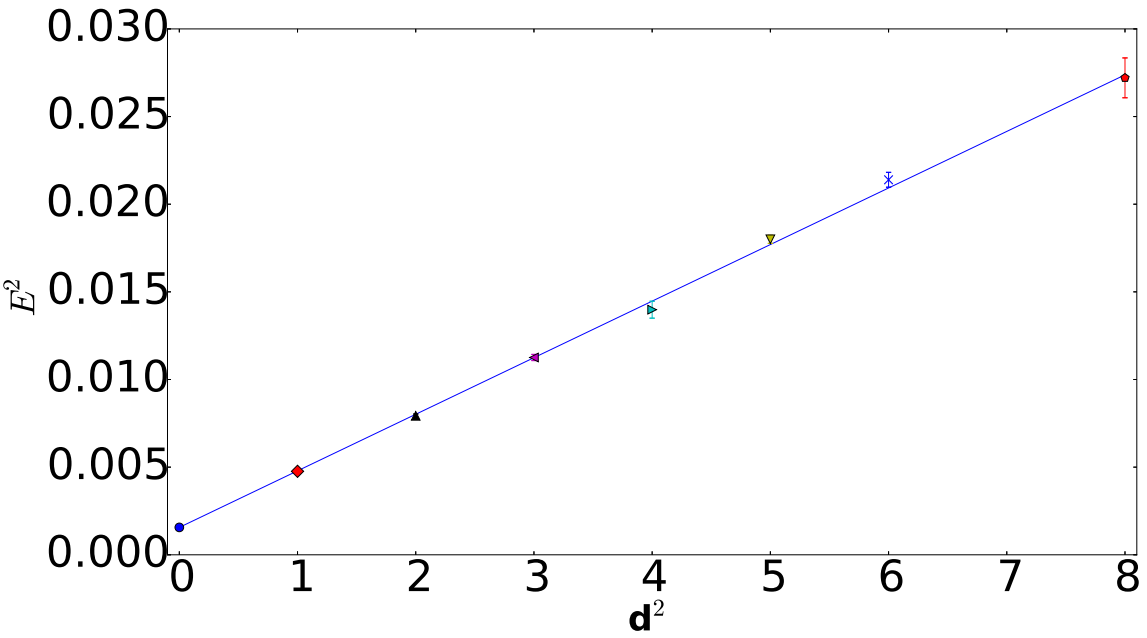

Figure 7.15: Plot of the pion energies squared against $\boldsymbol{d}^2$. Fitting this to a straight line yields $\xi = a_s/a_t$.

formulas given in Table 5.5. The phase shift requires not only the energy of the particular state, but also the mass of the pion at rest and the renormalized anisotropy ξ to convert to the energies in the center of mass frame. This was done separately for each bootstrap resampling to estimate the error in the phase shift.

The formulas in Table 5.5 yield $\cot \delta_1$, which means that care with respect to quadrant must be taken when determining δ_1 for measurements on different bootstraps. The prescription taken here was to take the median value of δ_1 and shift the value on each bootstrap sample by π to be within $\pm\pi/2$ of the median value. If the state is very close to the non-interacting state, the phase shift may jump between values close to 0 or close π for different bootstrap samples. When considering such cases, we shift by π those below resonance to be ≈ 0, and those above the resonance are shifted to be $\approx \pi$. This shifting is done only for measurements whose estimates are within a standard deviation of either 0 or π The results of the phase shifts for each of the energy levels are plotted in Fig. 7.16, showing the medians and standard deviations for the values of E_{cm} and δ_1 in degrees for each input level. The data points use color to indicate the momentum squared of the state used and point shape to indicate the irrep.

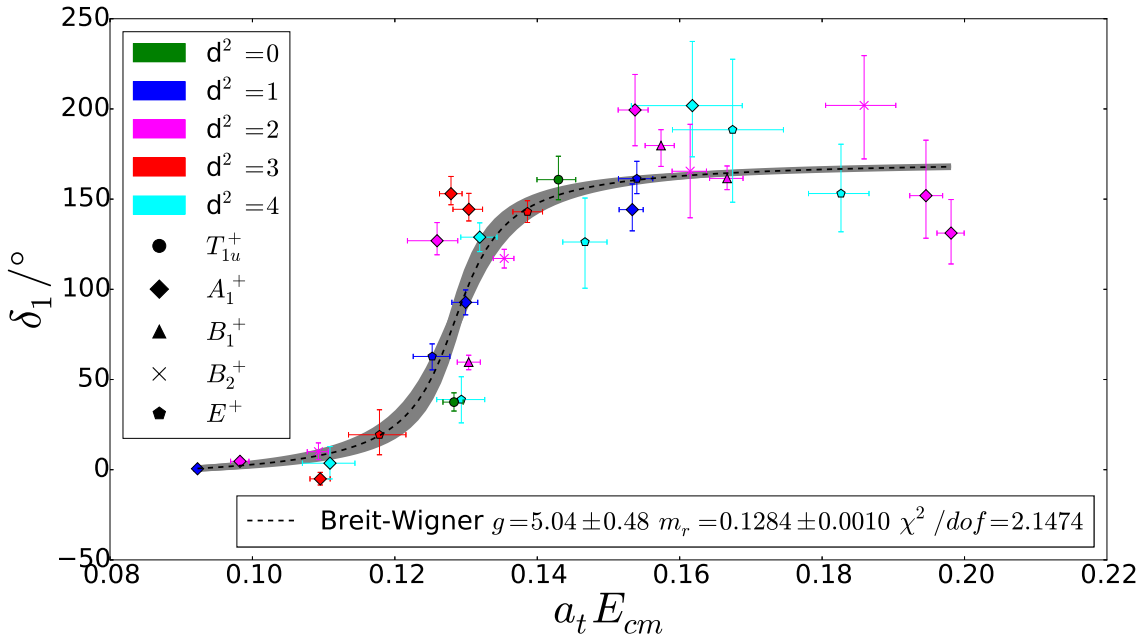

Figure 7.16: Values for the P-wave phase shift δ_1 from each of the energy levels. The color indicates the momentum squared of the level used, while the shape indicates the irrep. Points which overlap 0° or 180° within error are shifted by ±180, as explained in the text. The dashed line indicates the best fit to a Breit-Wigner with the gray band indicating the bootstrap errors in the fit function.

One can determine the location, m_r, and width, Γ, of the resonance by fitting the phase shifts to a Breit-Wigner form

$$\tan(\delta_1) = \frac{\Gamma/2}{m_r - E} + A. \tag{7.2}$$

However the width can be parameterized in terms of a coupling constant, g,

$$g = \sqrt{\frac{6\pi\Gamma m_r^2}{\left(\frac{m_r^2}{4} - m_\pi^2\right)^{3/2}}} \tag{7.3}$$

which should be independent of the quark mass [47, 48]. This function is then fit by minimizing the χ^2 to determine the parameters m_r and Γ on each bootstrap. The median value and standard deviation of the fits on each bootstrap results in

$$m_r = 0.1284 \pm 0.0010 \quad \text{and} \quad g = 5.04 \pm 0.48. \tag{7.4}$$

the value of g is consistent with results utilizing [49] smaller lattice and heavier pion masses.

The location of the resonance is consistent with the value obtained from the spectrum of states in a finite box for channel of T_{1u}^{+} in Sec. 7.2, which had a value for the lowest energy level of 0.1284 ± 0.0014. Again, by taking the ratio with respect to the kaon mass and using the experimental value of the kaon mass to convert to physical units, this sets the resonance location to $m_r = 761.8 \pm 6.2\text{MeV}$ with a width of $\Gamma = 63 \pm 12\text{MeV}$, which compares to the experimental values of $m_\rho^{\text{exp}} = 775.26 \pm 0.25\text{MeV}$ and $\Gamma^{\text{exp}} = 149.1 \pm 0.8\text{MeV}$. The value of Γ may be lower due to a reduced phase space of decay resulting from a heavier pion.

7.3.4 Comparison with Other Works

This section will compare the results of section with results for the $I = 1$ $\pi\pi$ phase shift by other lattice groups [47–52]. Past results have been done using heavier pions masses and smaller volumes. A comparison of previous results to those from this work are shown in Figure 7.17. Each color represents results from one or more lattices from other collaborations and the experimental values taken from the PDG [**PDF2013**] plotted in black for comparison. The horizontal location of each data points indicates the pion mass used by each collaboration. The different pion masses used by each calculation has a noticeable effect on the energy of the resonance and as calculations at higher pion mass produce results with a larger energy. It should be noted that the scale setting procedure is not consistent for each of these results so comparing energies directly should be done with caution. On the other hand the value of the $\rho \to \pi\pi$ coupling, g, should be independent of the pion mass and past results are distributed on either side of the experimental value.

The lattice parameters used in other works are compared in Table 7.11. This work utilized the largest lattice and lightest pion mass to date. The heavier pion mass from previous results means fewer $\pi\pi$ states are below the inelastic threshold and fewer finite-volume energies are available. Additionally many collaborations did calculations on a smaller set of total momentum. From reference [47] the phase shift was computed using only two stationary-state lattice energies on a coarse $12^3 \times 24$ lattice in 2007. The ETMC collaboration [48] computed the phase shift using six energies from four different lattices each with a different pion mass. Their results are plotted as four

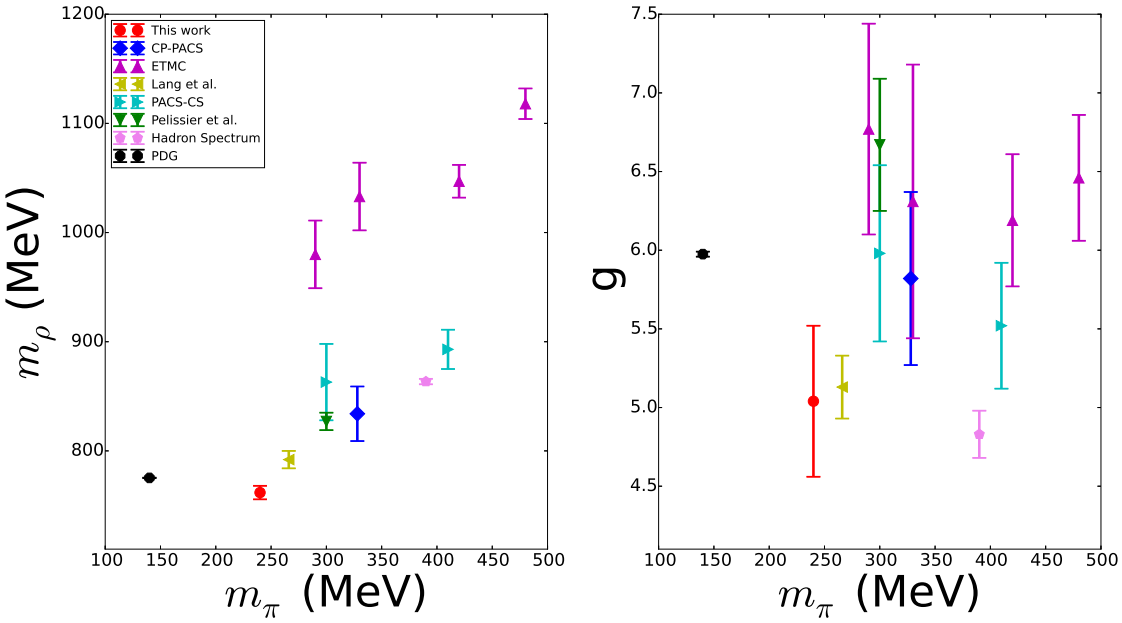

Figure 7.17: Values of the energy of the ρ resonance and the coupling, g, between ρ and $\pi\pi$ in various lattice studies. The horizontal axis shows the pion mass used in the lattice study as the energy of the resonance should be dependent on the light quark mass but the coupling is expected to be independent of the light quark mass. The black points shows the experimental results from the PDG [46] plotted at the physical pion mass. The red points show the values from this work shown in the previous section. The remain colors come from results from other collaborations or authors. Details of each of the other studies is explained in the text.

separate points in Figure 7.17 for the four different pion masses used. Their values for the energy of the resonance appears to be inconstantly large compared to other results though this may be a due to their method of setting the scale [53]. The calculation which previously had the lowest pion mass was from Lang et al. [50] however their lattice is small relative to their pion mass resulting in $m_\pi L < 4$ indicating that finite volume effects could be significant. The results from the Hadron Spectrum Collaboration [49] uses energies computed from 3 different anisotropic lattices with approximately the same pion mass to perform a single fit to the scattering phase shift. This may introduce systematic error as the pion mass or anisotropy may be different on each different volume. However all the listed results have values of the $\rho \to \pi\pi$ coupling which are consistent within 2-3 standard deviation. Future results may be able to compute the phase shift on larger lattices and pion masses approaching the

	m_π	# of lattice points	# of energies used	$m_\pi L$
This work	240	$32^3 \times 256$	30	4.7
CP-PACS	320	$12^3 \times 24$	2	4.2
ETMC	290-480	$24^4, 32^4$	5-6	≥ 3.7
Lang et al.	270	$16^3 \times 32$	5	2.7
PACS-CS	300, 410	$32^3 \times 64$	6	≥ 4.4
Pelissier et al.	300	$24^2 \times (24, 30, 48) \times 48$	6	≥ 4.6
Hadron Spectrum	390	$(16^3, 20^3, 24^3) \times 128$	29^*	≥ 3.8

Table 7.11: Lattice parameters used by other collaborations for the $I = 1$ $\pi\pi$ scattering phase shift. If multiple lattices are used then all are listed and in such cases the $m_\pi L$ listed corresponds to the lattice with the smallest value for $m_\pi L$. The fourth column shows the number of stationary state energies used to compute the phase shift with the exception of the last row where the 29 energy levels were used from all three lattices for a single fit for the phase shift.

physical pion mass as computing power and computational methods improve.

Chapter 8

Conclusions

The ability to efficiently compute temporal correlators for multi-meson operators in lattice QCD using the stochastic LapH method has opened up studies of excited states and scattering phase shifts. Figs. 7.9 and 7.16 summarize the main results of this work. The calculations presented here used 412 gauge-field configurations generated by a Monte Carlo method utilizing clover-improved Wilson fermions on an anisotropic $32^3 \times 256$ lattice with a pion mass near 240 MeV.

First, the low-energy spectrum of stationary states in the $I = 1$, $S = 0$, T_{1u}^+ channel was determined. A matrix of correlators built from 10 single meson operators and 53 two-meson operators was analyzed to extract the spectrum in this channel. The overlaps of the operators were inspected to identify the dominant particle content of each energy level in the finite volume. Levels with significant overlaps with the single-hadron operators were tentatively identified as "precursor" resonance states. In other words, we expect these levels should evolve into the actual resonance states as the volume becomes large. The masses of these states were compared with experiment.

We outlined how finite-volume two-particle energies can be related to infinite-volume scattering phase shifts. The energies were obtained for 30 $\pi\pi$ states of total isospin $I = 1$ with total zero and nonzero momenta in a variety of channels. These used to compute the $\pi\pi$ P-wave scattering phase shift in the vicinity of the ρ resonance. We were then able to estimate the mass and width of the ρ resonance by performing a Breit-Wigner fit to the energy dependence of the phase-shift.

In the future, we will compute the spectrum of meson and baryon resonances in other channels, as well as scattering phase shifts for a variety of other particles. The two-particle operators used here are not limited to $\pi\pi$ states, so the phase shift of $K\pi$

or $\eta\pi$ systems can be looked at with simple modifications. The methods used here can apply to all meson channels, including isoscalar mesons, as the stochastic LapH method can reliably and efficiently estimate quark propagation from all spatial sites on one time slice to all spatial sites on any other or the same time slice.

Increased computing power and new Monte Carlo algorithms are steadily improving our ability to study the interactions of quarks and gluons inside hadrons using lattice QCD. The stochastic LapH method, combined with availability of petascale heterogeneous computing resources, such as those provided by NSF XSEDE, which allows studies of large numbers of heavier excited hadrons that could not be investigated before. As more and more lattice QCD groups adapt the stochastic LapH method, our understanding of the excited hadron resonances, and hence, the inner workings of the atomic nucleus, will grow.

Bibliography

[1] K. G. Wilson, "Confinement of Quarks", Phys. Rev. **D10**, 2445–2459 (1974).

[2] H. B. Nielsen and M. Ninomiya, "No Go Theorem for Regularizing Chiral Fermions", Phys. Lett. **B105**, 219 (1981).

[3] B. Sheikholeslami and R. Wohlert, "Improved Continuum Limit Lattice Action for QCD with Wilson Fermions", Nucl. Phys. **B259**, 572 (1985).

[4] R. G. Edwards, B. Joo, and H.-W. Lin, "Tuning for Three-flavors of Anisotropic Clover Fermions with Stout-link Smearing", Phys. Rev. **D78**, 054501 (2008).

[5] T. DeGrand, A. Hasenfratz, and T. G. Kovács, "Improving the chiral properties of lattice fermions", Phys. Rev. D **67**, 054501 (2003).

[6] G. P. Lepage and P. B. Mackenzie, "On the viability of lattice perturbation theory", Phys. Rev. **D48**, 2250–2264 (1993).

[7] K. Symanzik, "Continuum Limit and Improved Action in Lattice Theories: 1. Principles and ϕ^4 Theory", Nucl. Phys. **B226**, 187 (1983).

[8] G. Curci, P. Menotti, and G. Paffuti, "Symanzik's Improved Lagrangian for Lattice Gauge Theory", Phys. Lett. **B130**, 205 (1983).

[9] M. Luscher and P. Weisz, "On-Shell Improved Lattice Gauge Theories", Commun. Math. Phys. **97**, 59 (1985).

[10] P. Matthews and A. Salam, "The Green's functions of quantized fields", Nuovo Cim. **12**, 563–565 (1954).

[11] P. Matthews and A. Salam, "Propagators of quantized field", Nuovo Cim. **2**, 120–134 (1955).

[12] S. Duane, A. Kennedy, B. Pendleton, and D. Roweth, "Hybrid Monte Carlo", Phys. Lett. **B195**, 216–222 (1987).

[13] M. Clark, "The Rational Hybrid Monte Carlo Algorithm", PoS **LAT2006**, 004 (2006).

[14] H.-W. Lin et al., "First results from 2+1 dynamical quark flavors on an anisotropic lattice: Light-hadron spectroscopy and setting the strange-quark mass", Phys. Rev. **D79**, 034502 (2009).

[15] C. Morningstar, J. Bulava, J. Foley, K. J. Juge, D. Lenkner, et al., "Improved stochastic estimation of quark propagation with Laplacian Heaviside smearing in lattice QCD", Phys. Rev. **D83**, 114505 (2011).

[16] M. Peardon et al., "A Novel quark-field creation operator construction for hadronic physics in lattice QCD", Phys. Rev. **D80**, 054506 (2009).

[17] K. Wu and H. Simon, "Thick-Restart Lanczos Method for Large Symmetric Eigenvalue Problems", SIAM Journal on Matrix Analysis and Applications **22**, 602–616 (2000).

[18] C. Morningstar, J. Bulava, B. Fahy, J. Foley, Y. Jhang, et al., "Extended hadron and two-hadron operators of definite momentum for spectrum calculations in lattice QCD", Phys. Rev. **D88**, 014511 (2013).

[19] C. J. Morningstar and M. Peardon, "Glueball spectrum from an anisotropic lattice study", Phys. Rev. D **60**, 034509 (1999).

[20] S. Basak, R. Edwards, G. Fleming, U. Heller, C. Morningstar, et al., "Group-theoretical construction of extended baryon operators in lattice QCD", Phys. Rev. **D72**, 094506 (2005).

[21] R. Penrose, "A Generalized inverse for matrices", Proc. Cambridge Phil. Soc. **51**, 406–413 (1955).

[22] J. Foley, K. Jimmy Juge, A. O'Cais, M. Peardon, S. M. Ryan, et al., "Practical all-to-all propagators for lattice QCD", Comput. Phys. Commun. **172**, 145–162 (2005).

[23] J. Foley, C. H. Wong, J. Bulava, K. J. Juge, D. Lenkner, et al., "A novel method for evaluating correlation functions in lattice hadron spectroscopy", (2010).

[24] M. Matsumoto and T. Nishimura, "Mersenne twister: a 623-dimensionally equidistributed uniform pseudo-random number generator", ACM Trans. Model. Comput. Simul. **8**, 3–30 (1998).

[25] A. Reifman, B. S. DeWitt, and R. G. Newton, "Relations between bound-state problems and scattering theory", Phys. Rev. **101**, 877–879 (1956).

[26] B. S. DeWitt, "Transition from discrete to continuous spectra", Phys. Rev. **103**, 1565–1571 (1956).

[27] M. Luscher, "ON A RELATION BETWEEN FINITE SIZE EFFECTS AND ELASTIC SCATTERING PROCESSES", (1983).

[28] M. Luscher, "Volume Dependence of the Energy Spectrum in Massive Quantum Field Theories. 1. Stable Particle States", Commun. Math. Phys. **104**, 177 (1986).

[29] M. Luscher, "Volume Dependence of the Energy Spectrum in Massive Quantum Field Theories. 2. Scattering States", Commun. Math. Phys. **105**, 153–188 (1986).

[30] M. Luscher, "Two particle states on a torus and their relation to the scattering matrix", Nucl. Phys. **B354**, 531–578 (1991).

[31] K. Rummukainen and S. Gottlieb, "Resonance scattering phase shifts on a non-rest-frame lattice", Nuclear Physics B **450**, 397–436 (1995).

[32] C. Kim, C. Sachrajda, and S. R. Sharpe, "Finite-volume effects for two-hadron states in moving frames", Nuclear Physics B **727**, 218–243 (2005).

[33] Z. Davoudi and M. J. Savage, "Improving the volume dependence of two-body binding energies calculated with lattice qcd", Phys. Rev. D **84**, 114502 (2011).

[34] Z. Fu, "Rummukainen-gottlieb formula on a two-particle system with different masses", Phys. Rev. D **85**, 014506 (2012).

[35] L. Leskovec and S. Prelovsek, "Scattering phase shifts for two particles of different mass and nonzero total momentum in lattice qcd", Phys. Rev. D **85**, 114507 (2012).

[36] M. T. Hansen and S. R. Sharpe, "Multiple-channel generalization of lellouch-lüscher formula", Phys. Rev. D **86**, 016007 (2012).

[37] R. A. Briceño, "Two-particle multichannel systems in a finite volume with arbitrary spin", Phys. Rev. D **89**, 074507 (2014).

[38] M. Jacob and G. Wick, "On the general theory of collisions for particles with spin", Annals Phys. **7**, 404–428 (1959).

[39] A. J. Macfarlane, "Kinematics of the Relativistic Two-Particle System", J. Math. Phys. **4**, 490 (1963).

[40] A. Martin and T. Spearman, *Elementary particle theory* (North-Holland Pub. Co., 1970).

[41] M. Göckeler, R. Horsley, M. Lage, U.-G. Meißner, P. E. L. Rakow, A. Rusetsky, G. Schierholz, and J. M. Zanotti, "Scattering phases for meson and baryon resonances on general moving-frame lattices", Phys. Rev. D **86**, 094513 (2012).

[42] W. H. Press, S. Teukolsky, W. Vetterling, and B. Flannery, *Numerical recipes in c: the art of scientific computing, second edition* (Cambridge Univ. Press, New York, 1992).

[43] F. James and M. Roos, "Minuit - a system for function minimization and analysis of the parameter errors and correlations", Computer Physics Communications **10**, 343–367 (1975).

[44] D. W. Lenkner, "The Spectrum of Meson States in the Isovector Non-strange T_{1u}^{+} Channel by the Stochastic LapH Method in Lattice QCD", PhD thesis (Carnegie Mellon University, 2013).

[45] R. G. Edwards and B. Joo, "The Chroma software system for lattice QCD", Nucl. Phys. Proc. Suppl. **140**, 832 (2005).

[46] J. B. et al., "Review of Particle Physics", Phys. Rev. **D86**, 010001 (2012).

[47] S. Aoki, M. Fukugita, K.-I. Ishikawa, N. Ishizuka, K. Kanaya, Y. Kuramashi, Y. Namekawa, M. Okawa, K. Sasaki, A. Ukawa, and T. Yoshié, "Lattice qcd calculation of the ρ meson decay width", Phys. Rev. D **76**, 094506 (2007).

[48] X. Feng, K. Jansen, and D. B. Renner, "Resonance parameters of the ρ meson from lattice qcd", Phys. Rev. D **83**, 094505 (2011).

[49] J. J. Dudek, R. G. Edwards, and C. E. Thomas, "Energy dependence of the ρ resonance in $\pi\pi$ elastic scattering from lattice qcd", Phys. Rev. D **87**, 034505 (2013).

[50] C. B. Lang, D. Mohler, S. Prelovsek, and M. Vidmar, "Coupled channel analysis of the ρ meson decay in lattice qcd", Phys. Rev. D **84**, 054503 (2011).

[51] S. Aoki, K.-I. Ishikawa, N. Ishizuka, K. Kanaya, Y. Kuramashi, Y. Namekawa, M. Okawa, Y. Taniguchi, A. Ukawa, N. Ukita, T. Yamazaki, and T. Yoshié, "ρ meson decay in 2+1 flavor lattice qcd", Phys. Rev. D **84**, 094505 (2011).

[52] C. Pelissier and A. Alexandru, "Resonance parameters of the rho-meson from asymmetrical lattices", Phys. Rev. D **87**, 014503 (2013).

[53] T. YAMAZAKI, "Hadronic interactions", The 32nd International Symposium on Lattice Field Theory, 2014.